SANDIA REPORT
SAND2010-3400
Unlimited Release
Printed May 2010

Characterization and Modeling of Thermal Diffusion and Aggregation in Nanofluids

Patricia E. Gharagozloo and Kenneth E. Goodson

Prepared by
Sandia National Laboratories
Albuquerque, New Mexico 87185 and Livermore, California 94550

Sandia National Laboratories is a multi-program laboratory operated by Sandia Corporation, a wholly owned subsidiary of Lockheed Martin Corporation, for the U.S. Department of Energy's National Nuclear Security Administration under contract DE-AC04-94AL85000.

Approved for public release; further dissemination unlimited.

Sandia National Laboratories

Issued by Sandia National Laboratories, operated for the United States Department of Energy by Sandia Corporation.

NOTICE: This report was prepared as an account of work sponsored by an agency of the United States Government. Neither the United States Government, nor any agency thereof, nor any of their employees, nor any of their contractors, subcontractors, or their employees, make any warranty, express or implied, or assume any legal liability or responsibility for the accuracy, completeness, or usefulness of any information, apparatus, product, or process disclosed, or represent that its use would not infringe privately owned rights. Reference herein to any specific commercial product, process, or service by trade name, trademark, manufacturer, or otherwise, does not necessarily constitute or imply its endorsement, recommendation, or favoring by the United States Government, any agency thereof, or any of their contractors or subcontractors. The views and opinions expressed herein do not necessarily state or reflect those of the United States Government, any agency thereof, or any of their contractors.

Printed in the United States of America. This report has been reproduced directly from the best available copy.

Available to DOE and DOE contractors from
U.S. Department of Energy
Office of Scientific and Technical Information
P.O. Box 62
Oak Ridge, TN 37831

Telephone: (865) 576-8401
Facsimile: (865) 576-5728
E-Mail: reports@adonis.osti.gov
Online ordering: http://www.osti.gov/bridge

Available to the public from
U.S. Department of Commerce
National Technical Information Service
5285 Port Royal Rd.
Springfield, VA 22161

Telephone: (800) 553-6847
Facsimile: (703) 605-6900
E-Mail: orders@ntis.fedworld.gov
Online order: http://www.ntis.gov/help/ordermethods.asp?loc=7-4-0#online

SAND2010-3400
Unlimited Release
Printed May 2010

Characterization and Modeling of Thermal Diffusion and Aggregation in Nanofluids

Patricia E. Gharagozloo and Kenneth E. Goodson
Department of Mechanical Engineering
Stanford University
440 Escondido Way, Bldg 530
Stanford, CA 94305
peghara@sandia.gov
goodson@stanford.edu

Abstract

Fluids with higher thermal conductivities are sought for fluidic cooling systems in applications including microprocessors and high-power lasers. By adding high thermal conductivity nanoscale metal and metal oxide particles to a fluid the thermal conductivity of the fluid is enhanced. While particle aggregates play a central role in recent models for the thermal conductivity of nanofluids, the effect of particle diffusion in a temperature field on the aggregation and transport has yet to be studied in depth.

The present work separates the effects of particle aggregation and diffusion using parallel plate experiments, infrared microscopy, light scattering, Monte Carlo simulations, and rate equations for particle and heat transport in a well dispersed nanofluid. Experimental data show non-uniform temporal increases in thermal conductivity above effective medium theory and can be well described through

simulation of the combination of particle aggregation and diffusion. The simulation shows large concentration distributions due to thermal diffusion causing variations in aggregation, thermal conductivity and viscosity.

Static light scattering shows aggregates form more quickly at higher concentrations and temperatures, which explains the increased enhancement with temperature reported by other research groups. The permanent aggregates in the nanofluid are found to have a fractal dimension of 2.4 and the aggregate formations that grow over time are found to have a fractal dimension of 1.8, which is consistent with diffusion limited aggregation. Calculations show as aggregates grow the viscosity increases at a faster rate than thermal conductivity making the highly aggregated nanofluids unfavorable, especially at the low fractal dimension of 1.8. An optimum nanoparticle diameter for these particular fluid properties is calculated to be 130 nm to optimize the fluid stability by reducing settling, thermal diffusion and aggregation.

ACKNOWLEDGEMENTS

First of all, I would like to thank my research advisor Professor Ken Goodson for supporting and encouraging me to stay and pursue my PhD. He gave me the freedom to choose a topic and mold my project together and provided invaluable insight and encouragement particularly during the frustrating times. I am particularly grateful to Professor John Eaton, who gave unique perspectives on my research and consistent feedback and insight. I also appreciate the technical guidance from Professor Juan Santiago. I would also like to thank Dr. Jonathan Zimmerman for obtaining LDRD funding from Sandia National Labs to assist my research, giving me encouragement and guidance, serving on my defense committee, and giving feedback on my thesis. For serving as my defense committee chair, I would like to thank Professor Andrew Spakowitz.

I am fortunate to have the support and added guidance from a talented research group. I would like to thank the entire research group for the constant moral and technical support. I am especially grateful to Xuejiao Hu for mentoring me in the first year and teaching me how to use the infrared microscope. I would like to thank the researchers I worked closely with in nanofluids, Joo Hyun Lee and Babajide Kolade. For always being available to assist me when the camera software stopped working, I would like to thank Dr. Roger Flynn and Julie Steinbrenner. For teaching me how to use the Dynamic Light Scattering equipment, I thank Namjun Cho. I appreciate the help from Matt Panzer, John Reifenberg, and Jeremy Rowlette for always being

willing to talk through calculations, discuss possible measurement techniques, and explain phonon density of states. I would like to thank Cecilia Gichane-Bell, for always smiling and being willing to help with any purchases, reimbursements, and the many other administrative requests.

I am so very grateful for the constant support of my family and friends: to my loving husband, Ali, for being understanding and helpful during the most stressful of times, to my parents, Carmen and Linda, for listening to me talk about my research even when it passed their understanding, to my brother and sisters, Homer, Stephanie and Kathy, for the great distractions.

Financial support for this research was provided by a grant from the Office of Naval Research (overseen by Dr. Mark S. Spector) under the Grant No N00014-05-1-0374-P0001 and also by graduate fellowships from both the National Science Foundation and Sandia National Labs (overseen by Dr. Jonathan Zimmerman). Sandia National Laboratories is a multi program laboratory operated by Sandia Corporation, a wholly owned subsidiary of Lockheed Martin Corporation, for the U.S. Department of Energy's National Nuclear Security Administration under contract DE-AC04-94AL85000.

CONTENTS

1 Introduction 19

1.1 Electronics Cooling 20

1.2 Nanofluids History and Applications 23

1.3 Theoretical Models for Composite Materials 26

1.4 Nanofluid Favorability 28

1.5 Experimental Results 29

1.5.1 Temperature Dependence 30

1.5.2 Time Evolution 33

1.5.3 Aggregation 34

1.5.4 Viscosity 34

1.6 Theoretical Work 35

1.6.1 Brownian Motion and Micro-convection 35

1.6.2 Liquid Layering. 36

1.6.3 Near Field Radiation and Ballistic Transport 36

1.6.4 Aggregation 37

1.6.4.1 Fractal and Percolation Theory 37

1.6.4.2 Application to Nanofluids 38

1.6.5 Particle Diffusion 41

1.7 Objectives and Scope of this Study 43

2 Measurement Procedure for the Thermal Conductivity of Nanofluids 45
2.1 Introduction. 45
2.2 Experimental Setup 46
2.3 Measurement Results 48
2.4 Conclusions 53

3 Aggregate Characterization 37
3.1 Introduction 55
3.2 Nanofluid Preparation 56
3.3 Dynamic Light Scattering 57
3.3.1 Theory 57
3.3.2 Methodology 59
3.3.3 Results 60
3.4 Scanning Electron Microscopy 61
3.4.1 Theory 61
3.4.2 Methodology. 62
3.4.3 Results 62
3.5 Static Light Scattering 65
3.5.1 Measurement Theory 65
3.5.2 Measurement Setup 66
3.5.3 Results 69
3.6 Conclusions 79

4 Simulation of Aggregation and Thermal Diffusion 81
4.1 Introduction 81
4.2 Onsager Solution for Thermal Diffusion 82
4.2.1 Methodology 82
4.2.2 Results 84

4.3 Monte Carlo Simulation 87
4.3.1 Methodology 87
4.3.1.1 Particle Initialization and Aggregation 88
4.3.1.2 Effective Properties 90
4.3.2 Non-interacting Particles 95
4.3.3 Isothermal Aggregation 96
4.3.3.1 Effect on Fluid Properties 97
4.3.3.2 Comparison with Measurements 100
4.3.3.3 Particle Size Effect 102
4.3.4 Thermal Diffusion and Aggregation 103
4.3.4.1 Concentration Effects 103
4.3.4.2 Comparison with Thermal Measurement . 110
4.3.4.3 Effective Viscosity 113
4.3.4.4 Particle Size Effects 116
4.4 Particle Size Optimization 119
4.5 Conclusions 122

5 Conclusions 125
5.1 Summary 125
5.2 Discussion 126
5.3 Recommendations for Future Work 128

References 130

LIST OF TABLES

Number *Description* *Page*

Table 3.1: Measured pH values for various fluids 57

LIST OF FIGURES

Number *Description* *Page*

Figure 1.1: The 2007 ITRS predicted performance over time for single chip microprocessors 21

Figure 1.2: The 2007 ITRS power density predictions over time for cost performance (squares) and high performance (circles) single chip microprocessors 21

Figure 1.3: Typical fin-array heat sink cooling schematic 22

Figure 1.4: Schematic of microchannel heat sink 23

Figure 1.5: Computer simulated 3D aggregates with different fractal dimensions projected onto 2D plane 38

Figure 1.6: Schematic of a single aggregate with effective thermal conductivity k_a consisting of the backbone particles shown in black and dead-end particles shown in gray. The aggregate is decomposed into dead ends with the fluid and the backbone. Thermal conductivity of the aggregate only with particles belonging to the dead ends, k_{nc} is calculated using the Bruggeman model. Linear chains are embedded inside a medium with effective conductivity of k_{nc} 40

Figure 2.1: Schematic of infrared microscope experimental setup showing nanofluid held between copper plates and glass spacers. A heat flux is applied across the nanofluid with a thin Kapton heater, measured on the opposite side with a heat flux sensor, and dissipated into a thermoelectric cooler and heat sink. The temperature is monitored with thermocouples on the copper plates ... 47

Figure 2.2: Typical image of measured cross-sectional temperature distribution of a nanofluid of alumina suspended dispersed in deionized water (Alfa Aesar / 12733) subjected to a $4W/cm^2$ heat flux: (a) temperature distribution at white line, (b) temperature distribution image, and (c) temperature color scale..... 49

Figure 2.3: Plot of the time dependence of average thermal conductivity for varying concentration in nanofluid consisting of alumina particles dispersed in deionized water (Alfa Aesar / 12733) ……. 50

Figure 2.4: Measured time dependence of the full field thermal conductivity increase of a nanofluid consisting of alumina particles dispersed in deionized water (Alfa Aesar / 12733) in a temperature gradient for volumetric concentrations of (a) 5%, (b) 3%, and (c) 1% 52

Figure 3.1: Image of nanofluid of alumina particles suspended dispersed in deionized water (Alfa Aesar / 12733) diluted to the desired volumetric concentrations of 1%, 3% and 5% qualitatively showing level of transparency (vials illuminated from behind with a halogen lamp)..... 57

Figure 3.2: Measured multimodal particle size distributions from dynamic light scattering for nanofluid of alumina dispersed in deionized water (Alfa Aesar / 12733) diluted to $0.05\%_{vol}$ concentration presented in both number and intensity based distributions to show presence of permanent aggregates 60

Figure 3.3: SEM image of suspended alumina nanoparticles from the gelified water based nanofluid showing the presence of singlet particles and permanent aggregates of particles sintered together 63

Figure 3.4: Binary version of aggregate from SEM image. The particle volume fraction in the aggregate is estimated from this image to be 0.51 64

Figure 3.5: Schematic of static light scattering experimental setup showing nanofluid held in bottle at the specified temperature and at the measurement time is pulled into a stationary cuvee with a syringe pump. A laser is shone through the sample causing light to scatter. The scattered light intensity is measured versus angle using a photo detector attached to a rotary stage 67

Figure 3.6: Image of static light scattering setup including: (a) laser, (b) flow-through cell, (c) photodetector, and (d) motorized rotational stage..... 68

Figure 3.7: Log-log plot of the measured normalized intensity versus scattering vector for the NIST traceable size standards showing the -4 power law for $1/q < r_p$ (red line). Amorphous silica particles, 0.5 μm in diameter dispersed in deionized water (Alfa Aesar / 12733) are measured with the 785 nm laser (blue x's). Polystyrene particles, 150 nm in diameter dispersed in water are measured with the 633 nm laser (green dots) 68

Figure 3.8: Log-log plot of the measured normalized measured intensity versus scattering vector for the $1\%_{vol}$ concentration of alumina dispersed in deionized water (Alfa Aesar / 12733) at 20 ^{o}C with the 785 nm (blue x's) and 633 nm (green dots) lasers after an hour with a fit for the power law with a fractal dimension of 2.4 (red line) 69

Figure 3.9: Log-log plot of the measured normalized measured intensity versus scattering vector for the $1\%_{vol}$ concentration of alumina dispersed in deionized water (Alfa Aesar / 12733) at 60 ^{o}C with the 785 nm (blue x's) and 633 nm (green dots) lasers after an hour with a fit for the power law with a fractal dimension of 2.4 (red line)..... 70

Figure 3.10: Log-log plot of the measured normalized measured intensity versus scattering vector for the $3\%_{vol}$ concentration of alumina dispersed in deionized water (Alfa Aesar / 12733) at 20 ^{o}C with the 785 nm (blue x's) and 633 nm (green dots) lasers after an hour with a fit for the power law with a fractal dimension of 2.4 (red line) 71

Figure 3.11: Log-log plot of the measured normalized measured intensity versus scattering vector for the $3\%_{vol}$ concentration of alumina dispersed in deionized water (Alfa Aesar / 12733) at 40 ^{o}C with the 785 nm (blue x's) and 633 nm (green dots) lasers right after sonication with a fit for the power law with a fractal dimension of 2.0 (red line) and 2.4 (dotted red line) 71

Figure 3.12: Log-log plot of the measured normalized measured intensity versus scattering vector for the $3\%_{vol}$ concentration of alumina dispersed in deionized water (Alfa Aesar / 12733) at 40 ^{o}C with the 785 nm (blue x's) and 633 nm (green dots) lasers after an hour with a fit for the power law with a fractal dimension of 1.9 (red line) and 2.4 (dotted red line) 72

Figure 3.13: Log-log plot of the measured normalized measured intensity versus scattering vector for the $3\%_{vol}$ concentration of alumina dispersed in deionized water (Alfa Aesar / 12733) at 60 ^{o}C with the 785 nm (blue x's) and 633 nm (green dots) lasers right after sonication with a fit for the power law with a fractal dimension of 2.1 (red line) and 2.4 (dotted red line) 73

Figure 3.14: Log-log plot of the measured normalized measured intensity versus scattering vector for the $3\%_{vol}$ concentration of alumina dispersed in deionized water (Alfa Aesar / 12733) at 60 ^{o}C with the 785 nm (blue x's) and 633 nm (green dots) lasers after an hour with a fit for the power law with a fractal dimension of 1.8 (red line) and 2.3 (dotted red line) 73

Figure 3.15: Log-log plot of the measured normalized measured intensity versus scattering vector for the $5\%_{vol}$ concentration of alumina dispersed in deionized water (Alfa Aesar / 12733) at 20 ^{o}C with the 785 nm (blue x's) and 633 nm (green dots) lasers after an hour with a fit for the power law with a fractal dimension of 2.4 (red line) 74

Figure 3.16: Log-log plot of the measured normalized measured intensity versus scattering vector for the $5\%_{vol}$ concentration of alumina dispersed in deionized water (Alfa Aesar / 12733) at 40 ^{o}C with the 785 nm (blue x's) and 633 nm (green dots) lasers right after sonication with a fit for the power law with a fractal dimension of 1.8 (red line) and 2.4 (dotted red line) 75

Figure 3.17: Log-log plot of the measured normalized measured intensity versus scattering vector for the $5\%_{vol}$ concentration of alumina dispersed in deionized water (Alfa Aesar / 12733) at 40 ^{o}C with the 785 nm (blue x's) and 633 nm (green dots) lasers after an hour with a fit for the power law with a fractal dimension of 1.8 (red line) and 2.3 (dotted red line) 75

Figure 3.18: Log-log plot of the measured normalized measured intensity versus scattering vector for the $5\%_{vol}$ concentration of alumina dispersed in deionized water (Alfa Aesar / 12733) at 60 ^{o}C with the 785 nm (blue x's) and 633 nm (green dots) lasers right after sonication with a fit for the power law with a fractal dimension of 1.8 (red line) and 2.2 (dotted red line) 76

Figure 3.19: Log-log plot of the measured normalized measured intensity versus scattering vector for the $5\%_{vol}$ concentration of alumina dispersed in deionized water (Alfa Aesar / 12733) at 60 ^{o}C with the 785 nm (blue x's) and 633 nm (green dots) lasers after an hour with a fit for the power law with a fractal dimension of 1.8 (red line) and 2 (dotted red line) 76

Figure 3.20: Plot of the measured fractal dimension versus time for the $1\%_{vol}$ concentration of 40 nm alumina nanoparticles dispersed in deionized water (Alfa Aesar / 12733) at 20 and 60 ^{o}C..... 77

Figure 3.21: Plot of the measured fractal dimension versus time for the $3\%_{vol}$ concentration of 40 nm alumina nanoparticles dispersed in deionized water (Alfa Aesar / 12733) at 20, 40, and 60 ^{o}C 78

Figure 3.22: Plot of the measured fractal dimension versus time for the $5\%_{vol}$ concentration of 40 nm alumina nanoparticles dispersed in deionized water (Alfa Aesar / 12733) at 20, 40, and 60 ^{o}C 78

Figure 4.1: Calculated normalized particle concentration distribution, calculated from the numerical solution to the Soret effect in the Onsager relations, at steady state for various S_T values for 40 nm alumina nanoparticles in water subjected to a heat flux of 4 W/cm^2 86

Figure 4.2: Calculated normalized particle concentration distribution, calculated from the numerical solution to the Soret effect in the Onsager relations with S_T of 0.025 K^{-1}, at steady state for various particle diameters for alumina nanoparticles in water subjected to a heat flux of 4 W/cm^2 ……..... 87

Figure 4.3: Calculated normalized thermal conductivity enhancement versus aggregate radius of gyration for 40 nm alumina nanoparticles in water for various fractal dimensions 93

Figure 4.4: Calculated normalized viscosity enhancement versus aggregate radius of gyration for 40 nm alumina nanoparticles in water for various fractal dimensions 94

Figure 4.5: Calculated ratio of viscosity to thermal conductivity enhancement versus aggregate radius of gyration for 40 nm alumina nanoparticles in water for various fractal dimensions 94

Figure 4.6: Calculated normalized particle distribution for Monte Carlo simulation without aggregation or particle interaction (dashed) and numerical model (solid) for a S_T of 0.025 K^{-1} and d of 40 nm at times of 10, 40 and 180 minutes for alumina nanoparticles in water subjected to a heat flux of 4 W/cm^2 96

Figure 4.7: Simulated average radius of gyration of the aggregates over time for 1%, 3%, and $5\%_{vol}$ concentrations at 20, 40, and 60 ^oC 97

Figure 4.8: Predicted thermal conductivity plotted over time for the three concentrations each at the three temperatures calculated from the volume average of the simulated aggregate radius of gyration for a fractal dimension of 1.8 in a nanofluid with 40 nm alumina nanoparticles dispersed in water 98

Figure 4.9: Calculated viscosity plotted over time for the three concentrations each at the three temperatures calculated from the volume average of the simulated aggregate radius of gyration for a fractal dimension of 1.8 in a nanofluid with 40 nm alumina nanoparticles dispersed in water 99

Figure 4.10: Calculated ratio of the viscosity to thermal conductivity enhancements plotted over time for the three concentrations each at the three temperatures calculated from the volume average of the simulated aggregate radius of gyration for a fractal dimension of 1.8 in a nanofluid with 40 nm alumina nanoparticles dispersed in water..... 100

Figure 4.11: Plot of the simulated change in size after an hour versus initial particle diameter for three temperatures in a water based nanofluid at a $5\%_{vol}$ concentration 102

Figure 4.12: Predicted average aggregate radius of gyration distribution across the nanofluid at various times from the Monte Carlo simulation for 1%, 3%, and $5\%_{vol}$ concentrations of nominal diameter alumina nanoparticles in water subjected to a heat flux 104

Figure 4.13: The simulated average radius of gyration of the aggregates in the nanofluids over time for the three concentrations of the nanofluid of 40 nm alumina nanoparticles in water 105

Figure 4.14: Simulated volume concentration distribution across nanofluid at various times from the Monte Carlo simulation for 1%, 3%, and $5\%_{vol}$ concentrations of 40 nm nominal diameter alumina nanoparticles in water subjected to a heat flux 106

Figure 4.15: Simulated thermal conductivity distribution across the nanofluid at various times from the Monte Carlo simulation for 5%, 3% and $1\%_{vol}$ concentrations of 40 nm nominal diameter alumina nanoparticles in water subjected to a heat flux 108

Figure 4.16: Plot of the simulated average thermal conductivity over time from the Monte Carlo simulation with no boundary resistance (dashed) and with typical boundary resistance of 0.77 m^2K/W between alumina and water (dash - dot) 109

Figure 4.17: Plot of the simulated average thermal conductivities over time from the Monte Carlo simulation for the 1%, 3% and $5\%_{vol}$ concentrations for d_l = 1 (dot / x), 1.4 (dash) and 1.6 (dash-dot / .) .. 110

Figure 4.18: Plot of the average thermal conductivity of the nanofluid over time from the Monte Carlo simulation (dashed) and experimental data (dotted) for 1%, 3%, and $5\%_{vol}$ concentrations of 40 nm nominal diameter alumina nanoparticles in water 111

Figure 4.19: Plot of the average thermal conductivity of the nanofluid over time from the Monte Carlo simulation (dashed) and experimental data shifted by 10 minutes (dotted) for 1%, 3%, and $5\%_{vol}$ concentrations of 40 nm nominal diameter alumina nanoparticles in water 111

Figure 4.20: Plot of the simulated thermal conductivity of the $5\%_{vol}$ concentration of 40 nm alumina particles suspended in water subjected to a 40 ^oC isothermal condition for the first 10 minutes then to a 4 W/cm^2 heat flux 113

Figure 4.21: Calculated viscosity distribution of the base fluid and nanofluid across the cavity at various times from the Monte Carlo simulation for $3\%_{vol}$ concentrations of 40 nm nominal diameter alumina nanoparticles in water subjected to a heat flux 114

Figure 4.22: Plot of the calculated ratio of viscosity increase to thermal conductivity increase over time from the full Monte Carlo simulation for the three concentrations of 40 nm alumina nanoparticles suspended in water 115

Figure 4.23: Plot of calculated average radius of gyration of the aggregates over time from the Monte Carlo simulation for $5\%_{vol}$ concentration for particle diameters of 40 nm, 60 nm, 80 nm, and 130 nm 117

Figure 4.24: Plot of the calculated average effective thermal conductivity over time from the Monte Carlo simulation for $5\%_{vol}$ concentration for particle diameters of 40 nm, 60 nm, 80 nm, and 130 nm 118

Figure 4.25: Calculated ratio of the average viscosity and thermal conductivity enhancement factor over time from the Monte Carlo simulation for $5\%_{vol}$ concentration and 40 nm, 60 nm, 80 nm, and 130 nm nominal diameter 118

Figure 4.26: Time constant for aggregation (dot), settling (dash), and diffusion (dash-dot) plotted versus particle radius. For each line the arrow points in the direction of increased stability 122

Chapter 1

Introduction

Cooling has become one of the foremost challenges in current technology. In a wide variety of fields including electronics, lighting, transportation, space exploration and manufacturing, the performance and efficiencies are limited by the cooling abilities. Fluidic cooling through advanced microchannel heat exchangers has emerged as a promising cooling solution for electronic systems. Two-phase cooling has proven to be unstable in the microscale channels and unable to provide consistent cooling of hot spots on microprocessors without channel dry-out. Fluid design is an important aspect of this cooling solution, since the working fluid must offer low viscosity, high thermal conductivity, high heat capacity, as well as a relatively low freezing point.

Fluids with suspensions of higher thermal conductivity nanoscale metal and metal oxide particles, nanofluids, are being considered as an option for improved fluid design. By adding nanoscale high thermal conductivity particles, the thermal conductivity of the fluid can be enhanced while the viscosity is only moderately increased. Maxwell's effective medium theory for dilute suspensions of spherical particles predicts a 3% increase in thermal conductivity for each 1% $_{vol}$ concentration added to the fluid. Predictions of Einstein for well dispersed nanoparticle suspensions give a 2.5% increase in viscosity per 1%$_{vol}$ concentration. These predictions result in a larger increase in the thermal power removed by the system than pump power required to drive the nanofluid through the system.

1.1 Electronics Cooling

Electronic devices unavoidably produce heat, which must be minimized to prevent device failure.[1] The drive for reduced size and increased speed and performance has produced high density multi-chip packaging resulting in high heat densities. The power generated in the semiconductor during switching is linearly proportional to the performance frequency and is given by:[1]

$$P = \frac{CV^2}{2} f \tag{1.1}$$

where C is the input capacitance, V is the peak-to-peak voltage, and f is the switching frequency. Even with efforts to minimize the input capacitance and voltage over the past few decades, the heat generated is still rising due to the increasing performance.

The International Technology Roadmap for Semiconductor (ITRS), which identifies the critical challenges of the future to encourage innovative solutions, 2007 report [2] projects the performance to increase from 5.45 in 2009 to 14.34 GHz in 2022. Their projections for the performance are plotted in Figure 1.1. ITRS predicts the power density of the single chip cost performance microprocessor to increase from 0.90 in 2009 to 1.73 W/mm^2 in 2022. For the single chip high performance microprocessor the power density is expect to remain constant over the same period of time due to the allowed increase in chip size to 5 times the size of the cost performance. The cost performance microprocessors result in reduced chip-to-board performance. These trends are plotted in Figure 1.2. The lack of a sufficient cooling solution has caused the recent increase in chip size for high performance microprocessors and development of multi-processor chips, causing the predicted flattening of the respective power density curve. It is apparent from these predictions that more efficient cooling solutions are required to continue the progress of the past.

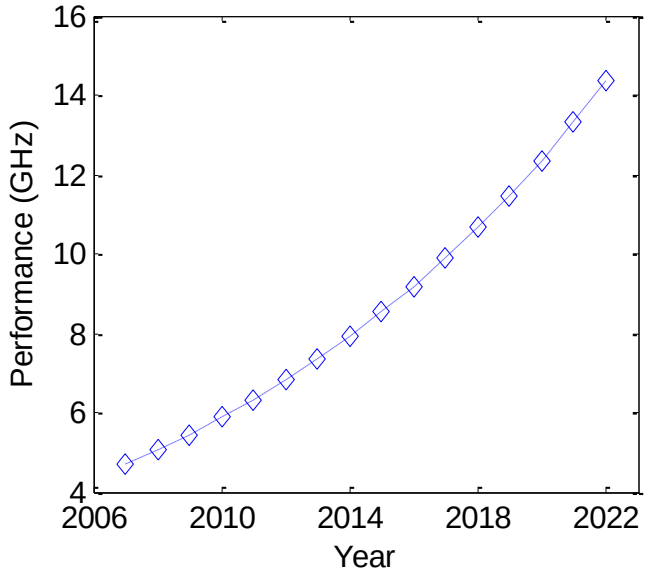

Figure 1.1: The 2007 ITRS predicted performance over time for single chip microprocessors.[2]

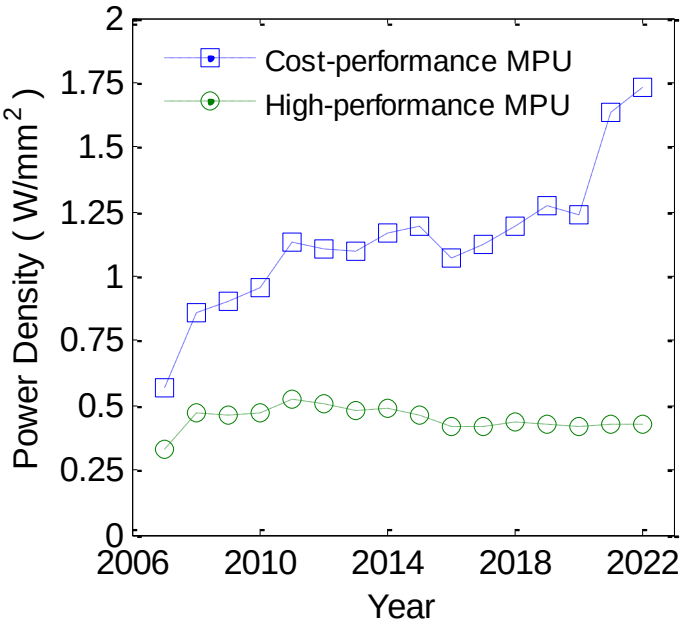

Figure 1.2: The 2007 ITRS power density predictions over time for cost performance (squares) and high performance (circles) single chip microprocessors.

The most widely used cooling method for electronics to date has been forced air convection, but this method is unable to keep up with the increasing level of heat flux due to the necessary increase in size of the metal fin-array heat sinks. A schematic of a typical fin-array heat sink is shown in Figure 1.3. Much research has been spent developing this design through fin redesigning and improvements in the thermal interface material properties.[3]

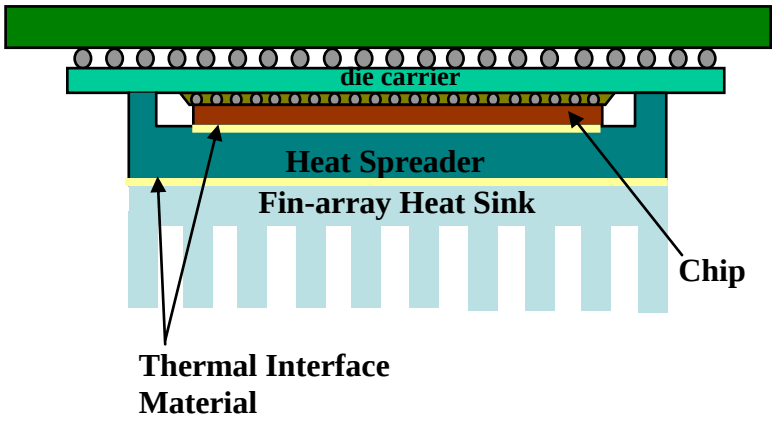

Figure 1.3: Typical fin-array heat sink cooling schematic.

Given the limitations of conventional forced air convection cooling, various solutions have been proposed including thermoelectric cooling [4-6], miniature heat pipes [7,8], microchannel heat sinks [9-11], and two-phase boiling [12-14]. Thermoelectric cooling tends to be inefficient since additional electric power must be supplied to the thermoelectric device. Two-phase boiling in microchannels and heat pipes creates flow and pressure instabilities, which can lead to channel dry-out. Single phase microchannel heat sinks offer better stability, but are limited by the thermal properties of the cooling fluid, which tend to be low. Figure 1.4 shows a schematic of a microchannel heat sink.

Nanofluids, which are metal or metal oxide nanoparticles suspended in fluid, offer a solution. By adding higher thermal conductivity nanoparticles to the fluid, the

effective thermal conductivity is increased without experiencing large increases in viscosity.

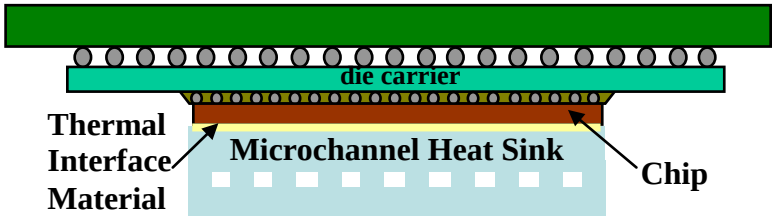

Figure 1.4: Schematic of microchannel heat sink.

1.2 Nanofluids History and Applications

Nanofluids have been studied for variety of other applications from tribology to cancer detection and treatment. In general, colloidal dispersions are dispersions of one phase within a second continuous phase. Both phases could be gas, liquid or solid. The size of the dispersed phase is typically on the order of a few microns to nanometers. Typical examples of colloids are foams like beer head, emulsions like mayonnaise, aerosols like mist, and solutions like ink or stained glass.[15] Nanocolloids are colloidal dispersions containing dispersed phases between 1 nm and 100 nm. Nanofluids are nanocolloids with dilute dispersions of nanoscale metal and metal oxide particles.

One of the earliest occurrences of nanocolloids occurred around the 5th century BC with the use of gold and silver colloids as red and blue colorant, respectively, for glass and ceramics. The most famous example is the Lycurgus cup from 4th century AD Rome that appears green, but when light is shone through the glass glows red due to the colloidal gold. In the 1600s colloidal gold became popular as a medicine for a variety of diseases. In the early 1900s it was used as a detection method for syphilis due to a reaction between the gold particles and the altered proteins in the spinal fluid.[16]

Nanofluids have been of great interest over the past couple decades for a variety of applications which are discussed briefly here. Some of the earliest investigations of electrical/mechanical applications of suspensions of metallic/semimetalic particles in fluids are electrorheological and magnetorheological fluids. Electrorheological fluids are fluids with dispersions of semiconducting particles with diameters on the order of 5 – 50 μm. When an electric field is applied to the fluid the particles polarize and align into chain like structures that can bridge the electrodes. These structures impede the flow of the fluid greatly increasing the effective viscosity. However, large field strengths are required for relatively low effective viscosity increases.[17]

Similarly, magnetorheological fluids, fluids containing magnetizable particles typically on the order of 0.1-10 μm are used as a viscosity control mechanism in a variety of applications. They result in much larger effective viscosity increases with lower voltage sources than electrorheological fluids. By applying a magnetic field to the fluid, the particles magnetize and align together to form linear aggregates in the direction of the field. As a result a much greater force is required to move the fluid and the apparent viscosity can increase as much as several orders of magnitude. Once the magnetic field is removed the process is reversed and the fluid returns to its original state. These fluids are currently being used in shock absorbers, artificial joints, and automotive clutches.[18]

Ferrofluids are fluids with suspensions of magnetic nanoparticles. The nanoparticles are typically functionalized to prevent aggregation. These fluids are used in a variety of applications. Ferrofluids are often used in loudspeakers to cool the voice coil and dampen the cone movement. The particles become less magnetic at higher temperatures causing fluid close to the hot, magnetic voice coil to move away and cooler fluid close to the heat sink to move towards the voice coil. This effect is called thermomagnetic convection. The ferrofluid allows for more efficient function, improved audio response and better power handling.[19] Ferrofluids are also used as rotary liquid seals. They are held in place by a magnet surrounding the rotating shaft

sealing the region. One of the main applications is the spinning drive shaft of a hard disk.

Nanofluids are being considered for medical detection and treatments. Magnetic nanoparticles have been shown to be functionalizable to bind to biomolecules. They can be sensed through observation of the magnetic behavior for diagnostic applications. Due to their magnetic nature, the nanoparticles can be controlled through an external magnetic field and forced to carry medication to a specific targeted region. In an alternating magnetic field, the magnetic nanoparticles could be used to generate heat to destroy tumors through magnetic hyperthermia and thermoablation.[20]

Similarly, gold nanoparticles have shown much promise due to their ability to conjugate easily altering their surface properties to target certain types of cells or antibodies. Once attached to the appropriate cells their optical properties allow for sensing of the nanoparticles or heating of the area immediately around the nanoparticles to destroy the surrounding cells.[21-24]

Due to the increased complexity, higher speeds and loads, and higher working temperatures in modern machinery, increased concern for the environment, and increased use of synthetic lubricants with little to no anti-wear ability, there is an increase in the demand for more novel lubrication fluids. The development of large scale metal nanoparticle synthesis techniques has allowed for the development of nanolubricants.[25] The use of nanoparticles in lubricants may prove to be a useful alternative to corrosive and polluting compounds, such as chlorine, currently in use to improve the anti-wear and extreme pressure abilities of the lubricants. The main issue is to create a stabilized suspension of the nanoparticles to prevent aggregation and precipitation. Multiple groups have recently shown that once properly stabilized the nanolubricants perform well.[26-29]

1.3 Theoretical Models for Composite Materials

During the past century, multiple theories of the effective thermal conductivities of composites have been developed. For this purpose, we are most interested in the theories governing particles in a fluid matrix and will focus on spherical and ellipsoidal particle suspensions. By using these theories it is assumed that the fluid matrix and suspended particles can be treated as a composite and convection is negligible.

Bruggeman considered a spherical inclusion embedded in a uniform medium with a uniform electric field, E_0, far from the inclusion leading to a dipole moment in the spherical volume producing a deviation from E_0. If the average deviation is taken as zero we get an equation for the effective conductivity, k_{eff}, of a multi-component system:[30]

$$\sum_i \varphi_i \frac{k_i - k_{eff}}{k_i + 2k_{eff}} = 0 \tag{1.2}$$

where φ_i is the volume fraction of component i and k_i is the conductivity of component i.

The most well known and widely used theory is that of Maxwell. For monodisperse spherical particles contained in a sphere of larger radius, Maxwell equated the potential for the particles in the surrounding medium to the potential of the larger sphere containing all the particles with an effective conductivity in the surrounding medium and backed out the effective thermal conductivity. This yields the effective medium theory (EMT) for random dispersed, non-interacting, spherical particles dispersed in another material given by the following equation:[31]

$$k_{eff} = k_f \frac{k_p + 2k_f - 2\varphi(k_f - k_p)}{k_p + 2k_f + \varphi(k_f - k_p)} \tag{1.3}$$

where φ is the particle volume fraction, k_p is the particle thermal conductivity and k_f is the matrix thermal conductivity. This model can be simplified for the case when $k_p >> k_f$ and $\varphi << 1$ to $k_{eff} = k_f(1+3\varphi)$.

The Maxwell formula was expanded by Fricke for homogeneous ellipsoidal particles given below in equation 1.4 and Hamilton and Crosser (H-C) for particles of varying sphericity given below in equation 1.5.[32]

$$k_{eff} = k_f \left[\frac{1 + \left(F \frac{k_p}{k_f} - 1 \right)}{1 + \varphi(F-1)} \right], \quad F = \frac{1}{3} \sum_{i=1}^{3} \left[1 + \left(\frac{k_p}{k_f} - 1 \right) f_i \right], \quad \sum_{i=1}^{3} f_i = 1 \tag{1.4}$$

$$k_{eff} = k_f \frac{k_p + (n-1)k_f - (n-1)\varphi(k_f - k_p)}{k_p + (n-1)k_f + \varphi(k_f - k_p)} \tag{1.5}$$

where f_i represents the axes of the ellipsoid and are equal for a spherical particle, $n=3/\psi$ is an empirical constant related to the sphericity of the particles, ψ, and was determined by Maxwell to be 3 for spherical particles and increases as the sphericity reduces.

More recently, Nan expanded these models to include a boundary resistance between the two mediums.[33] For an ellipsoid with an aspect ratio of $p = a_3 / a_1$, a dimensionless parameter α is defined as $a_k / a_{1,3}$, whichever is greater, where a_k is the Kapitza radius and is related to the boundary resistance and surrounding medium thermal conductivity by $a_k = R_B\ k_f$. The resulting equations for spherical and

randomly oriented ellipsoidal particles uniformly distributed in another medium are given below, respectively:

$$k_{eff} = k_f \frac{k_p(1+2\alpha) + 2k_f - 2\varphi(k_f - k_p(1-\alpha))}{k_p(1+2\alpha) + 2k_f + \varphi(k_f - k_p(1-\alpha))} \tag{1.6}$$

In 1911 Einstein [34] formulated a model for the increase in viscosity for well dispersed spherical nanoparticle suspensions. He found the viscosity increase follows $\mu_{eff} = \mu_f (1 + 2.5\varphi)$. This formula was found to predict experiments well for particle sizes of 2.5 to 80 μm and volume concentrations from 0.01 to 0.14.[35] Taking the effective viscosity model of Einstein and effective thermal conductivity model of Maxwell for $k_p >> k_f$, we would expect the thermal conductivity to increase by 3% and the viscosity to increase by 2.5% per 1% particle volume concentration.

1.4 Nanofluid Favorability

For the use of a nanofluid to be beneficial, the pumping power required to drive the fluid must decrease at a given level of thermal power removal. For a single circular channel, the work required to drive a fluid is given by:

$$W = Q\Delta P \tag{1.7}$$

$$\Delta P = \frac{128QL\mu}{\pi d^4} \tag{1.8}$$

where Q is the volumetric flow rate, ΔP is the pressure drop over length, L, and d is the channel diameter. The heat flux removed from a channel is given by

$\dot{q}/A = q'' = h\Delta T$, where $h = Nu\,k/d$ is the heat transfer coefficient, k is the fluid thermal conductivity, Nu is the Nusselt number, and ΔT is the difference in temperature between the wall of the channel and the mixed mean of the fluid at distance L.

The required enhancement in thermal conductivity for a given increase in viscosity is found by holding $L, q'', \Delta T, Q,$ and Nu constant between the base fluid and nanofluid cases, allowing the channel diameter to increase to keep ΔT constant, and requiring that ΔP not change. By formulating the ratios $\Delta T_{nf}/\Delta T_f$ and $\Delta P_{nf}/\Delta P_f$ and solving for d_{nf}/d_f and combining, a single equation of the enhancements is generated. The relationship between the enhancements is found to be $(\mu_{nf}/\mu_f) < (k_{nf}/k_f)^4$, which in terms of enhancement factors corresponds to $(1 + C_k\varphi)^4 > (1 + C_\mu\varphi)$. Assume $C_k\varphi$ is small compared to 1 to get, $(1 + 4C_k\varphi) > (1 + C_\mu\varphi)$. This shows that C_μ can be up to 4 times larger than C_k.

If the channel size is not allowed to change, then the relationship can be derived by requiring the increase in pumping power to drive the fluid to be less than the increase in thermal power removed. Thus, W_{nf}/W_f must be less than $\dot{q}_{nf}/\dot{q}_f$. By holding everything else but the viscosity and thermal conductivity constant, a direct relationship is found where $(\mu_{nf}/\mu_f) < (k_{nf}/k_f)$. Thus C_μ must be smaller than C_k. From the effective medium theories C_μ is expected to be 2.5 and C_k is expected to be 3, yielding a favorable fluid.

1.5 Experimental Results

The first measurements of the thermal conductivity and viscosity of dilute dispersion of nanoscale particles in fluid were completed by Masuda et al.[36] They measured enhancements of SiO_2, TiO_2, and Al_2O_3 in water at various concentrations and temperatures. Thermal conductivity enhancements were at or below the H-C model for the low conductivity SiO_2 and consistent with the model for TiO_2. Their

measurements of Al_2O_3 showed a 30% increase with 4.3% $_{vol}$ concentration and were above the predictions by the H-C model, but fit well with the Fricke model for ellipsoids. Their measurements of viscosity showed large increases for the SiO_2 and Al_2O_3 increases by 3 times for 2.5%$_{vol}$ fractions. For the TiO_2 the increases in viscosity with particle loading followed Einstein's model well. The use of nanofluids for as heat transfer fluids was proposed in a theoretical study by Choi et al.[37] calculating the potential enhancement from the Hamilton Crosser model for varying volume concentration and sphericity.

Interest first began in nanofluids for cooling applications when Eastman et al. [38] found enhancements of 6% for Al_2O_3 and 12% for CuO per 1%$_{vol}$ concentration in water and 15% per 0.01%$_{vol}$ concentration for Cu in oil. These were well above the expected enhancements from Maxwell effective medium theory of 3% per 1%$_{vol}$ concentration for dilute suspensions of high thermal conductivity nanoparticles, but the values of Cu in oil were incredibly high sparking much interest in the scientific community.

The same group measured the thermal conductivity of Al_2O_3 and CuO in water and ethylene glycol and compared the data to the Hamilton Crosser model for spheres and for cylinders.[39] They found that the enhancement from Al_2O_3 in both water and ethylene glycol fit the model for spheres well. They showed that CuO was well above the model for both base fluids using a k_p of 2 W/mK. However, the thermal conductivity of CuO is close to 20 W/mK. Using this value the measured enhancement fits the model well for water and is slightly higher for the ethylene glycol.

Wang et al. [40] measured the thermal conductivity and viscosity of Al_2O_3 and CuO in water, vacuum pump fluid, engine oil, and ethylene glycol. They found for CuO the enhancements to match with the H-C model. For Al_2O_3 the enhancements in ethylene glycol and engine oil were at about 5% per 1%$_{vol}$ concentration with for water and pump fluid the enhancements matched the H-C model. For viscosity they

found increases of 12% per $1\%_{vol}$ concentration for water and about 8% for ethylene glycol, larger than the increase for thermal conductivity.

1.5.1 Temperature Dependence

The effect of temperature on the thermal conductivity of nanofluids has been highly controversial. Das et al. [41] measured Al_2O_3 and CuO nanoparticles in water at 1% and $4\%_{vol}$ concentrations using a temperature oscillation method. They found the thermal conductivity enhancements for Al_2O_3 increased from 2% at 21 ^oC to 10.8% at 51 ^oC for $1\%_{vol}$ concentration and from 9.4% at 21^oC to 24.3% at 51 ^oC for $4\%_{vol}$ concentration. The enhancements for CuO increased from 6.5% at 21 ^oC to 29% at 51^oC for the $1\%_{vol}$ concentration and from 14% at 21 ^oC to 36% at 51 ^oC for the $4\%_{vol}$ concentration. However, it was not apparent whether aggregation was occurring in their measurements due to the extra time needed for heating the nanofluids, which is another possible cause for increased thermal conductivity.

The same group shortly after looked at the enhancements of Au-thiolate in toluene and Au and Ag-citrate in water using a transient hotwire method.[42] For the Au-thiolate in toluene they found the enhancement to increase by an additional 2 to 3% over the base fluid measured value between 30 ^oC and 60 ^oC for the three concentrations measured: 0.011%, 0.008% and $0.005\%_{vol}$ concentration. However, they also measure the thermal conductivity of toluene as increasing by 4% even though it should actually decrease by 6% [43] showing a 10% error in their measurements and an incorrect trend. For the Au-citrate at 0.00013% and Ag-citrate at $0.001\%_{vol}$ concentration in water, the enhancement increases by an additional 1 to 1.5% over the base fluid measured value, while for the 0.00026% Au-citrate in water the enhancement increases by an additional 4% over the base fluid measured value when the temperature is increased from 30 ^oC to 60 ^oC. However, they measure the thermal conductivity of water as increasing by 10% over that temperature range when it should only increase by 5%, showing an error of 5% in their measurement.

Therefore, all of their measurements are within their errors and no conclusions can be made.

Li et al. [44] used a parallel disk method to measure the thermal conductivity of Al_2O_3 and CuO at concentrations between 2% and 10% by volume between 27.5 ^oC and 34.7 ^oC. In all of the cases they found the enhancement in thermal conductivity to increase an additional 10 to 15% over the base fluid value. However they did not describe how they prevented natural convection within the chamber nor did they describe the process of measuring the nanofluid thermal conductivity and if aggregation could have been taking place.

The previous three studies left many open questions about the variation in thermal conductivity enhancement with temperature. Zhang et al. [45] utilized a short-hot-wire method to measure Al_2O_3, ZrO_2, TiO_2, and CuO particles in water at mass fractions ranging from 10 to 40% and temperatures ranging from 10 to 50 ^oC. For each of the sample no increase in enhancement with temperature was observed. Their measurements of water showed the expected increase with temperature found in literature.

Yang et al. [46] measured the temperature dependence of Bi_2Te_3 nanorods suspended in FC72 using a 3ω method between 5 ^oC and 50 ^oC. They found no additional enhancement with temperature and found that effective medium theory fit their data well. They measured the expected values and trends with temperature for the thermal conductivity of FC72.

Venerus et al. [47] used a forced Rayleigh scattering technique to measure the thermal conductivity dependence on temperature of Au in water and Al_2O_3 in petroleum oil between 30 ^oC and 80 ^oC. Due to the optical nature of the measurement technique it was necessary for the volume fractions to remain small and the fluid to remain completely transparent without aggregation. They found in both cases that the enhancement fit well with effective medium theory and that there was no increase in enhancement with temperature.

As these last studies suggest, there is actually no direct increase in the thermal conductivity enhancement due to temperature. It is more likely another mechanism was causing the enhancements measured in the earlier studies possibly indirectly related to temperature.

1.5.2 Time Evolution

Due to the need for a fluid in thermal applications to have a long lifetime, several groups have studied the time evolution of the nanofluid thermal conductivity. Multiple groups found significant initial enhancements in the thermal conductivity that decrease greatly over time. The particle sizes for these studies were typically 10 nm or less, while the aggregate sizes were found to become >1 μm. In the worst cases, a significant amount of settling was noticed.

Hong et al. [48] measured the enhancement to decrease from 14% to 9% in a $0.2\%_{vol}$ concentration of Fe in ethylene glycol nanofluid after an hour with aggregate sizes increasing from 1.2 to 2.3 μm. Karthikeyan et al. [49] measured an enhancement decrease from 20% to no enhancement in $0.3\%_{vol}$ and $0.8\%_{vol}$ concentration of CuO in water after 20 min and noticed a significant amount of settling over time. Fortenberry et al. [50] measured a decrease in enhancement of 4% in both a $10\%_{vol}$ and $15\%_{vol}$ concentration of alumina in water after 15 and 100 days, respectively.

Aggregation is the likely cause of the time evolution of the thermal conductivity. As the aggregates become large (>1μ) settling occurs causing a decrease in particle concentration and thermal conductivity. Potentially large enhancements can occur in stabilized solutions if aggregates are less dense and small enough to stay in solution.

1.5.3 Aggregation

Recently magnetic nanofluids have shown great promise in the ability to tune thermal properties. Philip et al. [51] conducted an experimental study on aggregation. They utilized magnetic fields to bring stabilized magnetite particles into linear aggregates and measured a maximum angular averaged enhancement of 400% at 6.3%$_{vol}$ concentration corresponding to 64% per 1%$_{vol}$ concentration. They observed over aggregation at higher magnetic fields causing the thermal conductivity to decrease as predicted by Prasher et al. [52]

The particles in a nanofluid are smaller than the wavelength of light. Thus, a nanofluid is optically transparent when no aggregation is present. Data from research groups using optical methods to measure transparent nanofluids show thermal conductivity consistent with EMT. Putnam et al. [53] used an optical beam deflection technique to measure fullerenes in toluene and Au in ethanol and toluene. Their measurements were consistent with EMT. Venerus et al. [47] used forced Rayleigh scattering to measure the thermal diffusivity and conductivity of Au in water and Al_2O_3 in petroleum oil and found their measurements consistent with EMT. A recent benchmark study consisting of 34 research groups has shown that for a variety of stable, well-dispersed nanofluids, the thermal conductivity is well modeled through the Maxwell Effective Medium Theory.[54]

1.5.4 Viscosity

Even though viscosity is an important property for use in a microchannel heat exchanger, only a few groups measured the viscosity of the nanofluids they studied. The researchers that did measure the viscosity typically found the increase to be about 10% per 1%$_{vol}$ concentration. Wang et al. [40] found an increase of 12% for Al_2O_3 in water and 10% for Al_2O_3 in ethylene glycol. Prasher et al. [55] found an increase of 10% per 1%$_{vol}$ concentration for Al_2O_3 in propylene glycol and calculated the limiting case for nanofluid favorability to be when the enhancement in viscosity is greater than

four times the enhancement of the thermal conductivity. Lee et al. [56] found an increase of 1.74% per $0.1\%_{vol}$ concentration for Al_2O_3 in water. Garg et al. [57] measured Cu in ethylene glycol and found an increase in viscosity of 10% per $1\%_{vol}$ concentration.

Past experimental work has found typically larger enhancements than predicted by effective medium theories for both thermal conductivity and viscosity. Temperature effects measured by some groups have been shown to be likely due to another mechanism indirectly related to temperature. The thermal conductivity has been shown to increase with aggregation, but decrease if the aggregates become dense and large causing settling.

1.6 Theoretical Work

Due to the widely scattered of data, much of which early on in the field of nanofluids for heat transfer (before the year 2000) showed a higher thermal conductivity than expected from effective medium theory, multiple models were developed to describe the increases based on the trends reported.

1.6.1 Brownian Motion and Micro-convection

Particles in a fluid experience Brownian motion due to the constant bombardment of the fluid molecules. Due to the apparent temperature dependence of the thermal conductivity measurements of Das et al. [41] and the increase in Brownian motion with temperature, it was considered to be a likely reason for the enhancement. Keblinski et al. [58] showed that the movement of the particles would be much slower than the heat diffusion and thus would not increase the apparent thermal conductivity. Xuan et al. [59] created a model confirming the enhancement due to Brownian motion; however an apparent algebraic error in the model formulation leads to the excess modeled enhancement.

Once it was determined that the movement of a single particle could not cause a detectable increase in the thermal conductivity, researchers focused on the effect of two particles moving past each other causing micro-convection. Prasher et al. [60] developed an empirical model to describe enhancement from micro-convection to describe the apparent temperature dependence. Evans et al. [61] showed through a molecular dynamics simulation that micro-convection does not lead to thermal conductivity enhancements.

1.6.2 Liquid Layering

An ordered molecular layering at a solid-liquid interface of liquid molecules has been shown to occur with layering 3 – 6 molecules thick.[62] It was proposed by Keblinski et al. that the layering of liquid molecules on the surface of the nanoparticles would result in a larger apparent volume fraction and effective thermal conductivity. However, they also noted that the effect would be much smaller than previously reported enhancements and would only be a minor factor that is reduced significantly with increasing particle size (d_p > 20 nm). Yu et al. [63] expanded Maxwell equation for effective medium theory to include the effect of molecular layering and found that the thermal conductivities still under predicted experimental data even at the highest possible enhancements with liquid layers of 2 nm and layer thermal conductivities equal to the particle thermal conductivity. Xue et al. [64] conducted a molecular dynamics simulation and showed that even in a significantly confined fluid no apparent enhancement existed from liquid layering.

1.6.3 Near Field Radiation and Ballistic Transport

Due to the nanoscale size of the nanoparticles, the particle diameter in smaller than the mean free path of the phonons. Thus the phonons will move ballistically within the particle rather than diffuse.[58] If the ballistic phonons could then travel

from one particle to another it would greatly increase the bulk thermal conductivity. Ben-Abdallah [65] conducted a theoretical study of the ballistic phonon transport and found that the additional thermal conductance was of the order of 10^{-12} W/K, not enough to explain the larger measured enhancements.

1.6.4 Aggregation

Aggregation is an irreversible process in which initially dispersed particles join together.[66] The aggregate size increases with time as more particles join. In colloids, particles are dispersed in fluid and diffuse under Brownian motion. The particles act independently until they come close enough to experience Van der Waals forces and stick together. Particles may ricochet off each other multiple times before actually joining into an aggregate due to the electrostatic barrier.

1.6.4.1 Fractal and Percolation Theory

Fractal theory offers a way of modeling the complicated branched structure of the aggregates. Fractal theory is based on the random structure of the object being studied. The structure must contain random features at all length scales and never contain smooth contours down to a lower limit for real physical systems. The fractal dimension for a particular fractal object comes from the power law and describes how the structure changes density as the length scale changes. Simulated images of particle aggregates and various fractal dimensions are shown in Figure 1.5. Different fractal dimension are achieved depending on the type of aggregation. Diffusion limited aggregation produces fractal dimensions of 1.8. Reaction limited aggregation produces fractal dimensions of 2.4.

Percolation theory allows for the modeling dynamics, such as diffusion and phase transition, within stochastic systems, such as randomly oriented composites,

porous media, or fractal clusters. Through the fractal properties of the media and statistical theory, properties such as conductance can be calculated for disordered systems based on a random walk analysis. As the particles cluster close together the heat travels more easily from particle to particle bypassing the fluid allowing for percolation to occur with or without the particles touching.

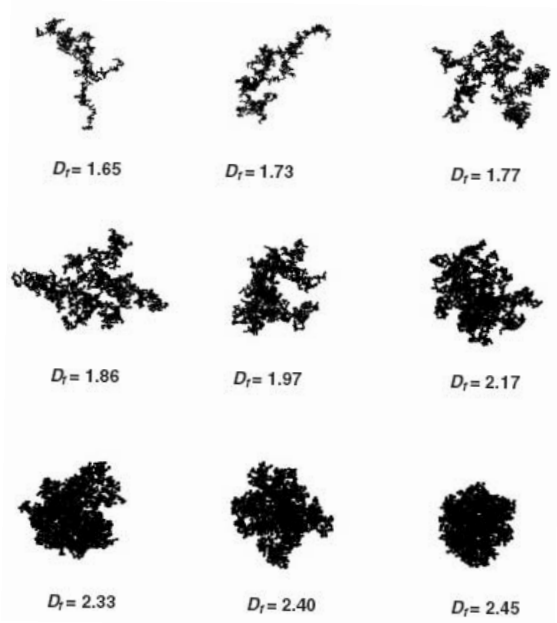

Figure 1.5: Computer simulated 3D aggregates with different fractal dimensions projected onto 2D plane.[67]

1.6.4.2 Application to Nanofluids

The clustering of particles into percolating aggregate structures could cause an increase in the nanofluid thermal conductivity. Keblinski et al.[58] showed from simple effective medium theory that enhancements of 30% for each $1\%_{vol}$ concentration are possible for very loosely packed aggregates with liquid layers separating the particles undergoing ballistic transport between the particles. For

closely packed aggregates, the affected volume for each aggregate is reduced and the enhancement reduces to 5% for each $1\%_{vol}$ concentration.

Wang et al. [68] proposed applying fractal theory to calculate the effective thermal conductivity of aggregated nanofluids. They included confinement effects of the nanoparticle's size and a monolayer of fluid absorption on the nanoparticle surface for the individual particle thermal conductivity. They used fractal theory equation below to estimate the volume fraction of particles in the aggregates, $\varphi_{p,agg}$:

$$\varphi_{p,agg} = \left(\frac{R_a}{r_p} \right)^{d_f - 3} \tag{1.9}$$

where R_a is the radius of the aggregate, r_p is the particle radius, and d_f is the fractal dimension. They developed a model for the aggregate thermal conductivity based on integrating the Bruggeman model over the aggregate size distribution. They calculated the nanofluid thermal conductivity using the Maxwell model and found a thermal conductivity enhancement of 30% per $1\%_{vol}$ concentration.

Prasher et al. [69] built upon the fractal theory and split the aggregate into non-percolating dead-ends and a percolating backbone structure. A schematic of the separation of the two subsets in shown in Figure 1.6 with the backbone particles shown in black and the dead-ends shown in gray. They continued using the Bruggeman model for the dead-ends and then used composite theory for randomly oriented ellipsoid particles for the backbone structure aggregate. For a fractal dimension of 1.8 and chemical dimension of 1.4, they found the enhancements approached a maximum of 10% per $1\%_{vol}$ concentration. For a higher chemical dimension the enhancements reached as high as 15% per $1\%_{vol}$ concentration at a fully aggregated state.

Evans et al. [70] expanded upon the previous work by studying the effect of the particle thermal conductivity and Kapitza radius of the interfacial resistance. They found that as aggregation progressed the particle thermal conductivity became more important and found the enhancement at a fully aggregated state increased from 9% to 22% per $1\%_{vol}$ concentration when the particle thermal conductivity went from 100 times to 200 time the base fluid thermal conductivity. When the ratio of the Kapitza radius to the particle radius was increased from zero to 0.1 and 1 nm, the enhancement at a fully aggregated state decreased from 9% to 8% and 5%, respectively, per 1%vol concentration.

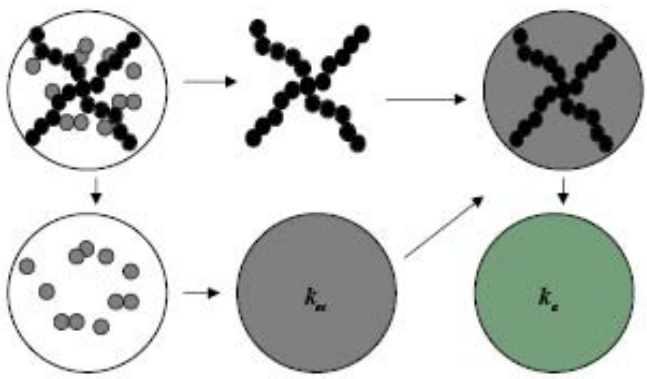

Figure 1.6: Schematic of a single aggregate with effective thermal conductivity k_a consisting of the backbone particles shown in black and dead-end particles shown in gray. The aggregate is decomposed into dead ends with the fluid and the backbone. Thermal conductivity of the aggregate only with particles belonging to the dead ends, k_{nc} is calculated using the Bruggeman model. Linear chains are embedded inside a medium with effective conductivity of k_{nc}. [70]

Prasher et al. [52], showed the aggregation time constant to be inversely proportional to the fluid temperature and particle volume concentration and directly proportional to the fluid viscosity. If the concentration is doubled the particles will reach the same point in aggregation in half the time. As the temperature is increased

the viscosity of the fluid decreases producing an even larger dependence on temperature. The temperature dependence of aggregation is likely the cause of the measured variations with temperature as the higher temperature fluids will aggregate faster increasing their effective thermal conductivity.

The effect of aggregation on the bulk viscosity of the fluid has been measured by various research groups. De Rooij et al. [71] found using creep experiments that once the aggregates reach a quasi-equilibrium structure the viscosity increases by 6 orders of magnitude in a $4.3\%_{vol}$ concentration. In steady, shear measurements, they found the viscosity to greatly reduce to an increase of less than 1 order of magnitude.

Variations in the fractal dimension of aggregates due to shear flow have been studied by multiple research groups. Hoekstra et al. [72] measured the fractal dimension of aggregates formed with and without shear conditions and found fractal dimensions of 2.2 and 1.7 respectively for the same sample. Potanin et al. [73] simulated the deformation of the aggregates in shear and showed an increase in the fractal dimension from 1.85 to 2.16 when shear was applied.

1.6.5 Particle Diffusion

Thermal diffusion, also referred to as thermophoresis, thermomigration, thermodiffusion, and the Soret effect, occurs when a binary or higher order mixture is subjected to a temperature gradient. Thermal diffusion is due to the variation in kinetic energy across the gradient allowing particles from the hot region to diffuse further than particles in the cold region. Thus, the particles diffuse towards the cold region of the fluid causing a concentration distribution within the nanofluid at steady state. Initially it was proposed that the resulting mass flux may contribute to the enhanced thermal conductivity, multiple researchers have shown this to be negligible.[58] The diffusion strongly influences the local particle concentration. Since the local viscosity, thermal conductivity, and aggregation all depend on the local concentration the diffusion will cause gradients in each of these.

Buongiorno [74] developed a model for convective transport in nanofluids. They studied many mechanisms present in particle laden fluid flow including the particle and fluid slip mechanisms of turbulent transport from eddies, Brownian diffusion, thermophoresis, diffusiophoresis, Magnus effect from rotation, fluid drainage at a wall, and gravity. They determined that in a turbulent flow the turbulent transport dominates all other mechanisms. When turbulent effects are not important Brownian motion and thermophoresis dominate.

Wen and Ding [75] studied the simulated effect of particle migration on the heat transfer of nanofluids flowing through microchannels. They took into account shear effects, shearing induced viscosity gradient, and diffusiophoresis. They did not include thermal diffusion. The shear effects caused large variations in concentration across the channel cross section with particles tending to move towards the center of the tube. The diffusiophoresis worked to counteract this effect as the concentration variation grew. For smaller particles which diffuse faster, the concentration variations were greatly reduced. Based on the relative importance of thermophoresis versus diffusiophoresis from Buongiorno, if the diffusiophoresis had been combined with thermophoresis a concentration profile would have remained even at smaller particle sizes.

Savino and Paterna [76] modeled convective transport of nanofluids subjected to thermal diffusion in a temperature gradient between two differently heated parallel plates. They showed that the combination of concentration and thermal gradients could create circulation based on the orientation of the cell.

1.7 Objectives and Scope of This Study

Recent data and simulations show a large dependency of the thermal conductivity on particle aggregation. Simulations by various research groups show the potential for large variations in concentration due to thermal diffusion of the particles in a temperature gradient. Due to the interdependencies of the particle

concentration on aggregation and aggregate size on thermal diffusion, it is important to understand the potential coupled effects. To understand these interdependencies, two experimental investigations are employed: a Monte Carlo simulation is conducted and the Onsager relations for particle and heat flux are solved.

In Chapter 2, the first experimental investigation measures the effect of a temperature field on the thermal conductivity distribution. This measurement looks at the joint effects on thermal conductivity of the combined thermal diffusion and aggregation over time across the temperature field.

In Chapter 3, the second experimental investigation looks at the aggregate structure and size for various concentrations and temperatures. Three techniques are used for this investigation. First, dynamic light scattering give the initial size distributions. Second, scanning electron microscopy gives images of the initial structure of the permanent aggregates. Third, static light scattering gives the fractal dimension of the aggregates over time at two length scales and various concentrations and temperatures. Finally, a Monte Carlo simulation is completed for these scenarios to obtain a prediction of the aggregate size over time at the temperatures and concentrations measured.

In Chapter 4, the measurements are simulated with a Monte Carlo simulation in three ways. First, only thermal diffusion is simulated. These results are compared to the solution to the Onsager relation between the particle flux and heat flux. Second, just aggregation is simulated in an isothermal environment. These results are compared to the measurements of aggregate size and structure. Finally, the full Monte Carlo simulation is completed combining thermal diffusion and aggregation. The effective properties are calculated from the aggregate and concentration information. These results are compared to the thermal conductivity measurement.

PAGE INTENTIONALLY LEFT BLANK

Chapter 2

Thermal Conductivity Measurement

2.1 Introduction

The nanoparticles in nanofluids for heat transfer are subjected to two main physical phenomena: aggregation and thermal diffusion. As the particles move from Brownian motion, they come into close proximity to each other allowing for interaction and aggregation. When the nanofluid is subjected to a temperature gradient such as those in a heat exchanger, the particles will migrate towards the colder region. As both of these phenomena progress, they will impact each other. Aggregation changes the effective diameter of the particles which will reduce Brownian motion and diffusion. Thermal diffusion will create a concentration gradient which will alter the local aggregation time constant. Each of these effects will have a major impact on the thermal conductivity of the nanofluid and the variation in thermal conductivity within a channel.

Traditional thermal conductivity measurements cannot decipher these effects and how they interact due to an inability to measure microscopic variations in thermal conductivity across a sample. This chapter describes advanced techniques for the measurement of nanofluid thermal conductivity distributions with high spatial resolution. The two dimensional temperature distribution of a nanofluid held between copper plates subjected to uniform heating is measured over time using diffraction-limited infrared microscopy. It is found that the temperature gradient, and thus

thermal conductivity, varies spatially and temporally as aggregation and thermal diffusion progress.

2.2 Experimental Setup

A calibrated high-resolution infrared microscope (QFI / Infrascope) measures the full-field temperature distribution. Figure 2.1 shows a schematic of the experimental system for high resolution nanofluid thermal conductivity measurements. The IR focal plane array uses an array of InSb elements (256 x 256) with detection wavelengths of 2 - 5.5 μm and 0.1 K minimum temperature sensitivity. A 15x SiGe objective with numerical aperture of 1.0 provides a diffraction limited spatial resolution of 2.8 μm. Two 1 inch square, ¼ inch thick, copper plates spaced 500 μm apart by glass spacers hold the nanofluid. The average Rayleigh number of the system with water is 160, which is much less than the limit of 1000 for buoyancy-driven flow to stay weak and heat transfer to be primarily through conduction. A 250 μm thick, 1 inch square, thin-film, Kapton encapsulated heater (Omega / KHLV-101) generates joule heat at a constant rate that conducts perpendicularly across the nanofluid and dissipates into a temperature controlling thermoelectric cooler and water cooled heat sink. A heat flux sensor (Omega / HFS-3) between the cold copper plate and the heat sink monitors any variations from the applied power to ensure minimal heat loss occurs. A temperature controller is used to control the temperature of the thermoelectric cooler and the cold copper plate. Five thermocouples are placed along the heat flux path, two on the hot copper plate, two on the cold copper plate, and one on the thermoelectric cooler. A humidification chamber reduces evaporation, which would alter the fluid concentration and increase the heat loss.

The uncertainty in the applied power is 2% and the measured heat flux is measured to be within 1%. The uncertainty in the calculated slope of the temperature distribution is 0.1% and 1.5% for the average and local thermal conductivities, respectively. The uncertainty in the calibration temperature is 0.5 ^{o}C across the cavity

leading to an uncertainty in the slope of 3%. These lead to an uncertainty in the calculated thermal conductivity of 5% for the average value and 7% for the local values. The method of determining the local values is described in Section 2.3.

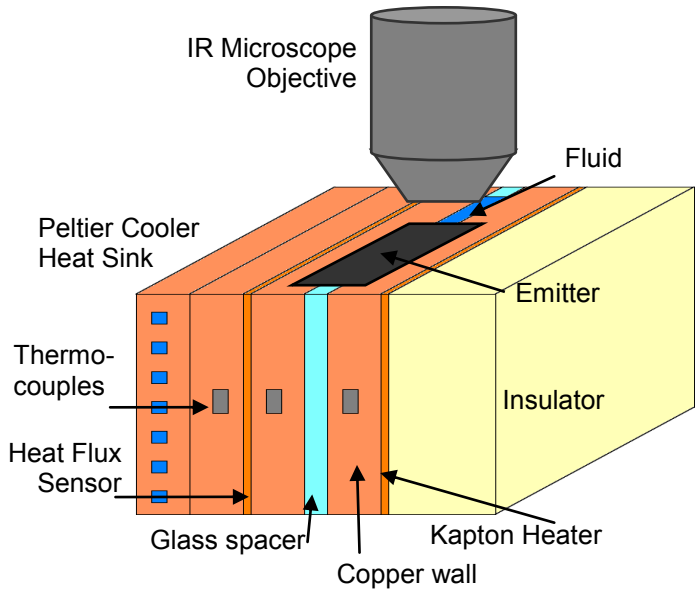

Figure 2.1: Schematic of infrared microscope experimental setup showing nanofluid held between copper plates and glass spacers. A heat flux is applied across the nanofluid with a thin Kapton heater, measured on the opposite side with a heat flux sensor, and dissipated into a thermoelectric cooler and heat sink. The temperature is monitored with thermocouples on the copper plates.

A 20 μm thick polyester film covers the fluidic opening, serves as a uniform emissivity emitter, precisely defines the emission location, and reduces fluidic evaporation. The heat traveling through the film and bypassing the fluid is calculated using a thermal resistor network as less than 0.06% of the applied heat. A COMSOL finite element thermal model predicts the variation in measured temperature between the emitter and fluid. The difference in thermal conductivity is calculated from the temperature distribution to be less than 3% at any point in the cavity width and less

than 1.5% on average. To obtain the thermal conductivity, 256 temperature distribution lines are averaged and the gradient calculated.

The emissivity of the experimental system is calibrated prior each measurement set at 20 ^{o}C and 60 ^{o}C, temperatures characteristic of the measurement temperature gradient with a radiance reference taken at 45 ^{o}C. The emissivity variation with temperature for each pixel is calculated and stored by the instrument software. The temperature controller is set to the desired temperature and the heater power is adjusted until a uniform temperature is reached. Typically about 15 minutes elapses during the calibration process. The calibration is applied to the measurement images and corrects for reflected signal components and emissivity spatial and temperature dependencies. A typical thermal image is shown in Figure 2.2.

Heat loss from the experimental apparatus to the environment is due to natural convection from the outer surfaces, conduction through the back insulator, and minor fluid evaporation. These losses modeled through a thermal resistive network are found to be less than 1% of the applied heating power and are systematically eliminated as part of the data extraction procedure. The ability to precisely determine the temperature-dependent conductivity of pure water is verified before each measurement. The thermal conductivities are found to have repeatability to within 5% of the average value.

2.3 Measurement Results

The local thermal conductivity of the nanofluid is calculated from the temperature distribution using Fourier's Law for heat diffusion, $q'' = -k\nabla T$, where ∇T is the local slope of the ensemble averaged temperature distribution and q'' is the estimated actual heat flux. The total temperature difference across the cavity is about 25 ^{o}C with a heating power of 4 W/cm^2 and a mean temperature of 50 ^{o}C. Emitter film curvature at the edge of the copper plates prevents the evaluation of the outer 70 μm of the sample. The thermal conductivity profile is evaluated by discretizing the

temperature distribution into nine 40 μm divisions with 50% overlap and performing a linear fit on each division to obtain the local slope. The method for the preparation of the nanofluid is discussed in Chapter 3.

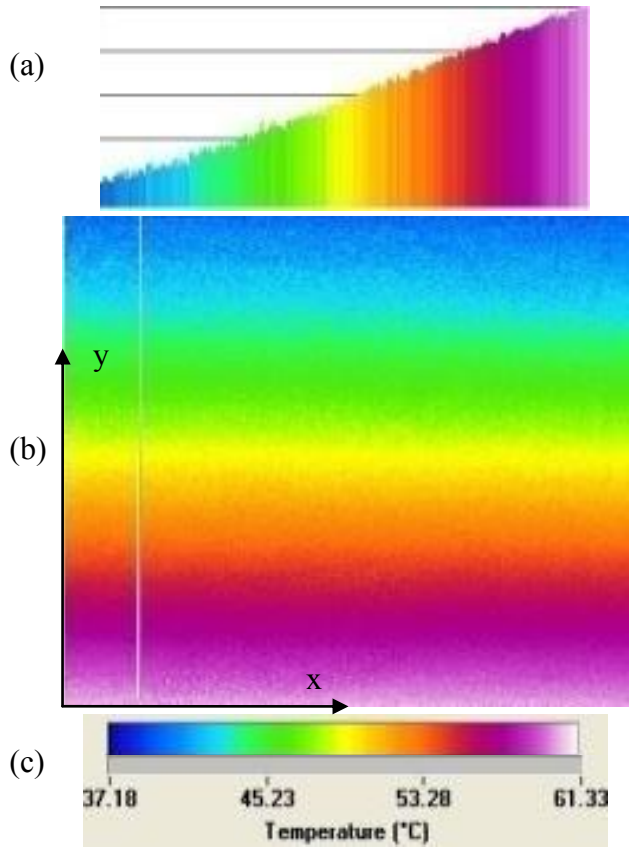

Figure 2.2: Typical image of measured cross-sectional temperature distribution of a nanofluid of alumina suspended dispersed in deionized water (Alfa Aesar / 12733) subjected to a 4W/cm^2 heat flux: (a) temperature distribution at white line, (b) temperature distribution image, and (c) temperature color scale.

The average thermal conductivity for three different concentrations of 40 nm alumina nanoparticles dispersed in deionized water (Alfa Aesar/12733) is plotted over time in Figure 2.3. For each volume concentration the initial experimentally measured

thermal conductivity starts near the prediction of effective medium theory. For the $1\%_{vol}$ concentration the thermal conductivity enhancement stays between 1.5% and 3.2% over the one hour period with the variation within the uncertainty of the measurement.

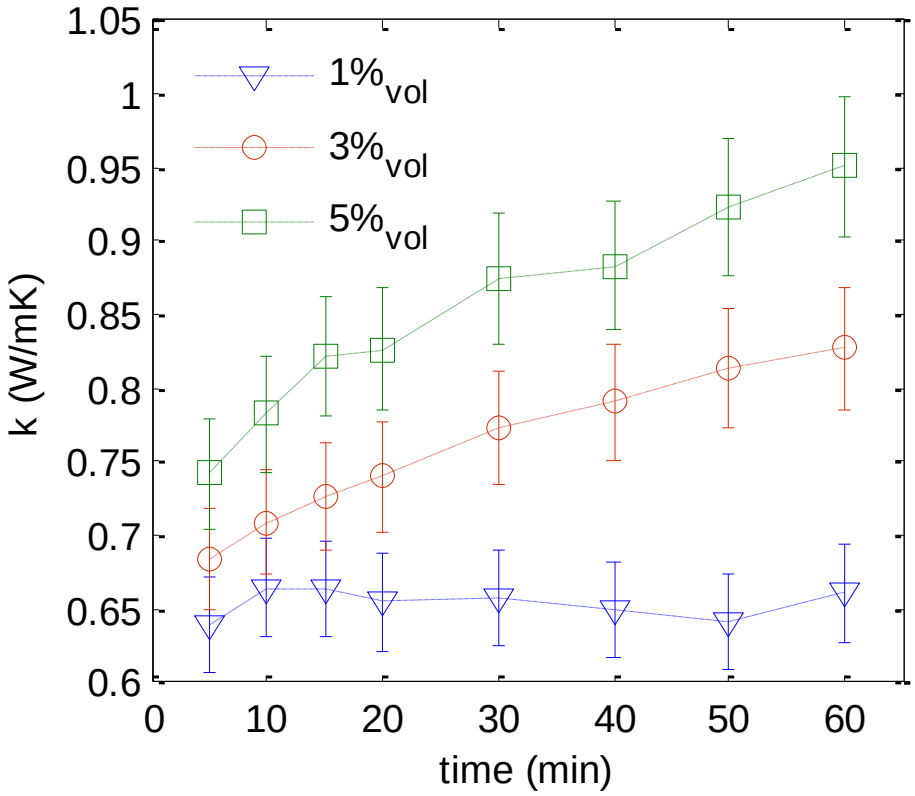

Figure 2.3: Plot of the time dependence of the average thermal conductivity for the three concentrations of nanofluid consisting of 40 nm alumina nanoparticles dispersed in deionized water (Alfa Aesar / 12733).

For the $3\%_{vol}$ concentration, the enhancement increases from about 7% to 30% over the course of the one hour measurement, increasing from an value consistent with effective medium theory to three times the predicted enhancement. The $5\%_{vol}$ concentration enhancement increases from 16% to 48% after an hour. Again the enhancement increases from effective medium theory to triple the prediction. These

overall increases in thermal conductivity with time are due to the aggregation of the particles within the fluid. At the lower concentration, not enough aggregation occurs to see an effect. At higher concentrations the effect of aggregation on the thermal conductivity is evident.

Figure 2.4 shows the distribution of the measured nanofluid thermal conductivity increase from the initial values for each concentration at various times. Small water droplets condensing on the emitting film during the measurement create slight waviness in the plots which slightly skew the calculations for the $5\%_{vol}$ case, but the waviness is within the error of the measurement and does not affect the overall conclusions. As before, the $1\%_{vol}$ concentration yields no discernable changes in conductivity over time throughout the entire spatial domain considering the experimental uncertainty. No effect of aggregation or thermal diffusion is evident.

The $3\%_{vol}$ concentration yields an increase in thermal conductivity over time with a larger increase in the colder region of the fluid. The increase over the course of the hour long measurement is 25% in the cold region and 10% in the hot region. As thermal diffusion occurs the concentration in the cold region of the nanofluid increases causing more aggregation to occur increasing the thermal conductivity more. This result shows the effects of both aggregation and thermal diffusion and more importantly the effect of thermal diffusion on aggregation.

The $5\%_{vol}$ concentration yields a 30% increase in thermal conductivity over time across the entire spatial domain over the course of the hour long measurement. The effect of aggregation is most apparent in this case. It is probable that between sonication and starting the measurement, while the system is calibrated to the new sample, some aggregation occurred. The larger aggregates experience much slower thermal diffusion, while the higher concentration experiences much faster aggregation. This result shows the effect of aggregation on thermal diffusion.

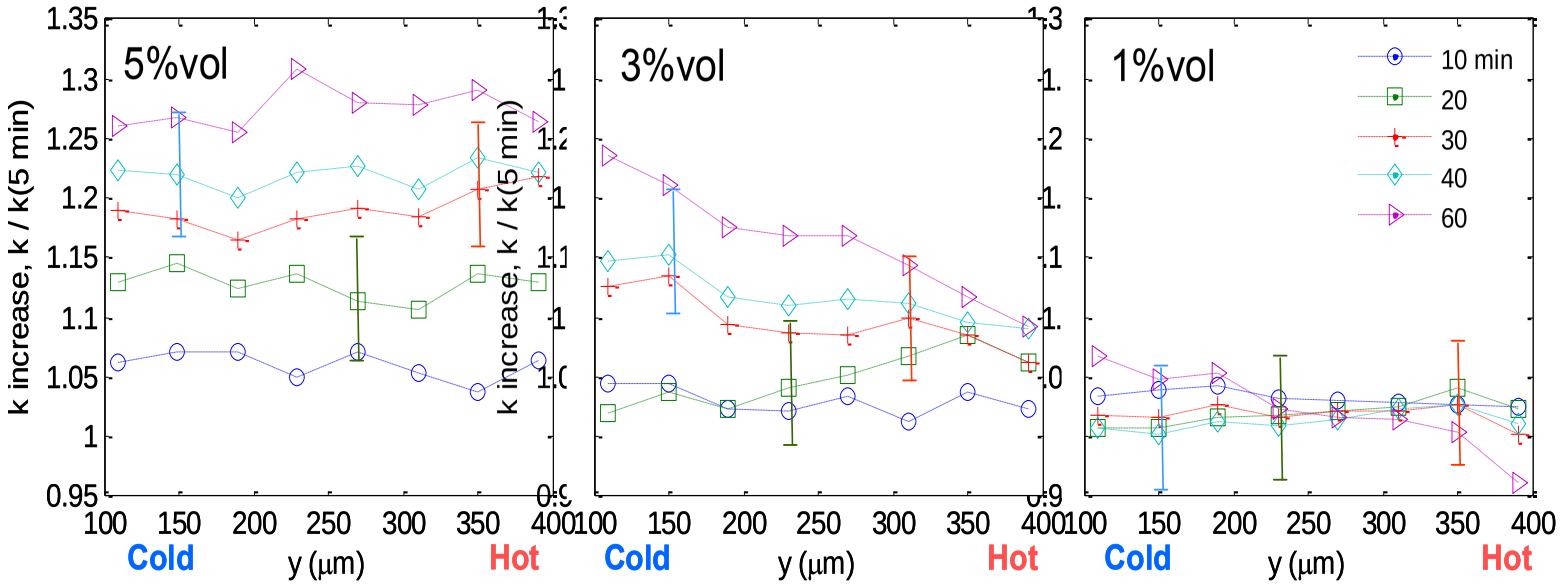

Figure 2.4: Measured time dependence of the full field thermal conductivity increase of a nanofluid consisting of alumina particles dispersed in deionized water (Alfa Aesar / 12733) in a temperature gradient for volumetric concentrations of (a) 5%, (b) 3%, and (c) 1%.

2.4 Conclusions

The full field temperature distribution allowed for the extraction of information not obtainable using other thermal conductivity measurement techniques. From the average measured thermal conductivity over time, it is shown that aggregation in stable nanofluids significantly increases the thermal conductivity of the fluid at concentrations above $1\%_{vol}$. From the thermal conductivity profile over time, it is shown in the $3\%_{vol}$ concentration that thermodiffusion affects the amount of aggregation across a temperature gradient by imposing a concentration distribution and variation in the aggregation time constant. The thermal conductivity distribution is affected through its direct relationship with the concentration and progress of aggregation. In the $5\%_{vol}$ concentration, it is shown that the aggregation affects the amount of thermal diffusion due to the increased particle size impeding the Brownian motion.

PAGE INTENTIONALLY LEFT BLANK

Chapter 3

Aggregate Characterization

3.1 Introduction

Aggregation has been identified as the most probable reason for the nanofluid thermal conductivity and viscosity enhancements beyond the basic effective medium theories. The enhancements achieved depend on the aggregate size and structure. The progression of aggregation is known to depend strongly on the particle volume concentration and fluid temperature. It is important to separate the effects of aggregation from the thermal diffusion and understand them individually to obtain correct predictions for the effective thermal conductivity and viscosity. A study of the aggregation progression and structure at various isothermal conditions is necessary for a full understanding of the thermal conductivity data.

This chapter describes two techniques to determine the initial state of the nanofluid and one technique to study the aggregate progression and structure at various concentrations and temperatures. Dynamic light scattering yields the initial particle size distribution and shows the presence of permanent aggregates in the nanofluid. Scanning electron microscopy gives a visualization of the particles and permanent aggregates as they appear in suspension and allows for the calculation of the fractal dimension of 2.5 for the aggregates. Static light scattering gives the

average fractal dimension of the aggregate formations over time at different length scales for each of the volume concentrations at different temperatures.

3.2 Nanofluid Preparation

The nanofluid has 20% weight concentration 40 nm alumina particles in H_2O with less than 1% nitric acid for stabilization (Alfa Aesar / 12733). The fluid is diluted with deionized water to the desired volume concentrations. Prior to the measurements the nanofluid is sonicated for 4 h. To prevent variations in the lapse in time between sonication and the measurement the fluid is heated to the desired temperature during sonication. An estimated 15 minutes elapses between sonication and measurements for each case as the fluid is loaded into the light scattering set-up and flow effects are allowed to subside. The nanofluid is stable with only minor settling after a week. A subset of the particles is initially aggregated and large enough to scatter visible light though the fluid remains partially transparent as shown in the image of the diluted nanofluids in Figure 3.1. As the fluid is diluted it becomes more transparent allowing more light to shine through the fluid.

The pH of the each of the nanofluids is measured using pH test strips (Indigo Istruments/3381) with a pH range of 1 to 14. First, the pH values of known substances are measured to verify the pH chart. To take the pH reading, the strip is dipped into the fluid for 2 seconds and read immediately to prevent errors in the reading as the strips dry and the color fades. The pH values are read with an accuracy of ± 0.5. The measured values are shown below in Table 3.1. The pH quoted by the nanofluid manufacturer is 4; however the measured pH for each of the nanofluid concentrations is 5.5. This may be due to exposure to air after the initial manufacturing of the fluid.

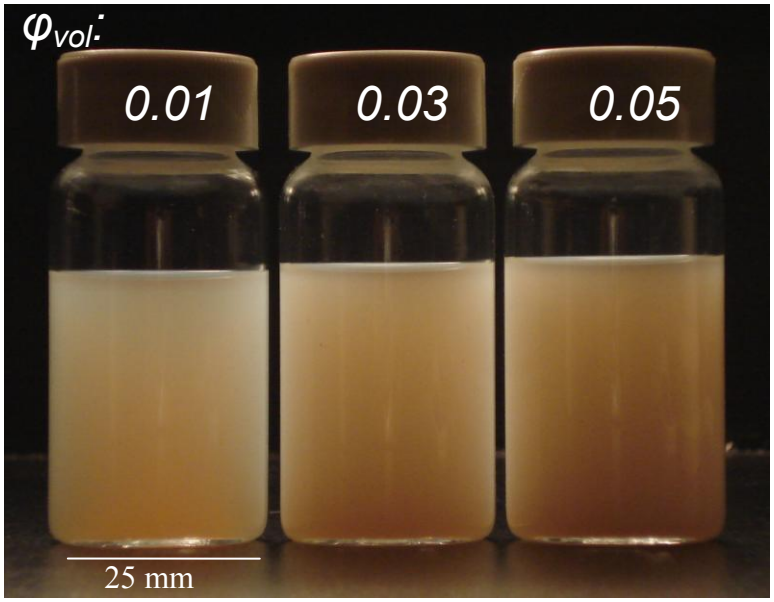

Figure 3.1: Image of nanofluid of alumina particles suspended dispersed in deionized water (Alfa Aesar / 12733) diluted to the desired volumetric concentrations of 1%, 3% and 5% qualitatively showing level of transparency (vials illuminated from behind with a halogen lamp).

Table 3.1: Measured pH values for various fluids.

DI Water	**Tap Water**	**$1\%_{vol}$**	**$3\%_{vol}$**	**$5\%_{vol}$**
6	8	5.5	5.5	5.5

3.3 Dynamic Light Scattering

3.3.1 Theory

Dynamic Light Scattering is a technique used to determine particle sizes based on the time-correlation of scattered light. As laser light is shines into the suspended particles a portion of the incident light is scattered via Rayleigh scattering towards the stationary detector. As the particles move due to Brownian motion the scattered light intensity in the direction of the detector fluctuates. Constructive and destructive

interference occurs as light scatters from multiple particles. As a result, the detector measures an average intensity that fluctuates over time. The time of these fluctuations to decay back to the average intensity depends on the motion of the particles. Smaller particles with more rapid movement result in faster decaying fluctuations than larger slower moving particles.

To quantify the decay time, an autocorrelation is used to compare the intensity at a particular time, t, with the intensity at a later time, $t + \tau$, yielding the correlation as a function of τ. At small τ, the correlation is high and as τ increases the correlation decays exponentially to the background level. For the simplest case of monodisperse particles the correlation is given by:

$$C(\tau) = A\exp(-2\Gamma\tau) + B \tag{3.1}$$

where A is a constant determined by the experimental design, B is the constant background value, and $\Gamma = Dq^2$ is the decay rate, where D is the diffusion coefficient can be determined for spherical particles from Stoke's drag and is given by:

$$D = \frac{k_b T}{3\pi\mu d_p} \tag{3.2}$$

where k_b is the Boltzmann constant, T is the temperature, μ is the fluid viscosity, and d_p is the diameter of the particles and q is the scattering vector given by:

$$q = \frac{4\pi n}{\lambda}\sin\left(\frac{\theta}{2}\right) \tag{3.3}$$

where n is the index of refraction of the fluid, λ is the wavelength of the laser, and θ is the angle at which the scattered light is measured. To account for polydispersity the correlation equation becomes:

$$g(\tau) = \int G(\Gamma)\exp(-\Gamma\tau)d\Gamma \tag{3.4}$$

where $g(\tau)$ is the measured data and $G(\Gamma)$ is the desired distribution. The solution can be found by a variety of methods including imposing a known distribution such as a lognormal distribution, cumulant analysis, or an inverse Laplace Transform. For bimodal distributions the cumulant and lognormal analysis are not adequate. The method used to determine particle sizes for our measurement is the Non-Negatively constrained Least Squares (NNLS) algorithm and is applied by the instrument software. This allows for multimodal distributions to be measured.

3.3.2 Methodology

Initial particle sizes of the nanofluids are measured through dynamic light scattering. To conduct the dynamic light scattering the 90plus Particle Analyzer from Brookhaven Instruments Corporation is used. This instrument has the ability to measure diffusion coefficients ranging from 10^{-6} to 10^{-9} cm^2/s and particle sizes ranging from 1 nm to 6 μm depending on the base fluid properties. A 15 mW, 659 nm, solid state laser beam is directed through the fluid sample. Light is scattered off the particles within the sample through Rayleigh scattering and the scattered light is measured at a 90° angle from the incident beam using a photo detector. The nanofluid is diluted 5e-4 volume fraction and inserted into a disposable, acrylic square cell with outer dimensions of 12 mm x 12 mm width, 46 mm height, and 0.75 mm wall thickness. The measurement is averaged over three 3 minute cycles and a Multimodal

Size Distribution analysis is used to allow for bimodal particle sizes due to the presence of aggregates.

3.3.3 Results

The results from the DLS are shown in Figure 3.2 for both the intensity and number based multimodal distributions. The intensity based distribution gives results skewed to the large particle sizes that scatter a larger amount of light. The software then calculates the number based distribution based on Rayleigh's approximation that the expected intensity of light scattered is proportional to the diameter to the sixth power.

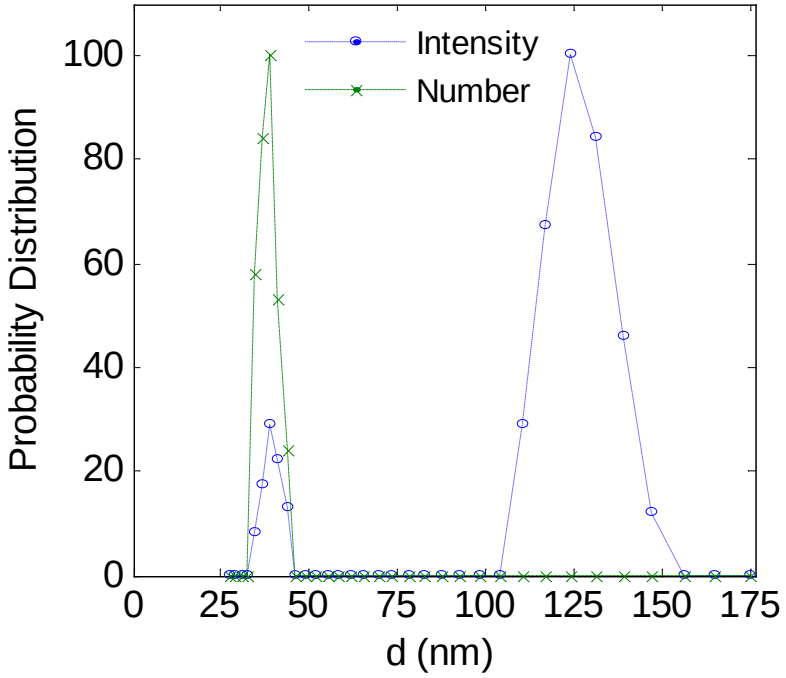

Figure 3.2: Measured multimodal normalized particle size distributions from dynamic light scattering for nanofluid of alumina dispersed in deionized water (Alfa Aesar / 12733) diluted to $0.05\%_{vol}$ concentration presented in both number and intensity based distributions to show presence of permanent aggregates.

The DLS yields a nominal particle diameter of 40.2 nm, a relative variance of 0.02, and skew in the decay of 11.5 nm towards larger diameters. A small number of sintered particles are initially present (less than 5 out of every 1000) with a nominal diameter of 125 nm as shown with the intensity based DLS distribution. These sintered aggregates are large enough to scatter visible light and reduce the transparency of the nanofluid.

3.4 Scanning Electron Microscopy

3.4.1 Theory

Scanning electron microscopes are used to obtain topographical information at length scales smaller than those obtainable by optical microscopes. Scanning electron microscopy utilizes a high energy electron beam incident on the sample producing backscattered electrons and secondary electrons. Backscattered electrons are those reflected or backscattered through elastic scattering and yield information about the composition of the sample. Secondary electrons are the electrons emitted from the sample through inelastic scattering and yield information about the surface topography. By detecting the secondary electrons a topographical image similar to what might be seen through an optical microscope is obtained. The electron beam can be focused very finely allowing for nanometer resolution.

The samples able to be observed using a scanning electron microscope are limited since the surface must be conducting to prevent charging and the sample must be able to withstand a high vacuum environment without evaporating or outgassing.

3.4.2 Methodology

A FEI XL30 Sirion Scanning Electron Microscope (SEM) with FEG source is used to image the particles as they are in suspension to observe individual particle aggregates. Nanofluids must be dried and coated with a conducting surface before imaging. However, when a nanofluid is simply dried onto a substrate, capillary effects due to the surface tension of the receding water pull particles together creating aggregates due to the drying that are not present in the suspension. To view nanofluids in a SEM and keep the particles as they are in suspension, the nanofluids are solidified into a gel: gelified.

Enüstün et al. [77] found gelatin to be an effective coagulation stopping agent to allow viewing of particles at various stages of coagulation. Fernández-Morán et al. [78] used gelatin for embedding small, fragile samples for viewing in an electron microscope. To create the gelified nanofluid, the nanofluid is sonicated, heated to 40°C and mixed at a 1:2 volume ratio with a 40 ^{o}C 15% by weight gelatin – deionized H_2O solution. A thin layer of the mixture is poured into a clean dish and placed in a refrigerator for 30 minutes to allow the mixture to gel and is then transferred into a vacuum chamber to solidify for 6 hours to remove any excess liquid from the nanofluid film and prevent outgassing in the SEM. A 1 cm square section is cut from the film and attached to a pin stub specimen mount (Ted Pella/16111). The sample is sputtered with a thin layer of gold to create a conducting surface.

3.4.3 Results

An SEM image of the gelified nanofluid of 40 nm alumina particles in water is shown in Figure 3.3. The image shows multiple singlet particles and a few sintered aggregates. This location on the gel was chosen to show the sintered aggregates and is not a representation of the relative number of sintered aggregates to singlet particles. To estimate the fractal dimension of the sintered aggregates from the SEM image, the

image is converted to binary changing the pixels within the particles to white and the pixels outside the particle to black as shown in Figure 3.4.

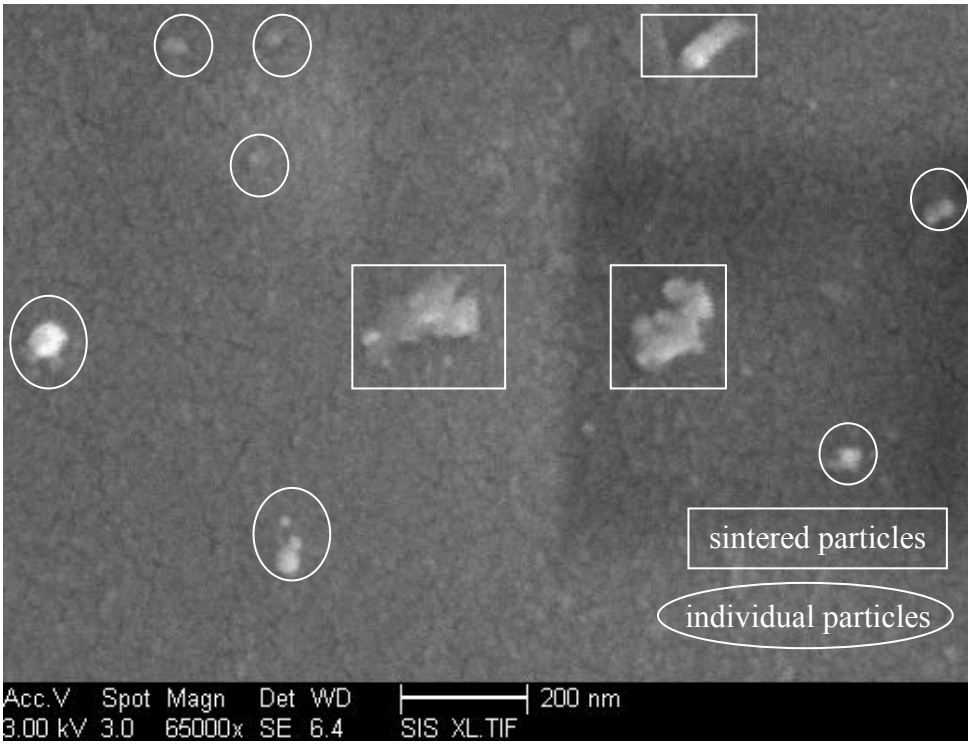

Figure 3.3: SEM image of suspended alumina nanoparticles from the gelified (see Section 3.4.2) water based nanofluid (Alfa Aesar / 12733) showing the presence of singlet particles and permanent aggregates of particles sintered together.

A circle is drawn around the particle to just include the whole aggregate and all the pixels outside the circle are not counted. The concentration of particles in the aggregate, $\varphi_{p,agg}$, is estimated as the ratio of the number of white pixels to total pixels in the circle and is found to be 0.51. We estimate the fractal dimension, d_f, from the following equation:

$$\varphi_{p,agg} = \left(\frac{2R_a}{d_p} \right)^{d_f - 3} \tag{3.5}$$

and find using an aggregate radius of gyration, R_a, of 100 nm and particle diameter, d_p, of 40 nm the value of the fractal dimension for the initial permanent aggregates to be 2.5 ± 0.1. This value is consistent with reaction limited aggregation, showing that the aggregates likely formed during the manufacturing of the nanoparticles.

Figure 3.4: Binary version of aggregate from SEM image. The particle volume fraction in the aggregate is estimated from this image to be 0.51.

3.5 Static Light Scattering

3.5.1 Measurement Theory

Static light scattering allows for the measurement of aggregate characteristics such as radius of gyration, fractal dimension, and primary particle size.[79-82] The magnitude of the scattering vector, q, of light scattered from a small particle is the difference between the incident wave vector, $\vec{k}_i$, and scattered wave vector, $\vec{k}_s$. Rayleigh scattering gives $\left|\vec{k}_i\right| = \left|\vec{k}_s\right| = 2\pi/\lambda$. For light scattered at angle, θ, the scattering vector is then given by [83]:

$$q = \frac{4\pi n}{\lambda}\sin\left(\frac{\theta}{2}\right) \tag{3.6}$$

where n is the index of refraction of the base fluid and λ is the incident laser beam wavelength. The value $1/q$ represents the length scale sampled by the scattered light.

The intensity of the scattered light from an aggregate, $I(q) \propto P(q)S(q)$, where $P(q)$ is the form factor, which represents the intensity of scattered light from a single particle and $S(q)$ is the interparticle structure factor, which represents the added intensity from the light scattered between the particles in the aggregate and describes the structure of the aggregate. When $1/q < R_a$ the scattered light is considered in phase and when $1/q > R_a$ it is not. Variations in $I(q)$ are due mainly to $P(q)$ at large q and $S(q)$ at small q. For $R_a > 1/q > r_p$, $S(q)$ dominates the variation in $I(q)$ with respect to q. $S(q)$ varies as $n_q(N_q)^2$, where $N_q = c_i\left(qr_p\right)^{-d_f}$ is the number of scatterers in a particular q-region and $n_q = c_s\left(R_q q\right)^{d_f}$ is the number of q-regions. This yields variations in intensity given by:[84]

$$I(q) \propto \begin{cases} q^{-4} & 1/q < r_p \\ q^{-d_f} & R_a > 1/q > r_p \\ \left(R_a / r_p\right)^{d_f} & R_a < 1/q \end{cases} \tag{3.7}$$

3.5.2 Measurement Setup

A schematic of the static light scattering setup is shown in Figure 3.5 and an image of the system is shown in Figure 3.6. The fluid is held in glass bottle at the specified temperature. At the time of measurement the nanofluid is pulled into a stationary quartz spectrophotometer flow-through cell (Starna/48-Q-0.5) using a syringe pump (Harvard Apparatus/HA11W) in reverse mode. A collimated 1 mW laser beam of either wavelength 635 nm (Edmund Optics/NT59-080) or 785 nm (Edmund Optics/NT59-082) passes through the cell allowing the light to scatter off the aggregates. The scattered light intensity is measured by a 2.5 mm Si photo-detector (Edmund Optics/NT57-624) detecting wavelengths from 200 to 1000 nm. The photo-detector is rotated around the fluid cell with a motorized rotation stage (Newport/PR50PP) to measure the intensity versus angle. The refraction from the water/quartz/air interfaces are accounted for in the angle used to determine the scattering vector. With the 785 nm laser source we sample the length scale of 150 nm to 180 nm and with the 633 nm laser source we sample the length scale from 115 nm to 140 nm.

The measurement is verified in three ways. First, the variation is confirmed to be symmetric as the photodetector is rotated in both the positive and negative direction. Second, the correct measurement of larger solid amorphous silica NIST traceable size standards particles (Thermo Scientific/ 8050) in the $1/q < r_p$ regime is confirmed. Third, the measurements of the NIST traceable size standards and permanent aggregates are made with two lasers (633 nm and 785 nm) of different wavelength to ensure the same values are measured. The intensity versus scattering vector data for the NIST traceable size standard particles are plotted in Figure 3.7. The fractal

dimension is found to be repeatable to 2% of the average value. Prior to the measurements the nanofluid is sonicated for *4 h*. To prevent variations in the lapse in time between sonication and the measurement the fluid is heated to the desired temperature during sonication. An estimated 15 minutes elapses between sonication and measurement for each case as the fluid is loaded into the light scattering set-up and flow effects are allowed to subside.

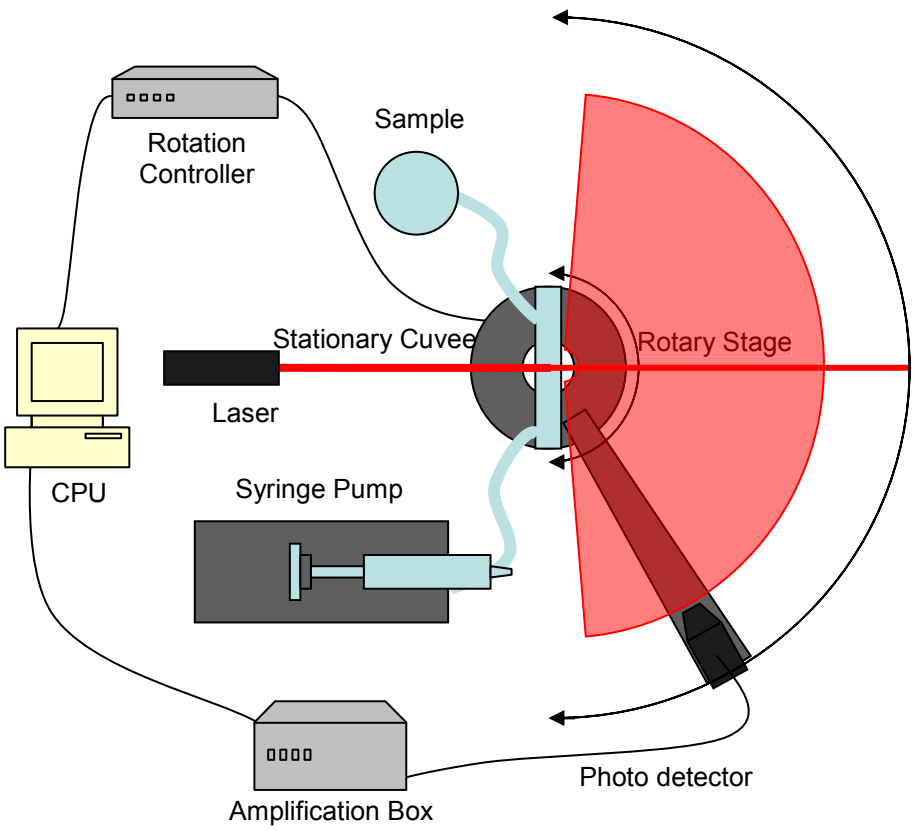

Figure 3.5: Schematic of static light scattering experimental setup showing nanofluid held in bottle at the specified temperature and at the measurement time is pulled into a stationary cuvee with a syringe pump. A laser is shone through the sample causing light to scatter. The scattered light intensity is measured versus angle using a photo detector attached to a rotary stage.

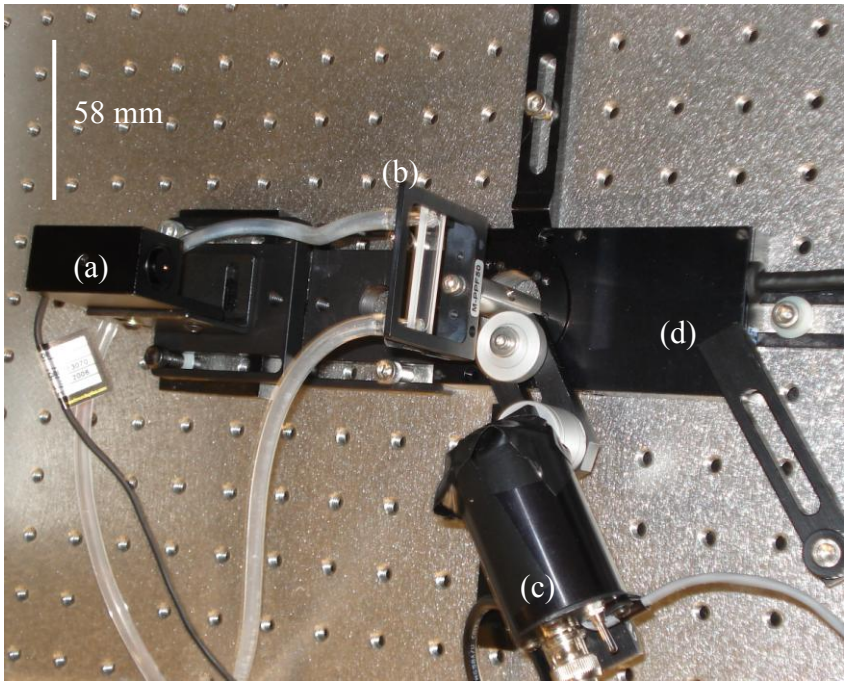

Figure 3.6: Image of static light scattering setup including: (a) laser, (b) flow-through cell, (c) photodetector, and (d) motorized rotational stage.

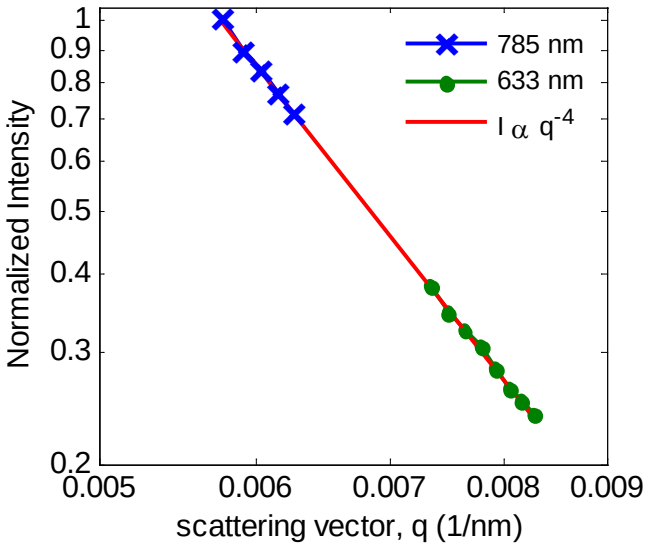

Figure 3.7: Log-log plot of the measured normalized intensity versus scattering vector for the NIST traceable size standards showing the -4 power law for $1/q < r_p$ (red line). Amorphous silica particles, 0.5 µm in diameter dispersed in water are measured with the 785 nm laser (blue x's) and with the 633 nm laser (green dots).

3.5.3 Results

The normalized intensity versus scattering vector is plotted for the various cases with a power law for the fitted fractal dimension. Figures 3.8 and 3.9 show the results for the $1\%_{vol}$ fraction at 20 ^{o}C and 60 ^{o}C, respectively, after 1 hour and show a fractal dimension of 2.4 in both cases at both length scales. The high fractal dimension represents that of the permanent aggregates and is similar to the value determined by the SEM images. Thus, very little aggregation has occurred.

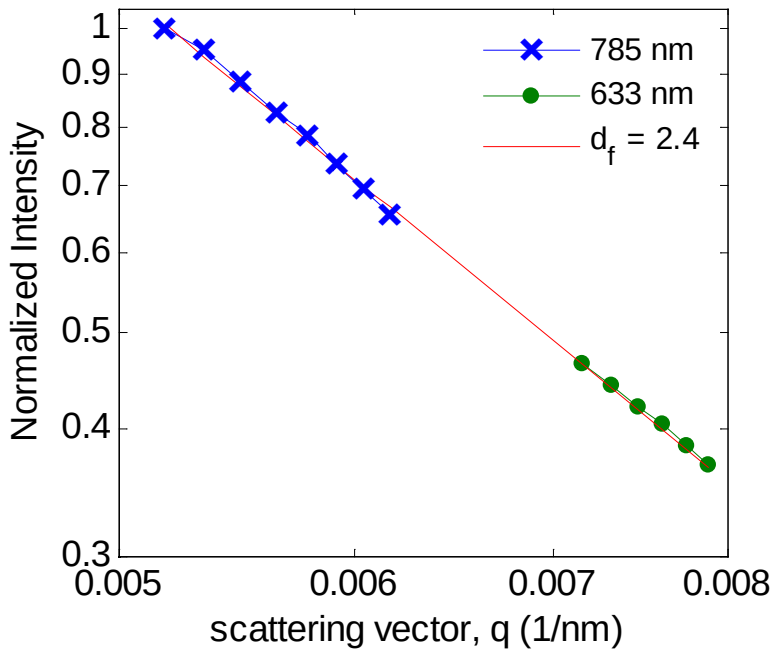

Figure 3.8: Log-log plot of the measured normalized measured intensity versus scattering vector for the $1\%_{vol}$ concentration of alumina dispersed in deionized water (Alfa Aesar / 12733) at 20 ^{o}C with the 785 nm (blue x's) and 633 nm (green dots) lasers after an hour with a fit for the power law with a fractal dimension of 2.4 (red line).

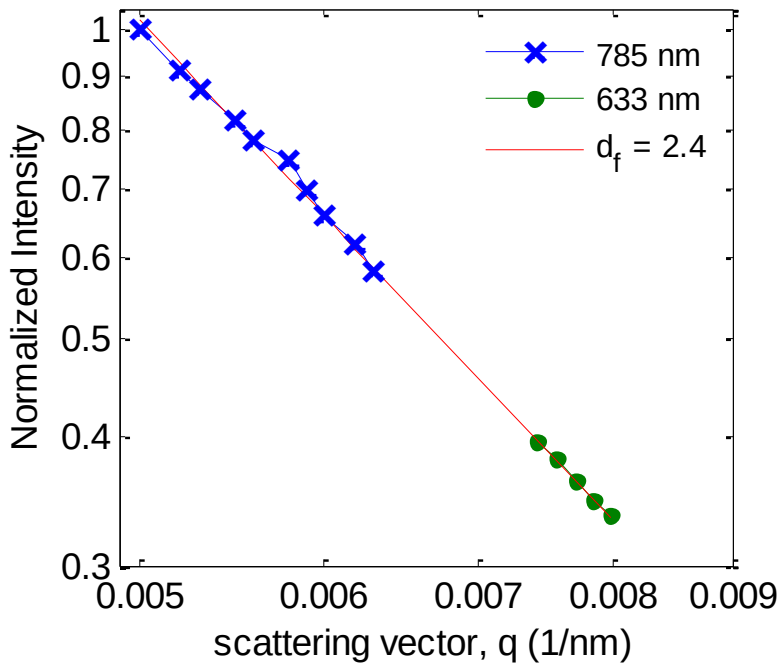

Figure 3.9: Log-log plot of the measured normalized measured intensity versus scattering vector for the 1%$_{vol}$ concentration of alumina dispersed in deionized water (Alfa Aesar / 12733) at 60 ^{o}C with the 785 nm (blue x's) and 633 nm (green dots) lasers after an hour with a fit for the power law with a fractal dimension of 2.4 (red line).

Figure 3.10 shows the results for 3%$_{vol}$ fraction at 20 ^{o}C after 1 hour and shows a fractal dimension of 2.4 for both length scales. This again shows very little aggregation has occurred at this temperature. Figure 3.11 shows the results at 40 ^{o}C, after sonication. The measured average fractal dimension is 2.4 at the shorter length scales and 2.0 at the large length scale where less permanent aggregates are present showing evidence of aggregate formations. At the longer length scales the aggregate formations begin to dominate. The results for one hour of aggregation are shown in Figure 3.12. The measured average fractal dimension stays 2.4 at the smaller length scale and reduces even further to 1.9 for the larger length scale showing further aggregation progression.

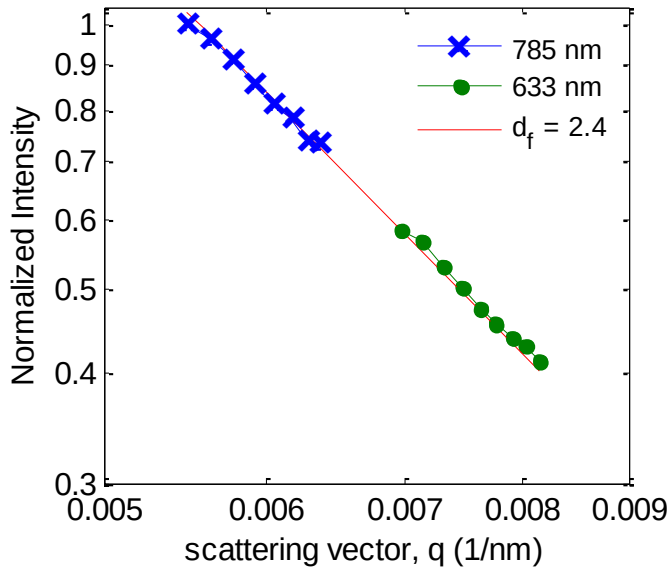

Figure 3.10: Log-log plot of the measured normalized measured intensity versus scattering vector for the $3\%_{vol}$ concentration of alumina dispersed in deionized water (Alfa Aesar / 12733) at 20 ^{o}C with the 785 nm (blue x's) and 633 nm (green dots) lasers after an hour with a fit for the power law with a fractal dimension of 2.4 (red line).

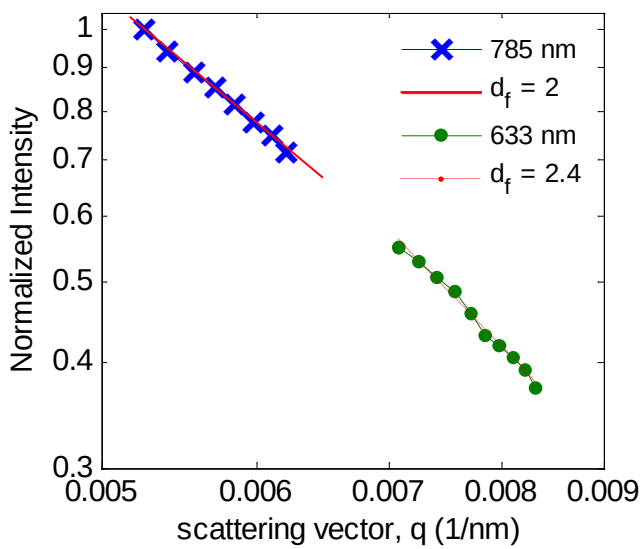

Figure 3.11: Log-log plot of the measured normalized measured intensity versus scattering vector for the $3\%_{vol}$ concentration of alumina dispersed in deionized water (Alfa Aesar / 12733) at 40 ^{o}C with the 785 nm (blue x's) and 633 nm (green dots) lasers after sonication with a fit for the power law with a fractal dimension of 2.0 (red line) and 2.4 (dotted red line).

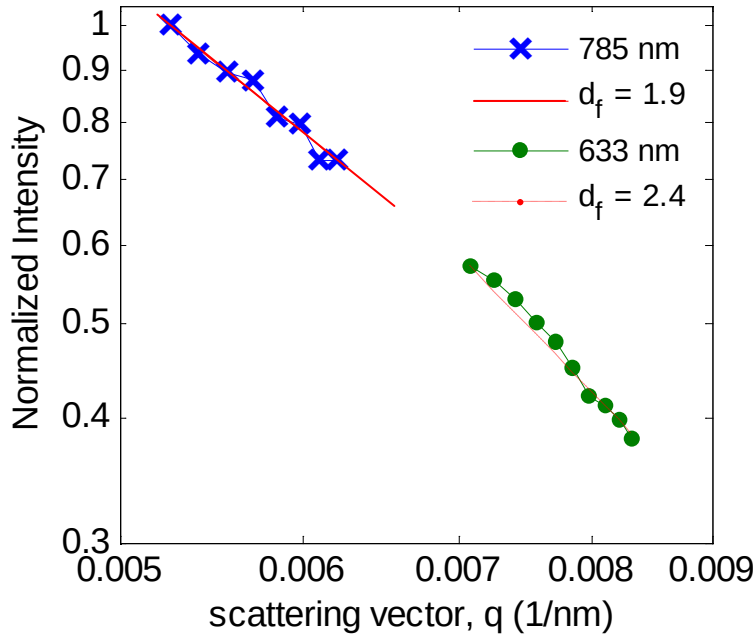

Figure 3.12: Log-log plot of the measured normalized measured intensity versus scattering vector for the 3%$_{vol}$ concentration of alumina dispersed in deionized water (Alfa Aesar / 12733) at 40 ^{o}C with the 785 nm (blue x's) and 633 nm (green dots) lasers after an hour with a fit for the power law with a fractal dimension of 1.9 (red line) and 2.4 (dotted red line).

The 60 ^{o}C case after sonication is plotted in Figure 3.13. In this case, the fluid starts out similar to the 40 ^{o}C case with a measured average fractal dimension of 2.4 for the smaller length scale and 2.1 for the larger length scale. The results after an hour are plotted in Figure 3.14. For the smaller length scale the measured average fractal dimension has reduced to 2.3 while the larger length scale has reduced to 1.8. This is evidence of the aggregate formations becoming numerous enough to reduce the average fractal dimension measured at the smaller length scale and of great enough size to have a substantial impact at the larger length scales.

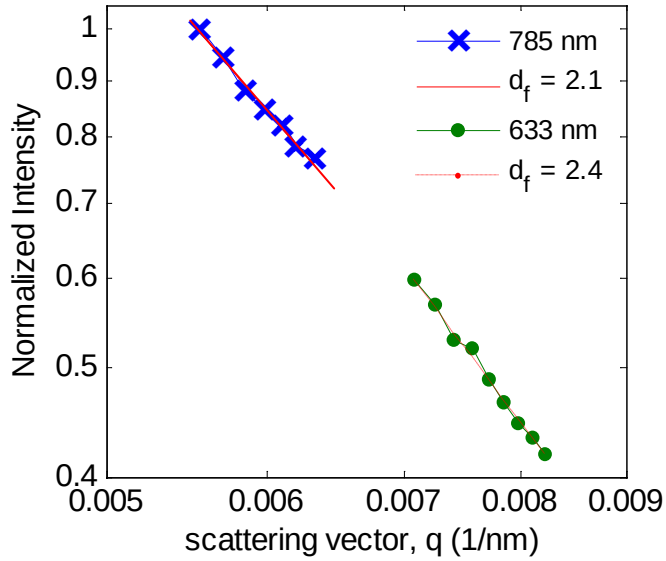

Figure 3.13: Log-log plot of the measured normalized measured intensity versus scattering vector for the $3\%_{vol}$ concentration of alumina dispersed in deionized water (Alfa Aesar / 12733) at 60 ^{o}C with the 785 nm (blue x's) and 633 nm (green dots) lasers after sonication with a fit for the power law with a fractal dimension of 2.1 (red line) and 2.4 (dotted red line).

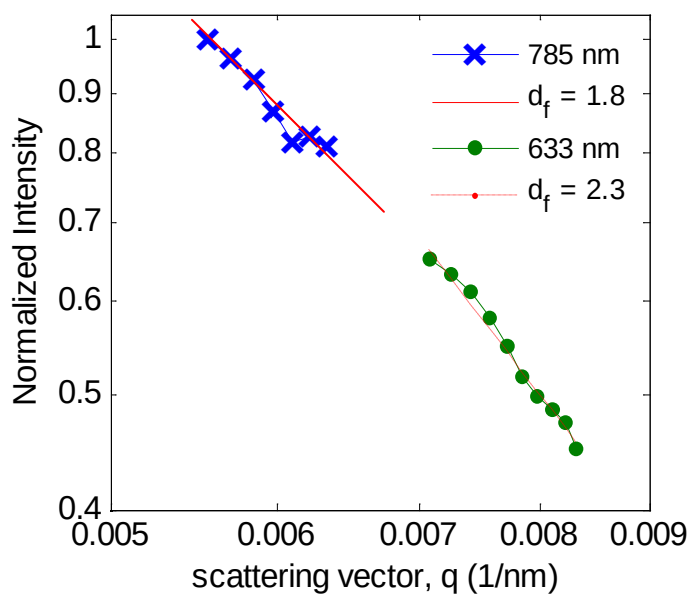

Figure 3.14: Log-log plot of the measured normalized measured intensity versus scattering vector for the $3\%_{vol}$ concentration of alumina dispersed in deionized water (Alfa Aesar / 12733) at 60 ^{o}C with the 785 nm (blue x's) and 633 nm (green dots) lasers after an hour with a fit for the power law with a fractal dimension of 1.8 (red line) and 2.3 (dotted red line).

The 20 ^{o}C case for the 5%$_{vol}$ fraction after an hour is plotted in Figure 3.15. As with both the 1% and 3%$_{vol}$ fractions, the measured average fractal dimension for both length scales is 2.4 indicating very little aggregation. Figure 3.16 shows the results for 40 ^{o}C after sonication. For the smaller length scale the measured average fractal dimension is 2.4. For the larger length scale the fractal dimension has reduced to 1.8. This shows the presence of a small number of large aggregate formations. The results for an hour later plotted in Figure 3.17 give a fractal dimension of 2.3 at the smaller length scales showing that the number of aggregate formations is increasing. At the larger length scales the fractal dimension is again 1.8. The results for the 60 ^{o}C case after sonication are shown in Figure 3.18. The fractal dimension for the shorter and longer length scales are 2.2 and 1.8, respectively, showing a significant number of aggregate formations already present. The results for an hour later are shown in Figure 3.19. The fractal dimensions for the shorter and longer length scales are 2.0 and 1.8 respectively showing an increasing number of aggregate formations over time.

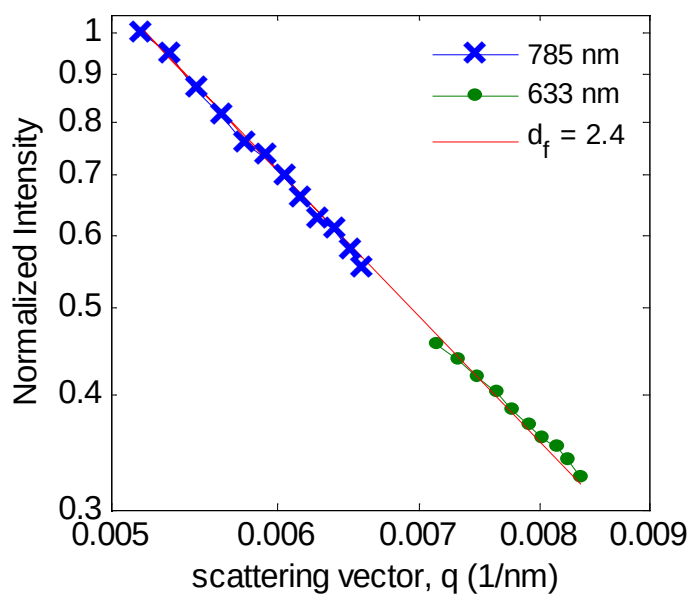

Figure 3.15: Log-log plot of the measured normalized measured intensity versus scattering vector for the 5%$_{vol}$ concentration of alumina dispersed in deionized water (Alfa Aesar / 12733) at 20 ^{o}C with the 785 nm (blue x's) and 633 nm (green dots) lasers after an hour with a fit for the power law with a fractal dimension of 2.4 (red line).

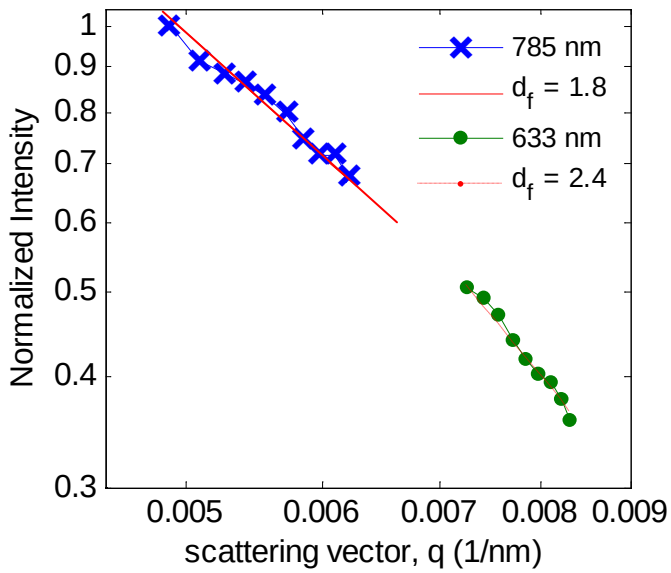

Figure 3.16: Log-log plot of the measured normalized measured intensity versus scattering vector for the $5\%_{vol}$ concentration of alumina dispersed in deionized water (Alfa Aesar / 12733) at 40 ^{o}C with the 785 nm (blue x's) and 633 nm (green dots) lasers after sonication with a fit for the power law with a fractal dimension of 1.8 (red line) and 2.4 (dotted red line).

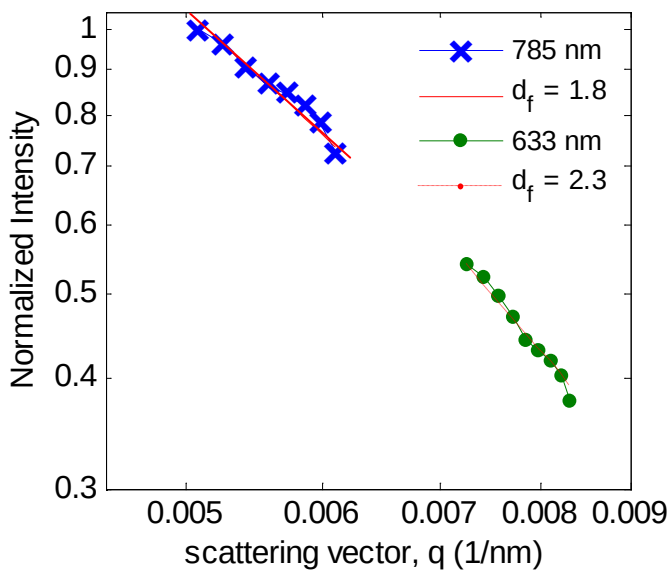

Figure 3.17: Log-log plot of the measured normalized measured intensity versus scattering vector for the $5\%_{vol}$ concentration of alumina dispersed in deionized water (Alfa Aesar / 12733) at 40 ^{o}C with the 785 nm (blue x's) and 633 nm (green dots) lasers after an hour with a fit for the power law with a fractal dimension of 1.8 (red line) and 2.3 (dotted red line).

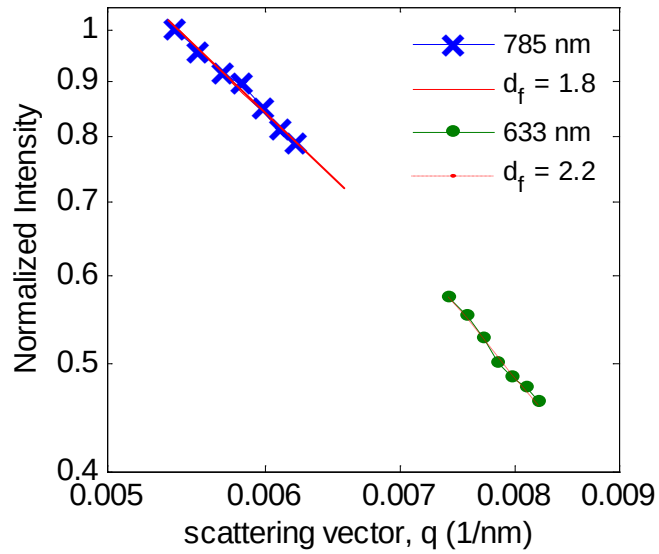

Figure 3.18: Log-log plot of the measured normalized measured intensity versus scattering vector for the 5%$_{vol}$ concentration of alumina dispersed in deionized water (Alfa Aesar / 12733) at 60 ^{o}C with the 785 nm (blue x's) and 633 nm (green dots) lasers after sonication with a fit for the power law with a fractal dimension of 1.8 (red line) and 2.2 (dotted red line).

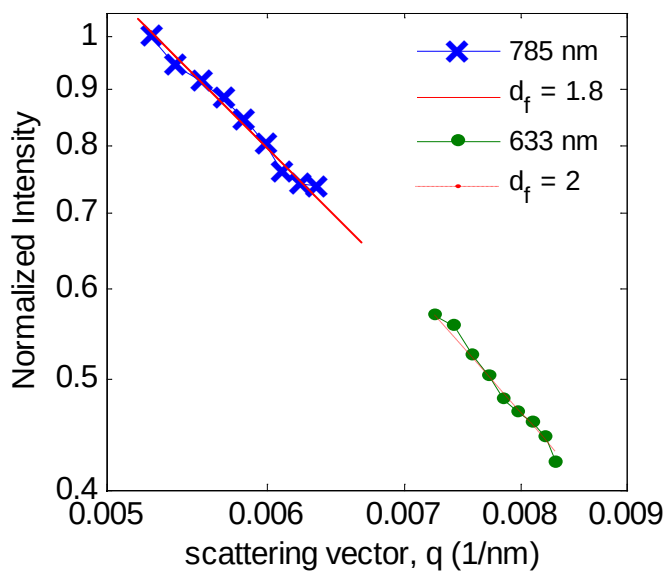

Figure 3.19: Log-log plot of the measured normalized measured intensity versus scattering vector for the 5%$_{vol}$ concentration of alumina dispersed in deionized water (Alfa Aesar / 12733) at 60 ^{o}C with the 785 nm (blue x's) and 633 nm (green dots) lasers after an hour with a fit for the power law with a fractal dimension of 1.8 (red line) and 2 (dotted red line).

The measured fractal dimensions for each temperature over time for the 1%, 3%, and 5%$_{vol}$ concentrations are plotted in Figures 3.20, 3.21, and 3.22, respectively at 20 ^{o}C, 40 ^{o}C, and 60 ^{o}C. The 1%$_{vol}$ concentration shows a fractal dimension of 2.4 at all times and temperatures due to a lack of significant aggregation. The 3%$_{vol}$ concentration shows a fractal dimension of 2.4 for 20 ^{o}C at both times and wavelengths. At 40 ^{o}C at the smaller length-scales below 135 nm, the fractal dimension is 2.4 and at larger length-scales the average fractal dimension becomes 2.0 at early times and reduces to 1.9 after an hour. At 60°C at the smaller length-scales, the average fractal dimension begins at 2.4 and reduces to 2.3 after an hour. At the larger length-scales, the average fractal dimension begins at 2.1 and reduces to 1.8 after an hour. The 5%$_{vol}$ concentration again shows a fractal dimension of 2.4 for 20°C at both times and length-scales and for 40 ^{o}C at the smaller length-scales initially and then reduces to 2.3 after an hour. At 60 ^{o}C at the smaller length-scales the average fractal dimension begins at 2.2 and reduces to 2.0 after an hour. At the larger length-scales the average fractal the average fractal dimension becomes 1.8 at both 40 ^{o}C and 60 ^{o}C at both times.

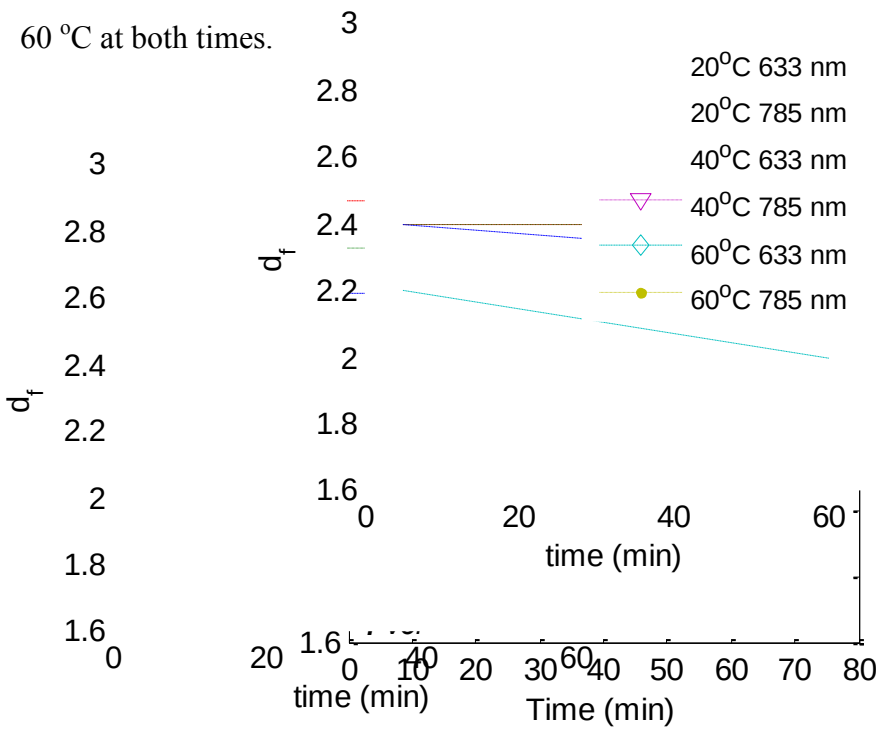

Figure 3.20: Plot of the measured fractal dimension versus time for the 1%$_{vol}$ concentration of 40 nm alumina nanoparticles dispersed in deionized water (Alfa Aesar / 12733) at 20, 40 and 60 ^{o}C.

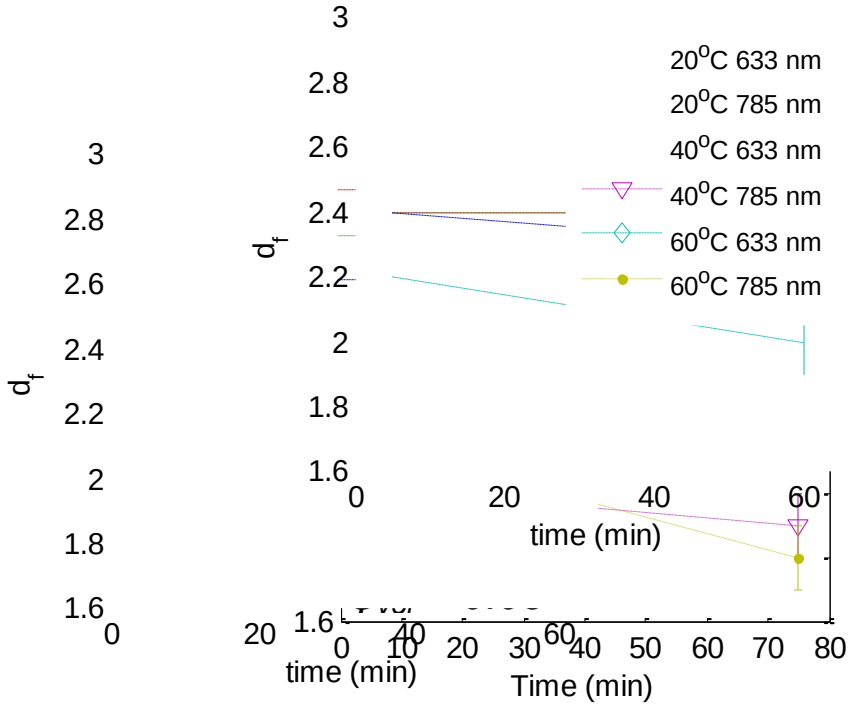

Figure 3.21: Plot of the measured fractal dimension versus time for the 3%$_{vol}$ concentration of 40 nm alumina nanoparticles dispersed in deionized water (Alfa Aesar / 12733) at 20, 40, and 60 °C.

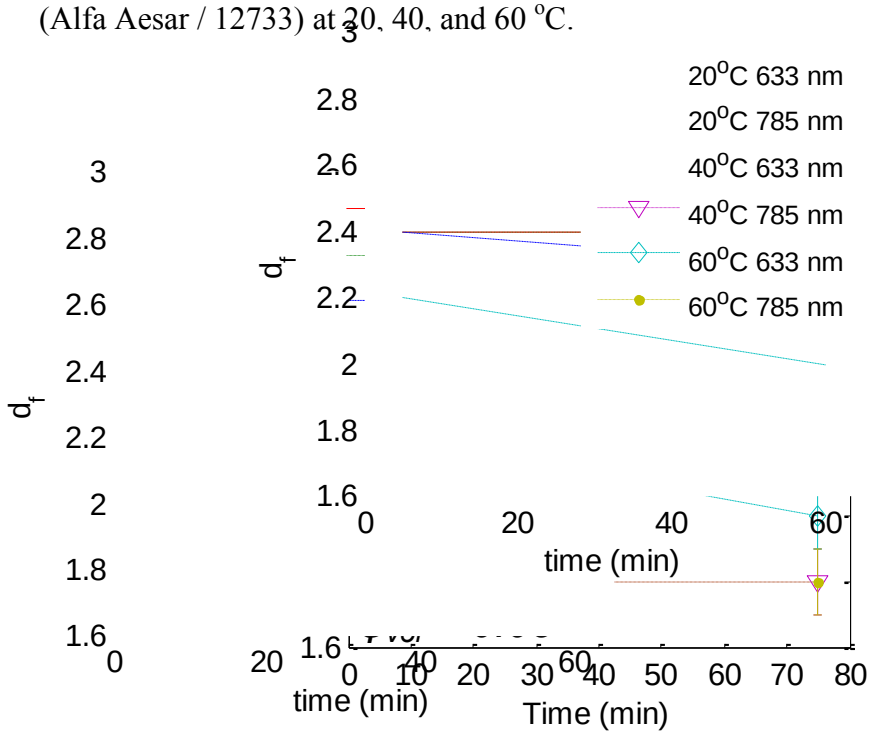

Figure 3.22: Plot of the measured fractal dimension versus time for the 5%$_{vol}$ concentration of 40 nm alumina nanoparticles dispersed in deionized water (Alfa Aesar / 12733) at 20, 40, and 60 °C.

3.6 Conclusion

At room temperature this fluid is well stabilized and few aggregate formations are present over time. When the nanofluid is heated the nanoparticles experience stronger Brownian motion, which increases as the fluid is heated further. This allows for greater aggregation at higher temperatures. At higher concentrations, more particles are present allowing particles to interact more, increasing the amount of aggregation. The diffusion limited aggregates produce fractal dimensions of 1.8, which is especially apparent in the higher concentrations and temperatures in the length scale larger than the permanent aggregates.

These results show that aggregation is a likely cause for the increasing enhancements of thermal conductivity with temperature reported by previous research groups. At higher temperatures, aggregation occurs quickly enough to effect measurements within minutes of sonication. If the fluid is not heated during sonication and must be heated between sonication and the measurement the aggregation would progress further for the higher temperatures with more time lapse.

PAGE INTENTIONALLY LEFT BLANK

Chapter 4

Simulation of Aggregation and Thermal Diffusion

4.1 Introduction

The importance of aggregation and thermal diffusion on nanofluids for heat transfer was discussed in Chapters 1 and 2. The thermal conductivity measurements of Chapter 2 showed the effects of the combination of aggregation and thermal diffusion. It is necessary to develop a full scale model of the two effects on the particles to be able to separate and fully understand their interplay.

This chapter describes two simulations to study the aggregation and thermal diffusion separately and combined. The Onsager relation for particle and heat flux is solved to determine and expected concentration profile from the thermal diffusion. A Brownian motion base Monte Carlo simulation of the nanofluids is conducted in three ways: first simulating only thermal diffusion in a temperature gradient, second simulating only aggregation under isothermal conditions, and finally combining aggregation and thermal diffusion. A comparison between the numerical simulation and the Monte Carlo results of thermal diffusion without aggregation yields an estimate of the Soret coefficient. It is found that the concentration distribution created

from the thermal diffusion greatly affects the thermal conductivity profile. The results from the full Monte Carlo simulation are found to agree well with the experimental results.

4.2 Onsager Solution for Thermal Diffusion

4.2.1 Methodology

A numerical simulation models the thermal diffusion for non-interacting particles in the experimental setup. The concentration and temperature profile over time is modeled through a numerical simulation of the appropriate Onsager relation [85,86] for the particle and heat flux given below:

$$j = -D\nabla c - D_T c \nabla T \tag{4.1}$$

$$q = -c_1 \nabla T - c_2 \nabla c \tag{4.2}$$

where j is the particle flux, D is the diffusion coefficient, c is the concentration, T is the temperature, c is the particle number concentration, D_T is the thermal diffusivity, q is the heat flux, and c_1 and c_2 are unknown coefficients.

In steady-state conditions, the particle flux goes to zero and equation 4.1 reduces to the Soret equation:

$$0 = -\nabla c - S_T c \nabla T \tag{4.3}$$

where $S_T = D_T/D$ is the Soret coefficient. The second term in equation 4.1 represents the Soret effect, which is the mass flux due to a temperature gradient. The second

term in equation 4.2 represents the Dufour effect [85], which is the heat flux due to a concentration gradient. This effect is typically very small.

To isolate the Dufour effect, equations 4.1 and 4.2 are combined to cancel the concentration gradient, the following equation is formulated:

$$q = \frac{c_2}{D} j - (c_1 - c_2 c S_T)\nabla T \tag{4.4}$$

leaving the first term as the portion of the heat flux that is due the particle flux and the second term as the typical Fourier's Law for heat diffusion with $(c_1 - c_2 c S_T)$ equivalent to the thermal conductivity.

From equation 4.1, the maximum particle flux from a constant volume fraction profile is calculated. The apparent increase in thermal conductivity from the particle diffusion by applying Fourier's Law and the equation:

$$q'' = \frac{\dot{m}}{A} c_p \Delta T = -k_{added} \frac{dT}{dx} \tag{4.5}$$

By estimating the mass flux, $\dot{m}$, over area, A, as the particle flux times the particle mass, the contribution to the thermal conductivity from the maximum particle flux is on the order of 10^{-7} W/m-K, which is small compared to the base fluid thermal conductivity. This shows $c_2 \nabla c$ is multiple orders of magnitude smaller than $c_1 \nabla T$ and is negligible. Thus, c_1 is the thermal conductivity k_{eff} and equation 4.2 reduces to Fourier's Law: $q'' = -c_1 \nabla T = -k_{eff} \nabla T$. The mass flux from thermal diffusion does not cause a measurable increase in heat flux or an apparent increase in thermal conductivity. This is consistent with the findings of other research groups.[58]

The Soret coefficient can be estimated from the ratio of the thermal diffusivity and the diffusion coefficient. The thermal diffusivity due to electrostatic effects is given by [87]:

$$D_T = \frac{-1}{4\mu_f T}\left(\varepsilon + T\frac{\partial \varepsilon}{\partial T}\right)\zeta^2 \tag{4.6}$$

where μ_f is the fluid viscosity, ε is the relative permeability of the fluid, and ζ is the zeta potential of the particle. The diffusion coefficient is modeled using Stoke's drag for a spherical particle and is given by:

$$D = \frac{k_b T}{3\pi \mu_f d_p} \tag{4.7}$$

where k_b is the Boltzmann constant and d_p is the particle diameter. The typical zeta potential of alumina in water ranges between 25 and 55 mV [88]. This yields of range of potential S_T values from 0.01 to 0.05 K^{-1} for a temperature of 300 K.

The coupled differential equations for the particle and heat flux are discritized with the control volume technique. A temperature profile only dependent on the thermal conductivity distribution is assumed. The temperature dependence of the viscosity is accounted for in the diffusion coefficient. The temperature is calculated at each time step using the effective thermal conductivity of each element and the second Onsager equation, which reduces to Fourier's law $dT/dx = -q/k_{eff}$. The effective thermal conductivity is calculated using Maxell's effective medium theory taking into account the variation in concentration across the temperature field due to the thermal diffusion.

To solve for the time evolution of the concentration distribution, the divergence of the first Onsager equation is taken yielding:

$$\frac{\partial c}{\partial t} = -\nabla \cdot j = \nabla \cdot (D\nabla c) + \nabla \cdot (DS_T c \nabla T) \tag{4.8}$$

$$\frac{\partial \varphi}{\partial t} = \nabla \cdot (D\nabla \varphi) + \nabla \cdot (DS_T \varphi \nabla T) \tag{4.9}$$

The change in the concentration for each element at a particular time step is calculated from the fluid properties and the local concentration and temperature gradients. At the boundaries the particle flux is set to zero yielding the conditions:

$$\nabla \varphi = -S_T \varphi \nabla T\big|_{0,h} \rightarrow \frac{\varphi_{1,n} - \varphi_{0,n-1}}{dx} = S_T \varphi_{0,n} \frac{q''}{k_{eff,0,n}} \tag{4.10}$$

$$\varphi_0 = \frac{\varphi_1}{1 - dxS_T q''/k_{eff,0}} \tag{4.11}$$

$$\varphi_n = \frac{\varphi_{n-1}}{1 + dxS_T q''/k_{eff,n}} \tag{4.12}$$

where n is the number of elements, h is the width of the channel, and dx is the width of an element.

4.2.2 Results

The numerical model is run for 40 nm particle diameter at each concentration. The temperature of the cold boundary is held at 20 ^{o}C and a heat flux of 4 W/cm^2 is applied at the opposite boundary as in the experiments. Since exact S_T for our fluid is

unknown the model is run for multiple values in the expected range given previous data for similar samples.[76] The steady state concentration profiles for various S_T and 5%$_{vol}$ concentration are plotted in Figure 4.1. The normalized profile for each concentration is effectively the same. As S_T is increased the variation in concentration across the temperature field is increased.

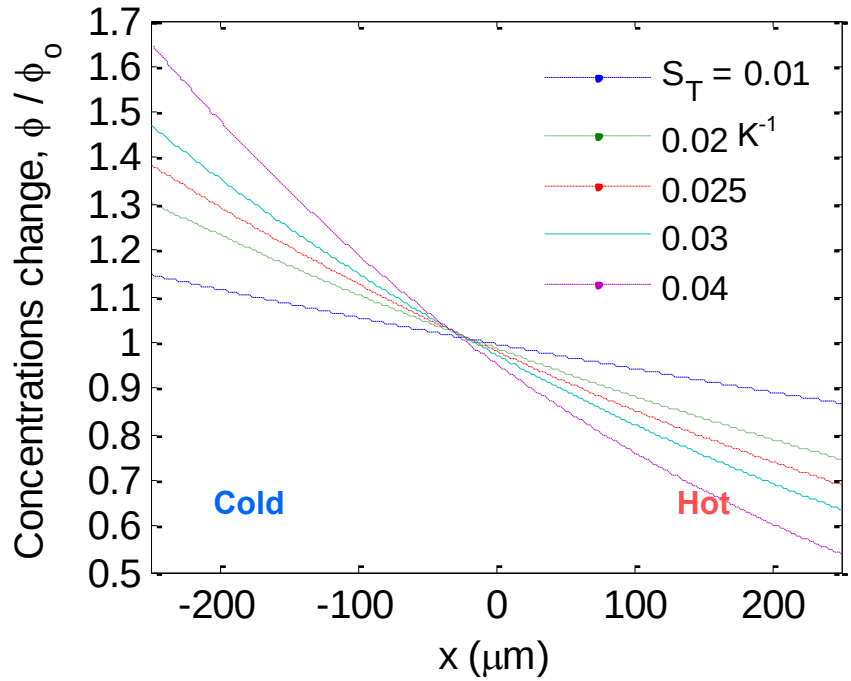

Figure 4.1: Calculated normalized particle concentration distribution, calculated from the numerical solution to the Soret effect in the Onsager relations, at steady state for various S_T values for 40 nm alumina nanoparticles in water subjected to a heat flux of 4 W/cm^2.

To look at the effect particle size has on the thermal diffusion, the simulation was run for three additional diameters, 60 nm, 80 nm, and 130 nm. The normalized concentration distribution for the diffusion for an S_T of the mean value of 0.025, 5%$_{vol}$ concentration, and time of 40 minutes is shown in Figure 4.2. As the particle size is increased, the diffusion coefficient decreases due to their inverse relationship, decreasing the rate of diffusion. The concentration profile for the 130 nm case at 40

minutes is approximately equivalent to the 40 nm case at 10 minutes. This verifies the inverse relationship between the diffusion coefficient and the diffusion time constant.

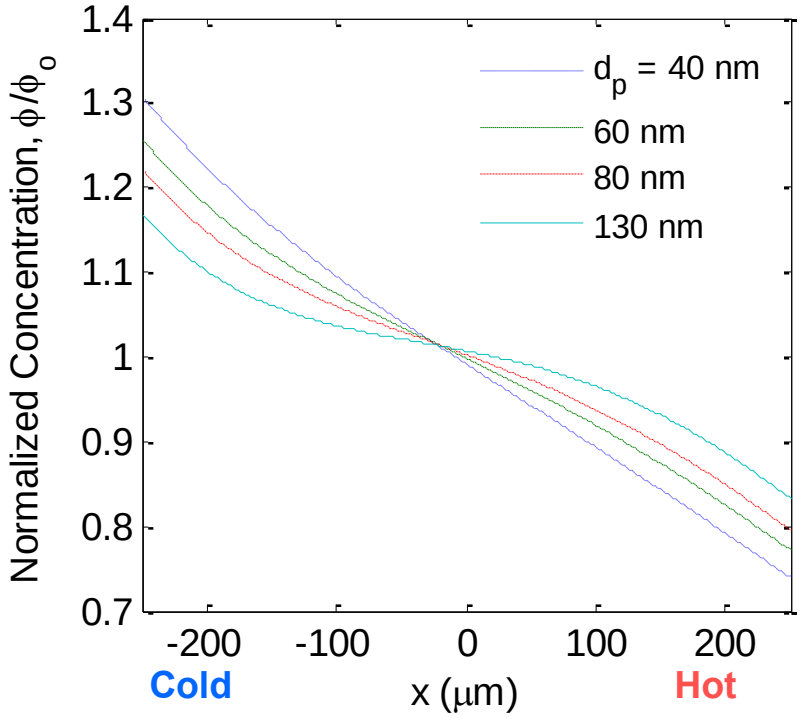

Figure 4.2: Calculated normalized particle concentration distribution, calculated from the numerical solution to the Soret effect in the Onsager relations with S_T of 0.025 K^{-1}, at steady state for various particle diameters for alumina nanoparticles in water subjected to a heat flux of 4 W/cm^2.

4.3 Monte Carlo Simulation

4.3.1 Methodology

Methods of modeling particle aggregation vary depending on the desired output. The Monte Carlo method allows for direct simulation of the system. Two main types of Monte Carlo simulations of aggregation are typically used. The first allows for the simulation of the growth and structure of the aggregates. [89,90] The second allows for extraction of bulk effects due to the aggregation. Spielman and

Levenspiel [91] showed the effectiveness of a Monte Carlo simulation for a system of reacting coalescing droplets by randomly choosing two droplets to coalesce, mix and redistribute at a constant rate. Shah et al. [92] expanded the simulation procedure by modeling the random behavior in terms of probability functions and advancing time based on the expected time for the event to occur. Liffman [93] calculates the probability of one cluster/particles interacting with another. Based on the probability a single particle is randomly chosen to interact and another particle is randomly chosen to interact with it. From the simulation, they modeled the size distribution of the clusters over time. Kruis et al. [94] proposed a simpler version by summing the collision functions for each possible particle pair and choosing pairs to aggregate based on a comparison between a random number and the relative magnitude of a pairs collision function. After each iteration, the time is progressed based on the number of aggregating pairs. For both of these last simulations no regard is given to the position of the particles.

In this study, the method of Kruis et al. is expanded on to determine the aggregate size variation across the temperature gradient and calculate the variation of the properties.[95] Rather than allow aggregation between any particles in the simulated volume, only pairs near each other are considered as potential aggregates. Instead of choosing a time step based on the number of aggregating pairs, the number of aggregating pairs is chosen from the time step. The simulation determines the time evolution of the concentration distribution and aggregate sizes.

4.3.1.1 Particle Initialization and Aggregation

The particles are initially uniformly distributed within the modeled area. At each time step, a normally distributed random displacement is applied to each particle in the x and y directions with mean zero and variance $2D\Delta t$. The simulation accounts for the temperature dependence of the viscosity and diffusion coefficient and applies specular reflection at the boundaries.

The aggregation is modeled through a three step process. The expected number of aggregating collisions in a given time step is calculated from the inverse of the sum of the collision frequency function, β, for all particle pairs by $N_{col} = A/\sum\beta_{ij}$, where A is the simulated area. For Brownian limited aggregation the collision frequency function derived from Fick's Law is given by:[94,96,97]

$$\beta_{ij} = 4\pi\left(D_i + D_j\right)\cdot\left(r_i + r_j\right) \tag{4.13}$$

Pairs of particles separated by less than their average diameter are identified as potentially aggregating collisions. Potentially aggregating collisions are chosen randomly to aggregate up to the expected number of aggregating collisions. The time step is sufficiently small to ensure more potentially aggregating collisions are identified than the number of expected aggregating collisions.

The simulation keeps track of the number of particles in, the average diameter of the particles in, the predicted radius of gyration of, and the hydraulic diameter of the aggregates. The radius of gyration is calculated by equating the particle volume fraction within the aggregate from two formulas, the first based on volume fraction (eq. 4.14), the second from 3D fractal theory of aggregates (eq. 4.15):

$$A_{agg} = \frac{NA_p}{\varphi_{p,agg}} = \pi R_a^2 = \frac{N\pi d_p^2}{2^2\varphi_{p,agg}} \rightarrow \varphi_{p,agg} = \frac{Nd_p^2}{4R_a^2} \tag{4.14}$$

$$\varphi_{p,agg} = \left(\frac{2R_a}{d_p}\right)^{d_f - 3} \tag{4.15}$$

where $\varphi_{p,agg}$ is the particle volume fraction in the aggregate, N is the number of particles in the aggregate, d_p is the average particle size in the aggregate, R_a is the radius of gyration of the aggregate, and d_f is the fractal dimension of the aggregate. We assume the aggregates are sparse enough, given their low fractal dimension, for the two dimensional area concentrations to equal the three dimensional volume concentrations. The fractal dimension is a measure of the change in particle density with distance from the center of the aggregate and typically varies between 1.7 and 2.5 for 3D. It relates the particle volume fraction in the aggregate to the aggregate radius of gyration through the power law given in equation 4.15.

Since the orientation of the aggregate is unknown and the aggregate structure is assumed, a directional variation of the diffusion coefficient is not practical. The aggregate diffusion coefficient is estimated for all directions using the hydraulic diameter of the aggregate given by:

$$d_h = 2\left(\frac{\sum A_{c,p}}{\pi}\right)^{1/2} \tag{4.16}$$

where $A_{c,p}$ is the cross-sectional area of an individual particle in the aggregate.

4.3.1.2 Effective Properties

The effective thermal conductivity of the aggregates is calculated by separating them into two components, the percolation contributing backbone and non-percolation contributing dead-ends.[52] The effective thermal conductivity of the dead-end particles, k_{nc}, is calculated using the Bruggeman model, which is appropriate for high volume fractions of particles [30]:

$$\sum_i \frac{\varphi_i\left(k_i - k_{nc}\right)}{k_i + 2k_{nc}} = 0 \tag{4.17}$$

where φ_i is the volume fraction of the non-percolation contributing aggregate components (fluid and dead-end particles) and k_i is the thermal conductivity of the components. The effective thermal conductivity of the aggregate, k_{agg}, is calculated using composite theory for completely randomly oriented ellipsoidal particles, for the backbone, in a matrix of the non-percolation contributing portion. The following equations are used [33]:

$$k_{agg} = k_{nc} \frac{3+\varphi_c\left(2\beta_{11}^c(1-L_{11})+\beta_{33}^c(1-L_{33})\right)}{3-\varphi_c\left(2\beta_{11}^c L_{11}+\beta_{33}^c L_{33}\right)} \tag{4.18}$$

$$L_{11} = \begin{cases} 0.5p^2/\left(p^2-1\right)-0.5p\cosh^{-1} p/\left(p^2-1\right)^{1.5} & p>0 \\ 1/3 & p=0 \end{cases} \tag{4.19}$$

$$L_{33} = 1-2L_{11} \tag{4.20}$$

$$\beta_{ii}^c = \left(k_{ii}^c - k_{nc}\right)/\left(k_{nc}+L_{ii}\left(k_{ii}^c-k_{nc}\right)\right) \quad i=1,3 \tag{4.21}$$

$$k_{ii}^c = \frac{k_p}{\left(1+\gamma L_{ii}k_p/k_f\right)}, \quad \left(with\ \gamma = \left(2+\frac{1}{p}\right)\alpha, \quad \alpha = \frac{2R_b k_f}{d_p}\right) \tag{4.22}$$

where R_b is the boundary resistance between the particle and the fluid and p is the ratio between the length of the percolating chain to the particle size. The effective thermal conductivity of the nanofluid is found through the Maxwell effective medium theory [98] for dispersed particles and is given by:

$$k_{eff} = k_f \frac{k_{agg}+(n-1)k_f-(n-1)\varphi_{agg}\left(k_f-k_{agg}\right)}{k_{agg}+(n-1)k_f+\varphi_{agg}\left(k_f-k_{agg}\right)} \tag{4.23}$$

where φ_{agg} is the volume fraction of aggregates in the fluid and $n = 3/\psi$ where ψ is the sphericity of the aggregate. A spherical aggregate is assumed yielding $n = 3$.

The volume fraction of the particles in the aggregate is given by equation 4.15 and $\varphi_{p,agg} = \varphi / \varphi_{agg}$ and the volume fraction of the backbone particles in the aggregate is $\varphi_c = \left(2R_a / d_p\right)^{d_l - 3}$, where d_l is the chemical dimension of the aggregates. The chemical dimension is a measure of the branch dimensions within the aggregate and theoretically varies between 1 and d_f though a maximum value of 1.6 is imposed by the self-avoiding random walk.[99] It relates the concentration of backbone particles within the aggregate to the radius of gyration of the aggregate through a power law. The volume fraction of the dead-end particles in the aggregate is $\varphi_{nc} = \varphi_{p,agg} - \varphi_c$. A limit is imposed on the size of the aggregates based on the fractal theory by setting $\varphi_{agg} = 1$ yielding a maximum radius of gyration of $R_{a,\max} = \left(d_p / 2\right)\varphi^{1/\left(d_f - 3\right)}$.

To determine the effect of aggregation and thermal diffusion on the viscosity and the viscosity profile, the bulk effective viscosity of the nanofluid is calculated. The effective hydrodynamic viscosity for fractal aggregates is modeled by:[99]

$$\mu_{eff} = \mu_f \left(1 - \frac{\varphi_{agg}}{\varphi_{\max}}\right)^{-2.5\varphi_{\max}} \tag{4.24}$$

where $\varphi_{max} = 0.61$ is the maximum possible volume concentration for rigid spheres. This equation is most appropriate for higher shear rates, where most nanofluids have been found to have less shear thinning.[100]

The expected enhancements in thermal conductivity and viscosity versus aggregate radius of gyration from these models at various fractal dimensions are plotted in Figures 4.3 and 4.4, respectively. These results assume all aggregates

are the same size and no singlet particles are present, which is unlikely. Both thermal conductivity and viscosity show initially large changes in the enhancement with aggregation radius of gyration. After a certain point that depends on the fractal dimension, the enhancement in thermal conductivity stagnates with changes in aggregate size and even reduces at a fractal dimension of 2.4. However, the viscosity continues to increase with increasing aggregate size.

Figure 4.5 plots the ratio of the viscosity to thermal conductivity enhancement versus aggregate size for various fractal dimensions. This shows the ratio becomes much higher than the favorability limit of 4 as the aggregates become larger at the lower fractal dimensions with less dense aggregates that consume more volume.

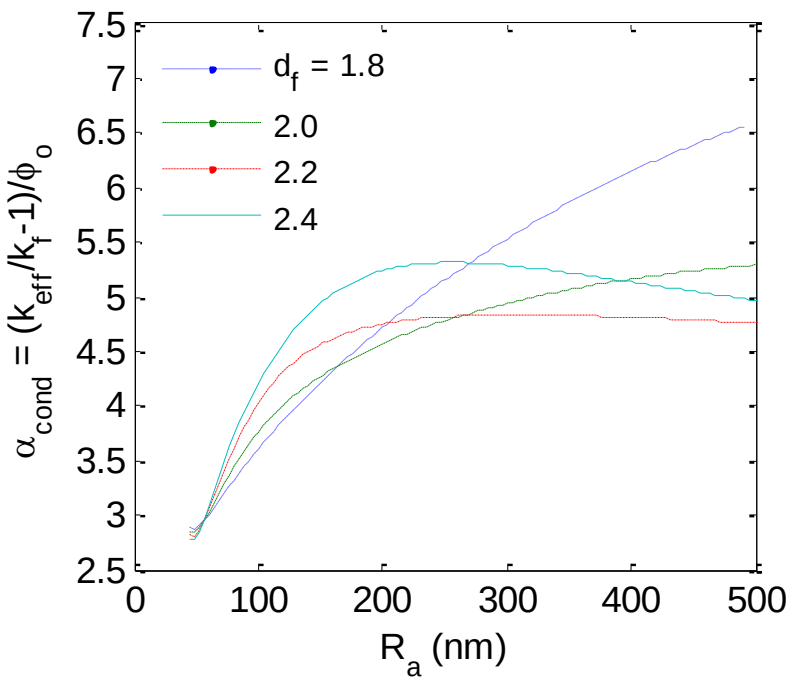

Figure 4.3: Calculated normalized thermal conductivity enhancement versus aggregate radius of gyration for 40 nm alumina nanoparticles in water for various fractal dimensions.

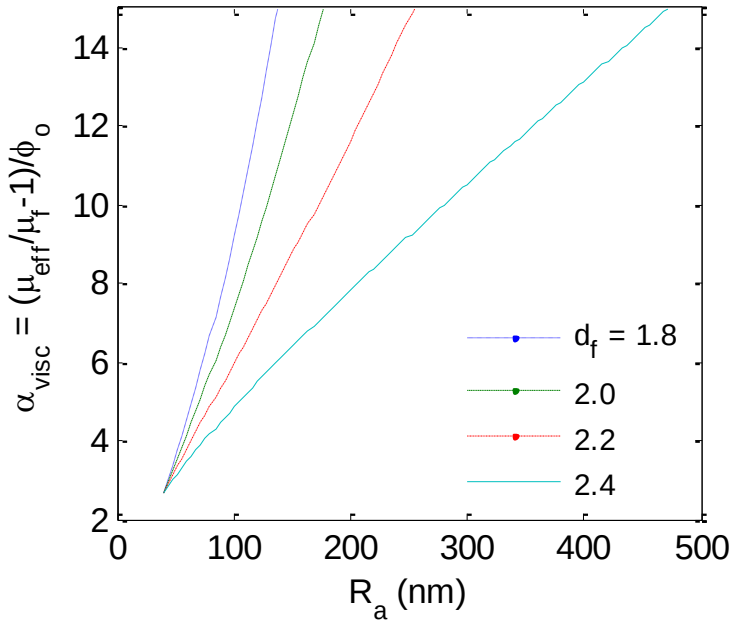

Figure 4.4: Calculated normalized viscosity enhancement versus aggregate radius of gyration for 40 nm alumina nanoparticles in water for various fractal dimensions.

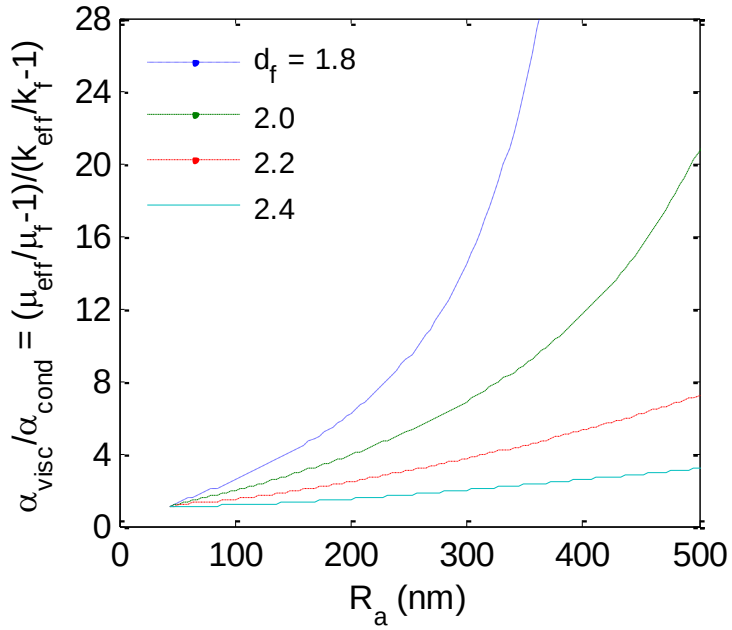

Figure 4.5: Calculated ratio of viscosity to thermal conductivity enhancement versus aggregate radius of gyration for 40 nm alumina nanoparticles in water for various fractal dimensions.

From the work of Potanin et al. [99] it is expected that in shear conditions the aggregates will compress. They showed increases in the fractal dimension from 1.8 to 2.3 in oscillating shear flows. Even with diffusion limited aggregation the nanofluid could remain favorable up to very large aggregate sizes.

4.3.2 Non-interacting Particles

For each Monte Carlo simulation, the particle sizes are distributed based on the DLS measurements of the nanofluid with imposed nominal particle sizes of 40, 60, 80, and 130 nm. Concentrations of 1%, 3%, and $5\%_{vol}$ are used. The temperature of the cold boundary is held at 20 ^{o}C and a heat flux of 4 W/cm^2 is applied at the opposite boundary as in the experiments. For the full Monte Carlo simulation, d_f is taken as 1.8, which was the average measured fractal dimension for our aggregate formations using static light scattering and d_l is taken as 1.0, 1.4, and 1.6 where the value of 1.4 corresponds to the typical value found for suspensions.[70]

The steady state solution from the Monte Carlo model without aggregation and the numerical model are fitted using S_T as the fitting parameter. The concentration profile from the Monte Carlo simulation and the numerical model with a Soret coefficient of 0.025 K^{-1} are plotted in Figure 4.6 at multiple times. This value compares well to estimated maximum values of 0.01 and 0.1 K^{-1} for C_{60}-C_{70} fullerenes and 4 nm gold particles respectively by Putnam et al. [101]. The comparison also holds for estimations by Savino et al. [76] of S_T for suspensions of nanosized particles on the order of 10^{-1} to 10^{-2} K^{-1}.

This plot shows good agreement in both the magnitude and shape of the curves. The predicted concentration profile yields a variation from 35% above the base concentration at the cold wall and 30% below the base concentration at the hot wall. This results in a 60% variation in the concentration across the fluid at steady state.

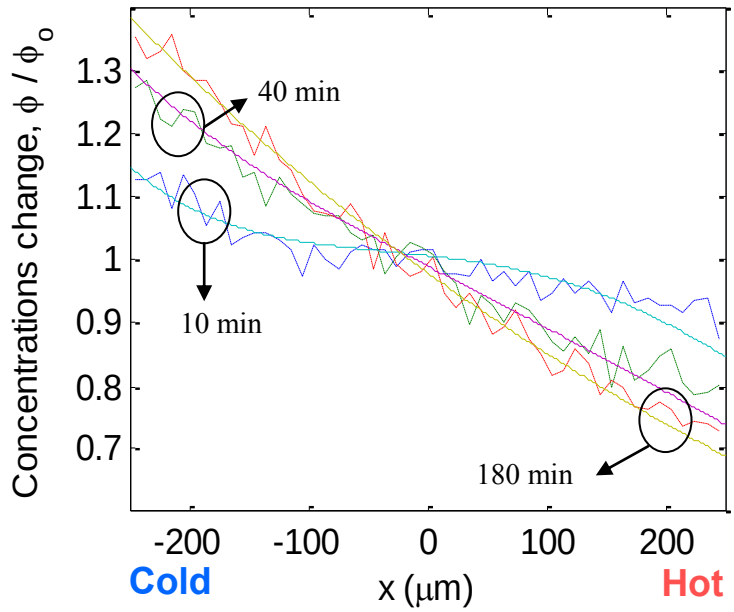

Figure 4.6: Calculated normalized particle distribution from Monte Carlo simulation without aggregation or particle interaction (dashed) and numerical model (solid) for a S_T of 0.025 K^{-1} and d of 40 nm at times of 10, 40 and 180 minutes for alumina nanoparticles in water subjected to a heat flux of 4 W/cm^2.

4.3.3 Isothermal Aggregation

To determine the effect of aggregation at various concentrations and temperatures, the Monte Carlo simulation is run in isothermal conditions. By conducting the Monte Carlo simulation, a distribution of aggregate sizes is formed including remaining single particles. Plotted in Figure 4.7 is the modeled average radius of gyration with an assumed fractal dimension of 1.8 for each of the concentrations and temperatures. For the $1\%_{vol}$ concentration the average radius of the aggregates stays smaller than 40 nm, less than double the initial particle radius and smaller than the permanent aggregates.

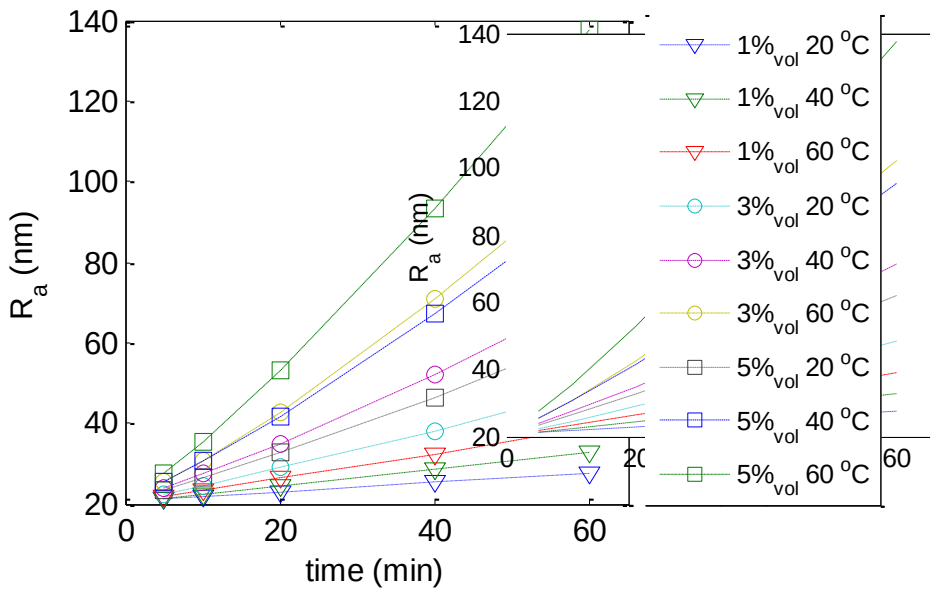

Figure 4.7: Simulated average radius of gyration of the aggregates over time for 1%, 3%, and 5%$_{vol}$ concentrations at 20, 40, and 60 °C.

For the 3%$_{vol}$ concentration, the aggregates remain small for the 20 °C case. At 40 °C, the aggregates begin to approach an 80 nm average radius of gyration, over triple the size of the initial particles and larger than the permanent aggregates. At 60°C, the aggregation occurs more quickly and the aggregates grow to an average radius of gyration of over 100 nm, more than five times the average initial particle size and almost double the size of the permanent aggregates. For the 5%$_{vol}$ concentration, the average radius of gyration of the aggregates is predicted to increase to the size of the permanent aggregates at all temperatures and become much larger for 40 °C and 60 °C.

4.3.3.1 Effect on Fluid Properties

The thermal conductivity and viscosity of the nanofluid is calculated from the volume averaged aggregate size. The calculated thermal conductivity over time is plotted in Figure 4.8. For the 1%$_{vol}$ concentration, there is no change in the thermal

conductivity over the cour at any of the simulated temperatures even with the m ıggregate radius of gyration.

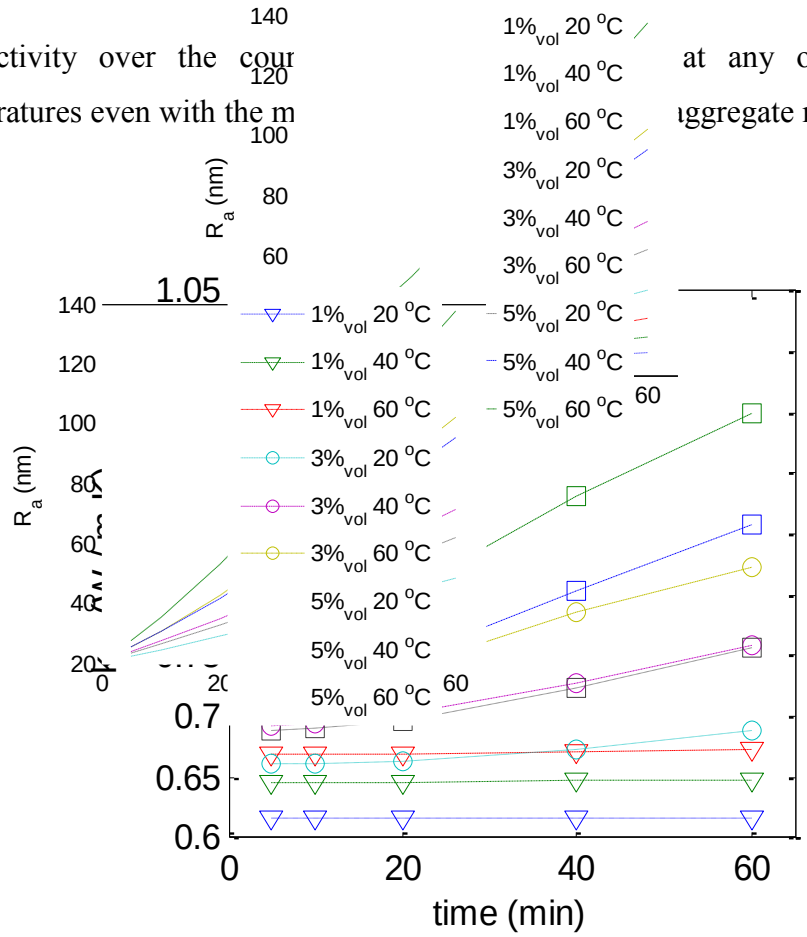

Figure 4.8: Predicted thermal conductivity plotted over time for the three concentrations each at the three temperatures calculated from the volume average of the simulated aggregate radius of gyration for a fractal dimension of 1.8 in a nanofluid with 40 nm alumina nanoparticles dispersed in water.

For the $3\%_{vol}$ concentration, an increase of less than 5% in the thermal conductivity is predicted at 20 °C over the course of the simulated hour. At 40 °C, the increase in thermal conductivity becomes 10%. At 60 °C, the thermal conductivity increases by almost 15%. For the $5\%_{vol}$ concentration, the increase is 10%, 18%, and 26% for 20, 40, and 60 °C, respectively.

The viscosity calculations are plotted in Figure 4.9. For the $1\%_{vol}$ concentration, there is no apparent increase in viscosity over the simulated time at any

of the temperatures modeled due to only a small amount of aggregation occurring. For the 3%$_{vol}$ concentration, the viscosity increases by 10%, 18%, and 45% for the 20, 40, and 60 ^{o}C temperatures, respectively. the viscosity increases by 25%, 65%, and 100% for , and 60 ^{o}C, respectively.

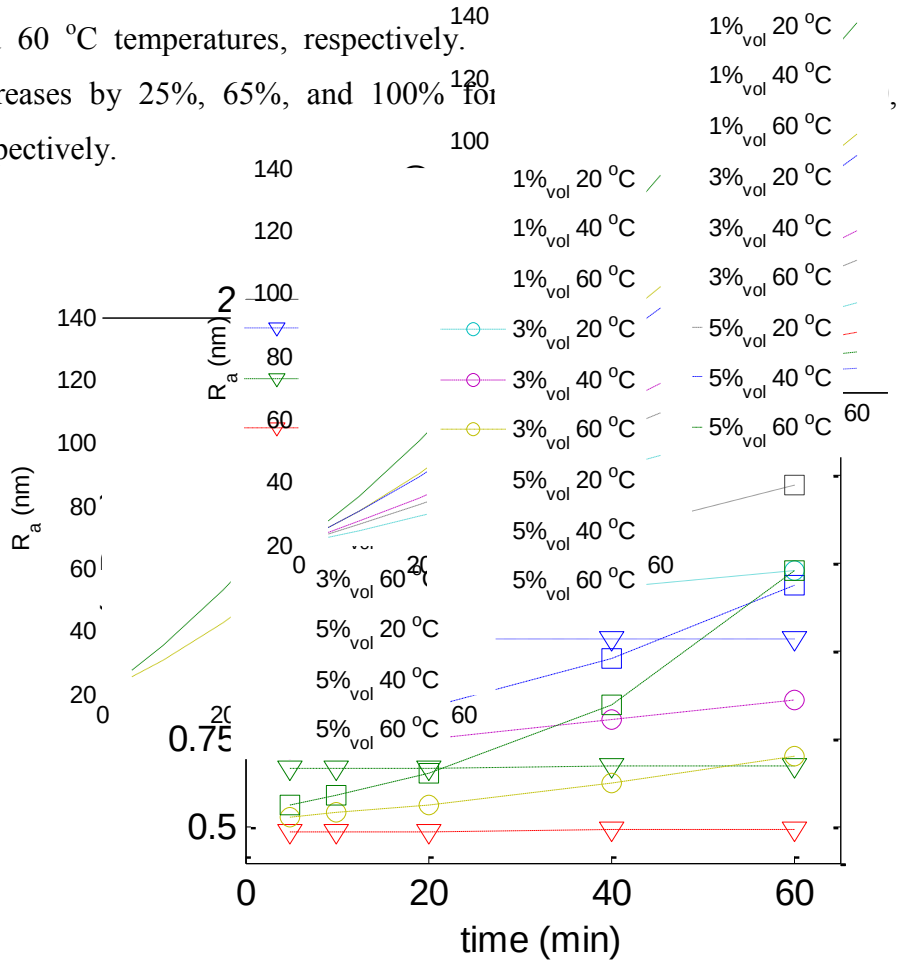

Figure 4.9: Calculated viscosity plotted over time for the three concentrations each at the three temperatures calculated from the volume average of the simulated aggregate radius of gyration for a fractal dimension of 1.8 in a nanofluid with 40 nm alumina nanoparticles dispersed in water.

The rate of increase in viscosity increases over time. Thus the viscosity increases faster at larger aggregate sizes. To compare the increases in thermal conductivity and viscosity, the ratio of the enhancements is plotted in Figure 4.10. For the cases simulated, the ratio stays below the limit of 4 for a favorable nanofluid. Early in the simulation of lower volume concentrations, before aggregation has progressed far enough to greatly affect the fluid properties, the ratio is in the ideal

region of below 1, which ve medium theories for the thermal conductivity and vi

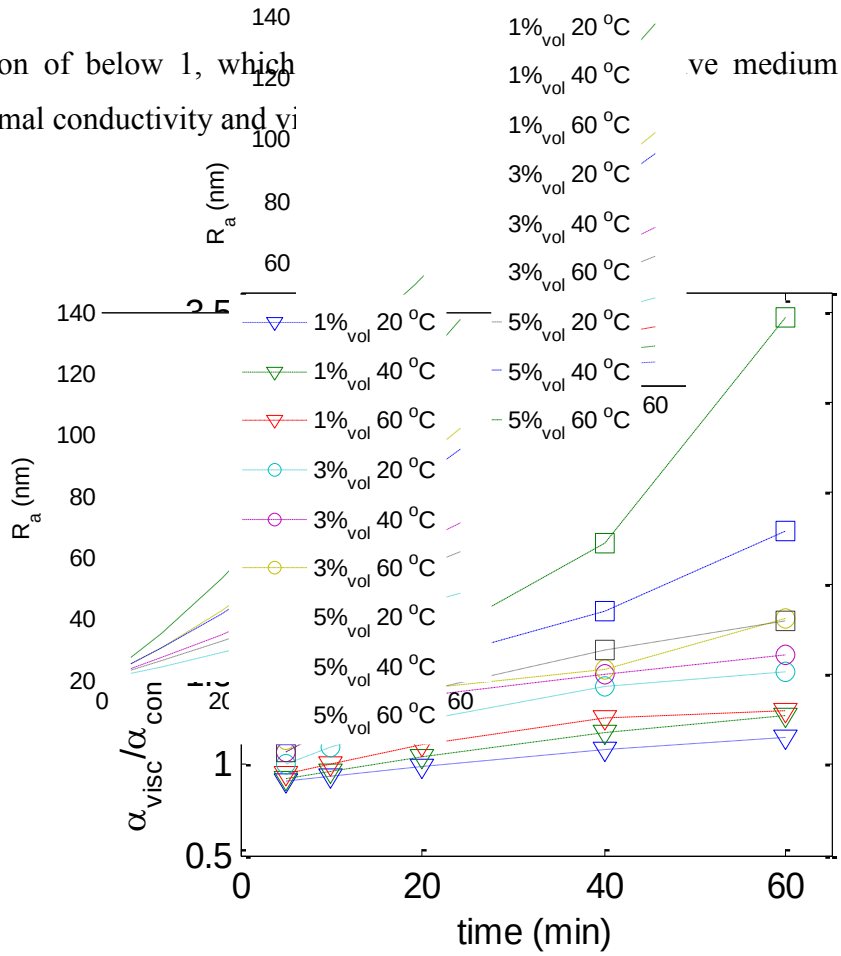

Figure 4.10: Calculated ratio of the viscosity to thermal conductivity enhancements plotted over time for the three concentrations each at the three temperatures calculated from the volume average of the simulated aggregate radius of gyration for a fractal dimension of 1.8 in a nanofluid with 40 nm alumina nanoparticles dispersed in water.

4.3.3.2 Comparison with Measurements

Comparing the simulation of the average radius of gyration of the aggregates to the static light measurements, there is very good correlation. For the $1\%_{vol}$ fraction, the simulation shows evidence of very little aggregation with small aggregate formation sizes. The light scattering at all temperatures and times yields a fractal dimension of 2.4 showing a dominance of the permanent aggregates and no evidence of aggregate formations over time.

For the $3\%_{vol}$ fraction, the simulation shows only slight aggregation and small aggregate sizes, which is consistent with the measured average fractal dimension of 2.4. At 40 ^{o}C, the simulation shows the aggregates becoming larger than the permanent aggregates in the fluid, which is consistent with the reduction in the fractal dimension at the longer length scales where fewer permanent aggregates are present. At 60 ^{o}C, the simulation shows even more aggregation occurring and the aggregates becoming even larger. The light scattering data show a small reduction in the measured fractal dimension over time at the shorter length scales from the aggregate formations becoming more numerous. At the longer length scales the fractal dimension reduces more showing evidence of more aggregate formations larger than the majority of the permanent aggregates.

For $5\%_{vol}$ concentration, the simulation shows aggregates sizes for the 20 ^{o}C temperature similar to that of the 3% at 40 ^{o}C, but the light scattering shows fractal dimensions of 2.4 at both length scales and times. This is likely due to the stabilization optimized for room temperature preventing major aggregation. At 40 ^{o}C, the simulation shows similar aggregate sizes to the 3% at 60 ^{o}C and the light scattering shows the same effect with essentially the same fractal dimensions measured at each length scale and time. At 60 ^{o}C, the simulation shows the aggregation occurs very quickly within the time period for the measurement to begin and the aggregates become much larger than the permanent aggregates in the fluid. From the light scattering this is apparent since for the shorter length scale the initial fractal dimension is measured to be 2.2 and reduces to 2.0 showing large effects of the lower fractal dimension aggregates. At the longer length scale the aggregate formations dominate the measurement and an average fractal dimension of 1.8 is measured.

The measured average thermal conductivity also shows similarity to the calculated thermal conductivity from the simulations at 60 ^{o}C for each of the volume concentrations. Although, this simulation only models the aggregation, it still captures the primary means of aggregate formation and its effects on the thermal conductivity at elevated temperatures.

4.3.3.3 Particle Size Effect

Given the dependence of the rate of aggregation, diffusion and settling on particle size with seemingly no dependence of the fluid properties, it is interesting to look at the effects of particle size. To study these effects on the aggregation, the simulation is run for the same concentration, 5% by volume, at four particle sizes, 40 nm, 60 nm, 80 nm, and 130 nm. The results for the change in average radius from the initial radius after an hour for each particle size and for temperatures of 20 ^{o}C, 40 ^{o}C and 60 ^{o}C are plotted in Figure 4.11.

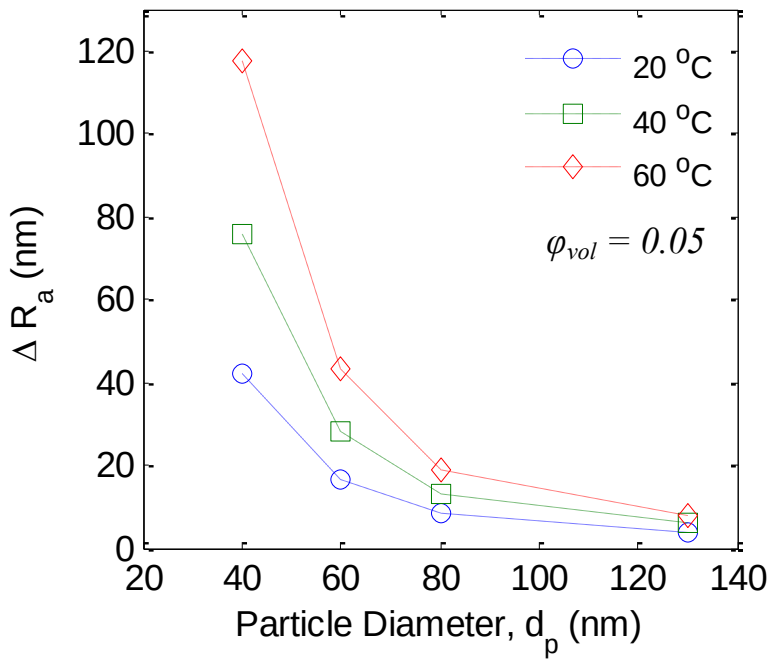

Figure 4.11: Plot of the simulated change in size after an hour versus initial particle diameter for three temperatures in a water based nanofluid at a $5\%_{vol}$ concentration.

As the particle size is increased for the same volume fraction, the number of particles is reduced. The larger particles experience less motion due to Brownian motion since Stoke's drag goes as the particle diameter. Thus the larger particles

sample less volume over time and interact less frequently. Large changes in the average size are seen for the smallest particle size of 40 nm. When the particle size is increased to 130 nm, very little aggregation occurs over the course of the simulation and little variation with temperature is apparent.

4.3.4 Thermal Diffusion and Aggregation

In this section, the combination of aggregation and thermal diffusion are simulated and the results compared to measurements. From the results and comparisons the effects of aggregation and thermal diffusion on the nanofluid properties and favorability become apparent.

4.3.4.1 Concentration Effects

The distribution of the average radius of gyration of the aggregates across the nanofluid for the three concentrations is shown for various times in Figure 4.12. The waviness of the data is due to the local effects of large aggregates. As the simulation is run multiple times and averaged the waviness is reduced. As the particles diffuse towards the cold region aggregation takes place faster than in the particle depleted regions. In the $1\%_{vol}$ concentration, the aggregates stay small for the first hour with some noticeable aggregation in the cold region. After another hour the aggregation in the cold region increases further.

In the $3\%_{vol}$ concentration, the aggregate radius of gyration grows after an hour to over 50 nm in the hot region and 100 nm in the cold region. After two hours, the aggregate radius in the hot region is 140 nm and 200 nm in the cold region. In the $5\%_{vol}$ concentration, after one hour the aggregate radius of gyration reaches 150 nm in the cold region and 100 nm in the hot region. After two hours, the radius increases to 250 nm in the cold region and 200 nm in the hot region. These results show a definite

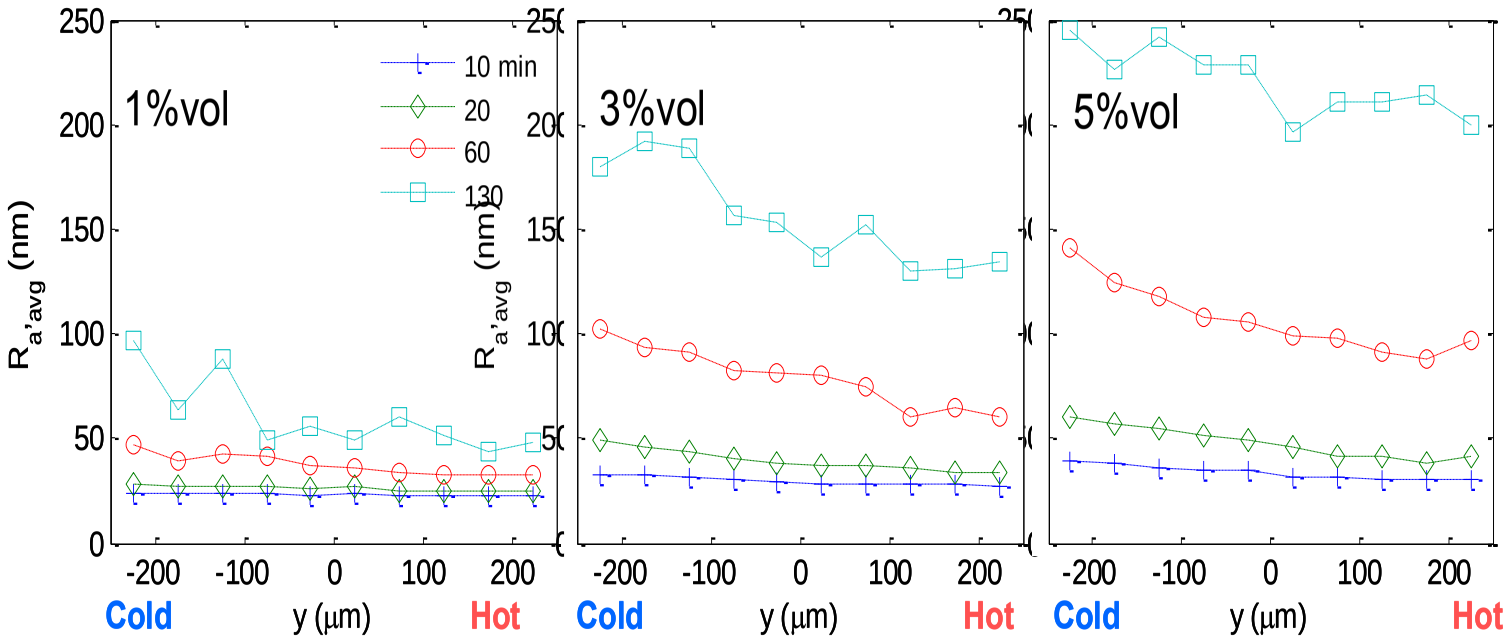

Figure 4.12: Predicted average aggregate radius of gyration distribution across the nanofluid at various times from the Monte Carlo simulation for 1%, 3%, and 5%$_{vol}$ concentrations of nominal diameter alumina nanoparticles in water subjected to a heat flux.

effect of thermal diffusion on aggregation. When compared to the isothermal aggregation simulation, aggregation occurred faster in the higher temperatures. However, with a temperature gradient, the diffusion of the particles towards the cold region and increase in concentration results in fast aggregation at the colder temperatures.

The average radius of gyration for each of the concentrations over the simulated time is plotted in Figure 4.13. These results match well with the isothermal case for 60 ^{o}C. As expected, the aggregates in the higher concentration grow faster.

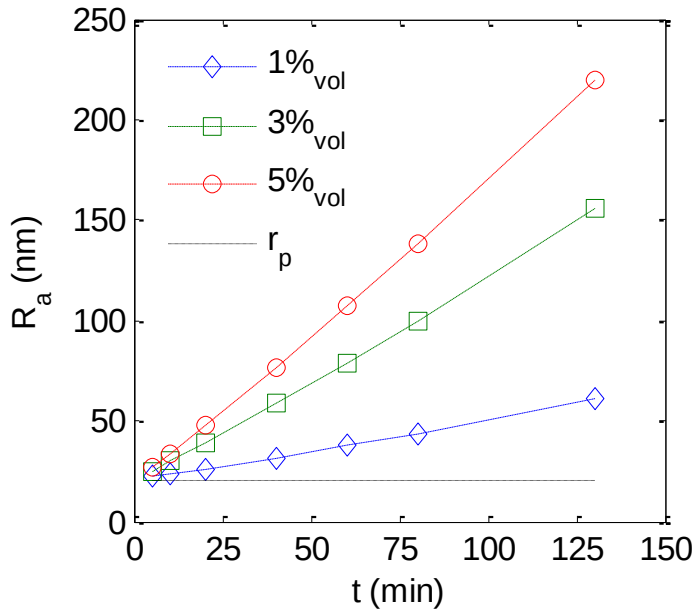

Figure 4.13: The simulated average radius of gyration of the aggregates in the nanofluids over time for the three concentrations of the nanofluid of 40 nm alumina nanoparticles in water.

The normalized particle volume concentration distribution for each concentration and various times is shown in Figure 4.14. The particles and aggregates diffuse towards the cold region as expected from thermal diffusion. The simulation without aggregation showed a normalized concentration varies between 1.35 on the cold end and 0.7 on the hot end. The simulation with aggregation shows are larger variation across the nanofluid. For the 1%$_{vol}$ concentration, the normalized concentration varies

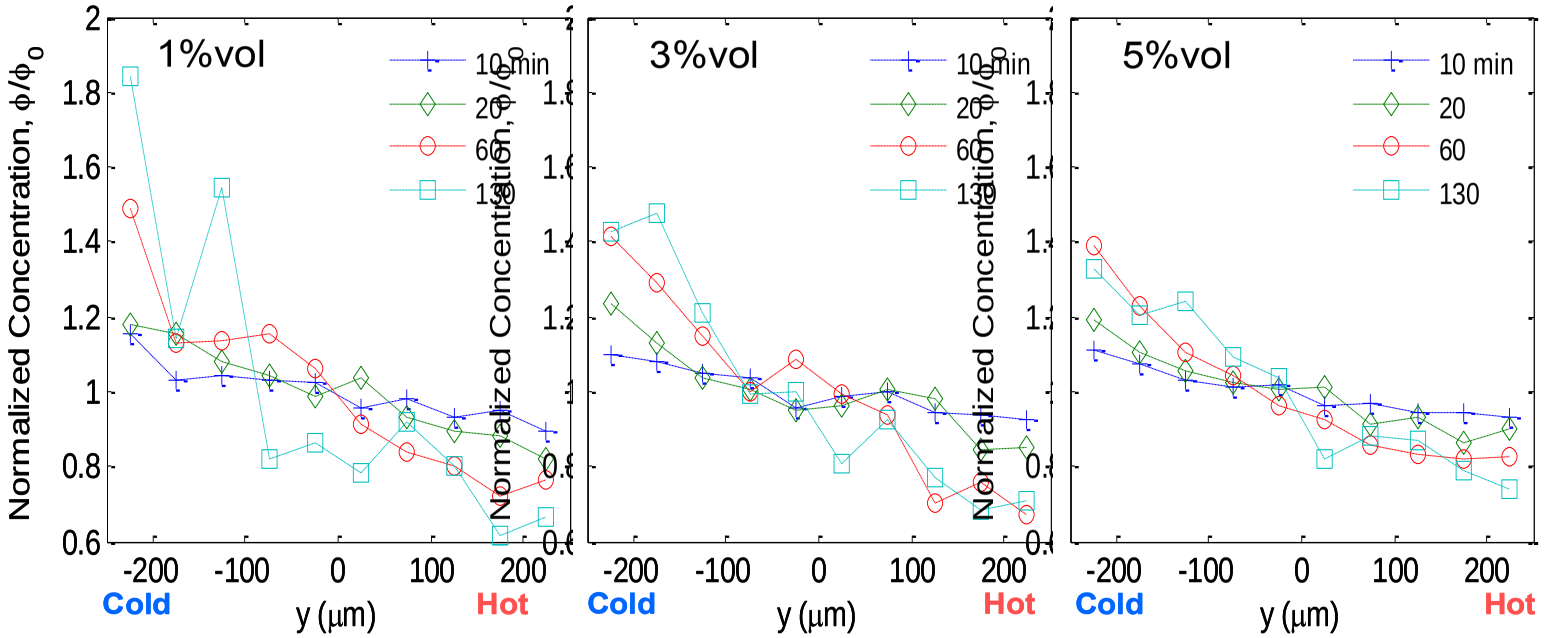

Figure 4.14: Simulated volume concentration distribution across nanofluid at various times from the Monte Carlo simulation for 1%, 3%, and $5\%_{vol}$ concentrations of 40 nm nominal diameter alumina nanoparticles in water subjected to a heat flux.

between 1.6 and 0.6. For the $3\%_{vol}$ concentration, the normalized concentration varies between 1.5 and 0.65. For the $5\%_{vol}$ concentration, the normalized concentration varies between 1.4 and 0.65. This is most likely due to the variation in aggregate size across the nanofluid.

As the aggregates in the cold region become larger their Brownian motion is reduced even further, while the aggregates in the hot region do not become as large and their motion is less inhibited. The larger variation is more evident in the lower concentration since the diffusion progressed before the aggregates became large. After the majority of the diffusion had occurred the aggregates became larger mainly in the cold region where the higher concentration was located. In the higher concentrations, the aggregates became large while the diffusion progressed, slowing the diffusion, and reducing this effect.

The predicted thermal conductivity distribution from the Monte Carlo simulation for each concentration at various times is shown in Figure 4.15. The time evolution of the thermal conductivity for the $1\%_{vol}$ concentration is very small during the first hour of simulated time. When taken to two hours, the simulation begins to show a rise in the thermal conductivity in the cold region with an increase of about 10% from the initial state while the hot region shows no change, which is expected from the average aggregate radius of gyration distribution.

For the 3% and $5\%_{vol}$ concentrations, the increases in thermal conductivity begin to occur early and become large after an hour of simulated time. The thermal conductivity increases across the whole nanofluid as aggregation occurs. The cold region experiences much larger increases in the thermal conductivity than the hot region in both concentrations and larger aggregate sizes present in the cold region compared to the hot region. These results correspond with the higher concentrations and larger aggregate sizes present in the cold region compared to the hot region shown in the average radius of gyration distribution. As aggregation progresses, large aggregates form and fewer individual aggregates and particles and present in the fluid.

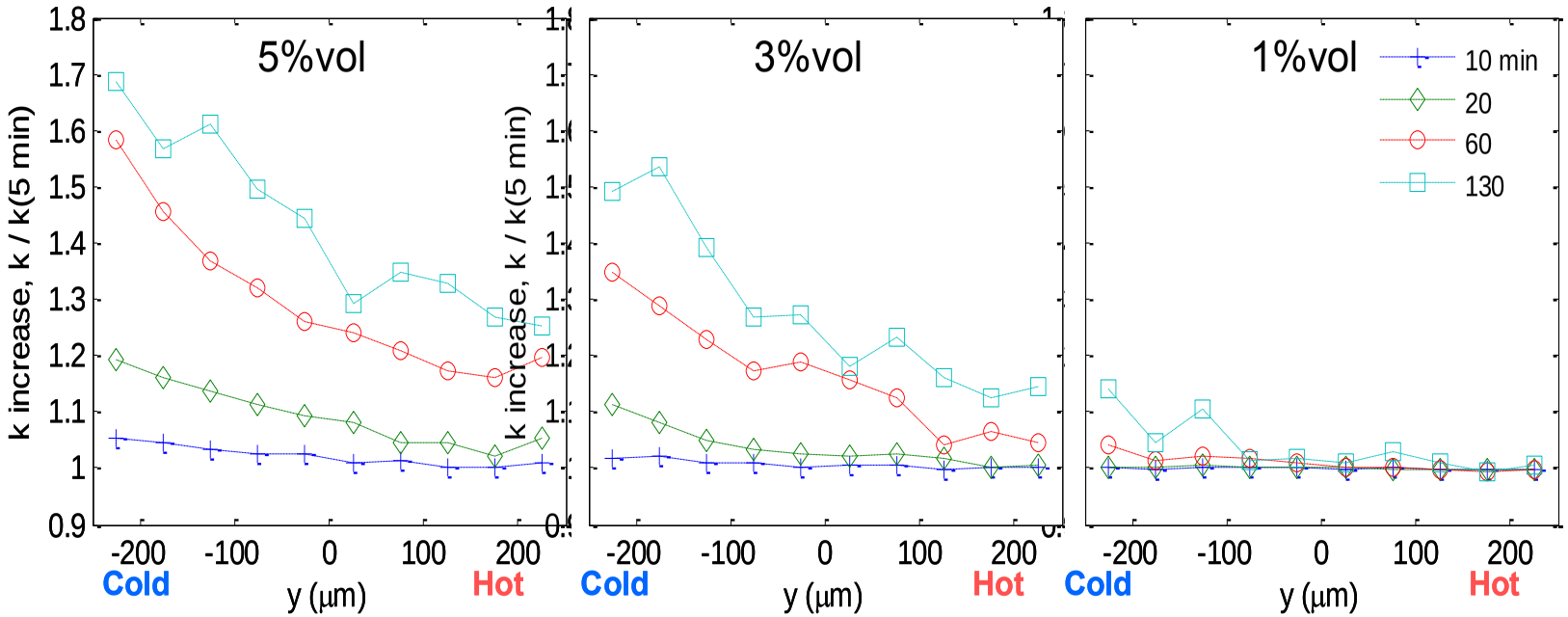

Figure 4.15: Simulated thermal conductivity distribution across the nanofluid at various times from the Monte Carlo simulation for 5%, 3% and $1\%_{vol}$ concentrations of 40 nm nominal diameter alumina nanoparticles in water subjected to a heat flux.

This creates greater waviness in the data, which is most apparent at the later times when aggregation has progressed the furthest.

The average thermal conductivity over time for each of the three concentrations is plotted in Figures 4.16 and 4.17. Figure 4.16 shows a plot of the average thermal conductivity over time with and without the inclusion of boundary resistance. The boundary resistance used, 0.77x 10^{-8} K m^2/W, for this simulation is a typical value for alumina and water. The thermal conductivity taking boundary resistance into account lowers the average effective thermal conductivity by less than *5%*. Figure 4.17 shows a plot of the average thermal conductivity over time for chemical dimensions between 1 and 1.6. There is little variation at early times with less aggregation. A variation of 5% between 1 and 1.6 cases occurs after two hours of simulated time. For this case neither boundary resistance nor chemical dimension has a major effect on the calculated thermal conductivities. Both are ignored for the remainder of the study.

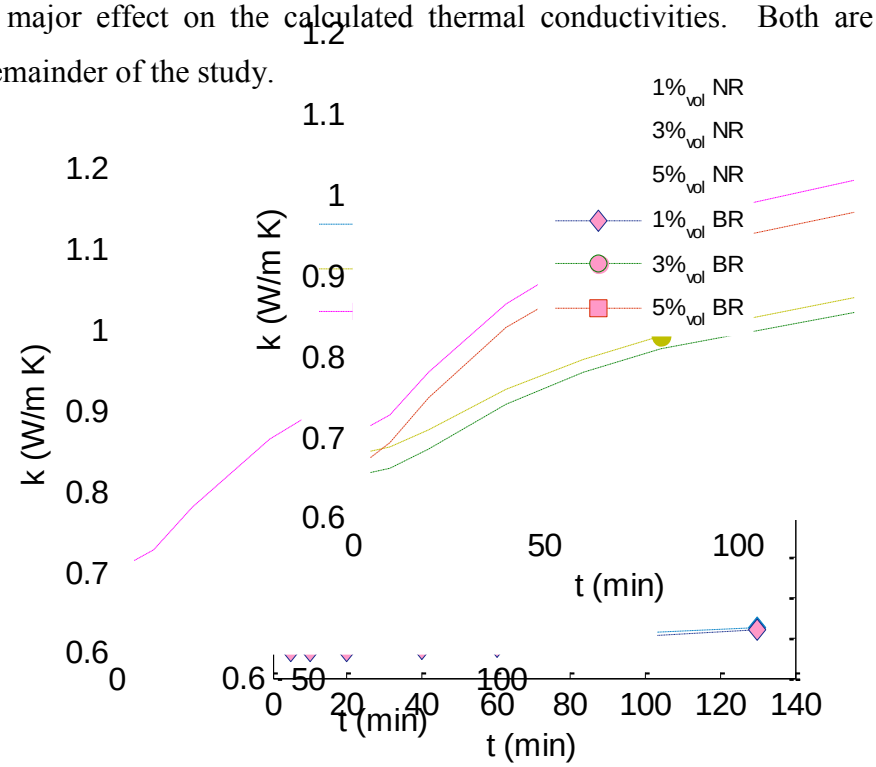

Figure 4.16: Plot of the simulated average thermal conductivity over time from the Monte Carlo simulation with no boundary resistance (dashed) and with typical boundary resistance of 0.77 m^2K/W between alumina and water (dash - dot).

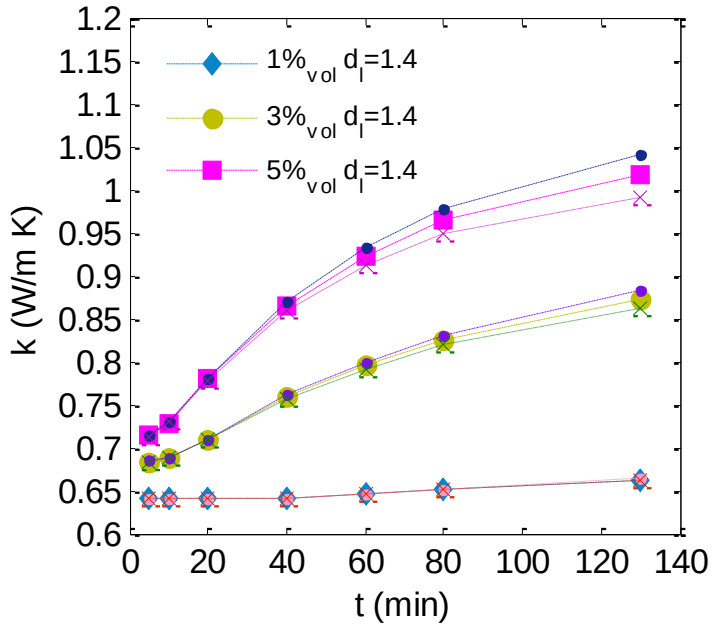

Figure 4.17: Plot of the simulated average thermal conductivities over time from the Monte Carlo simulation for the 1%, 3% and $5\%_{vol}$ concentrations for d_l = 1 (dot / x), 1.4 (dash) and 1.6 (dash-dot / .).

4.3.4.2 Comparison with Thermal Measurement

The average thermal conductivity from the Monte Carlo simulation and the experimental measurement for each concentration are plotted in Figure 4.18. The simulation and the experiment show good agreement in both magnitude and curvature. Both show the thermal conductivity increase flattening over time as aggregation progresses. The experimental data appears to be shifted in time to the left. This may be due to the nanofluid sitting for 10 to 15 min after sonication while the IR system is calibrated to the new surface emissivity at multiple temperatures, which would allow aggregation to occur before the measurement begins. Figure 4.19 shows a plot of the average thermal conductivity for the simulation and experiment with the experimental data shifted by 10 minutes. With the time shift in the experimental data the agreement improves. The measured values for the $5\%_{vol}$ concentration case are still slightly higher, which is likely due to the pre-aggregation.

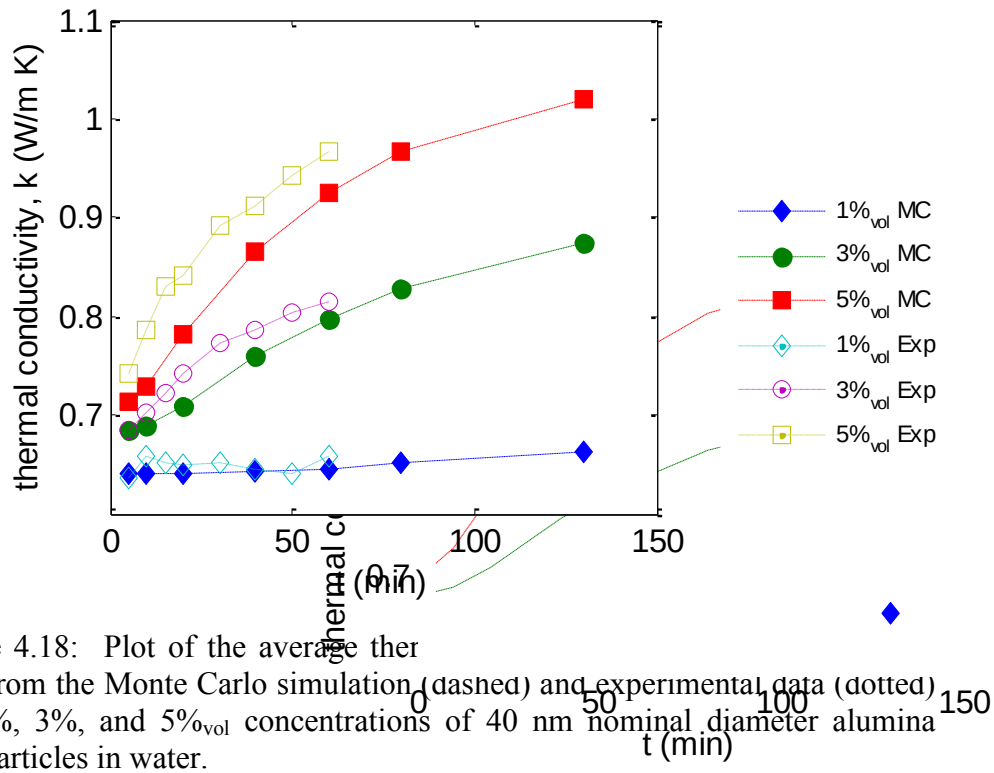

Figure 4.18: Plot of the average ther
time from the Monte Carlo simulation (dashed) and experimental data (dotted) for 1%, 3%, and 5%$_{vol}$ concentrations of 40 nm nominal diameter alumina nanoparticles in water.

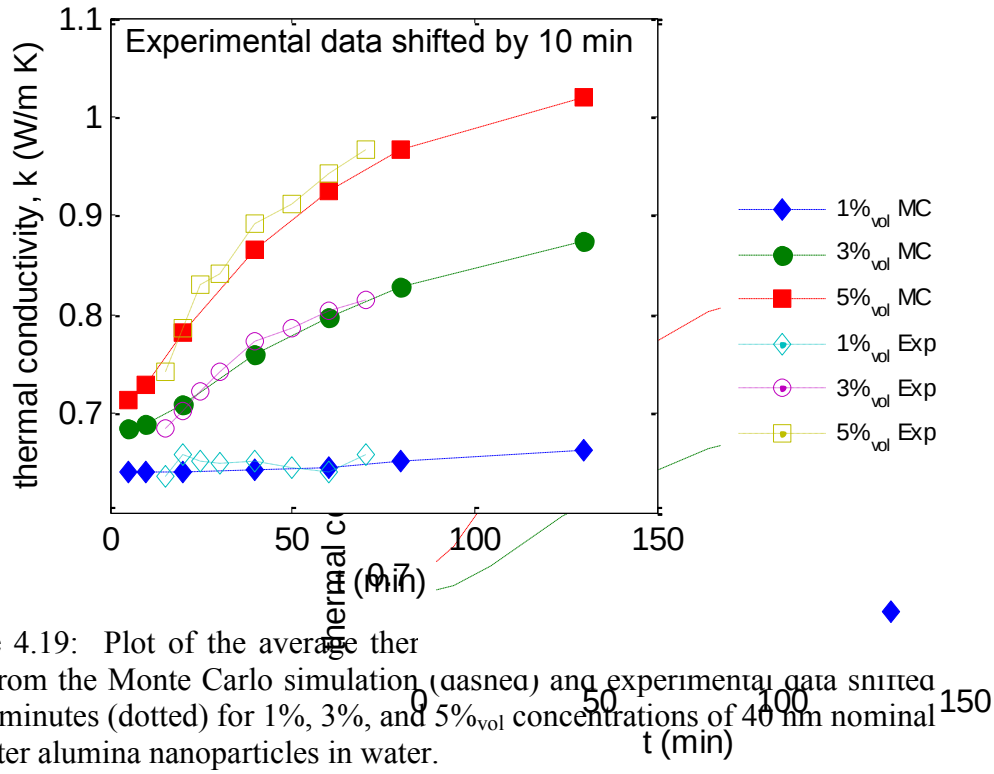

Figure 4.19: Plot of the average ther
time from the Monte Carlo simulation (dashed) and experimental data shifted by 10 minutes (dotted) for 1%, 3%, and 5%$_{vol}$ concentrations of 40 nm nominal diameter alumina nanoparticles in water.

The main differences between the measurement and the simulation are with the thermal conductivity distribution shown in Figure 1.4 for the experiment and Figure 4.17 for the Monte Carlo simulation. In both the simulation and experiment the variations in thermal conductivity are small for the $1\%_{vol}$ concentration and the two match well. At the higher concentrations this is not the case.

For the $3\%_{vol}$ concentration both the simulation and experiment show larger increases in the cold region than in the hot region. However, the simulation predicts more of an increase in the cold region than measured and a larger variation across the fluid. For the $5\%_{vol}$ concentration the experiment shows a constant increase in thermal conductivity across the whole nanofluid. The simulation shows much larger increases in the cold region than the hot region similar to the $3\%_{vol}$ concentration.

These differences between the simulation and experiment for the 3% and $5\%_{vol}$ concentrations are likely due to two effects. First, the time lapse between the sonication and the measurement for calibration may have allowed enough aggregation to occur to impede the initial thermal diffusion. This would reduce the concentration gradient and the variation in aggregate size across the nanofluid. Second, the stabilization of the nanoparticles in the fluid optimized for room temperature. Since the stabilizing electrolytes tend to dissociate at higher temperatures more dissociation may occur in the hot region than the cold causing less aggregation than expected to occur in the cold region. Since the static light scattering measurements at 3% and $5\%_{vol}$ concentrations agreed well with the isothermal aggregation simulation it is more likely that aggregate occurred during the multi-temperature calibration reducing the thermal diffusion. This would effect the higher concentration more since the aggregation progress faster at the higher concentration, which is consistent with the measurement.

To check if this effect could cause the difference, the Monte Carlo simulation is rerun for the $5\%_{vol}$ concentration case. For this check the simulation is run with isothermal aggregation occurring for the first 10 minutes at 40 ^{o}C and then at 10 minutes the heat flux is applied with the previous boundary conditions. The resulting

thermal conductivity distribution is plotted in Figure 4.20. As expect the aggregation reduces the thermal diffusion enough to eliminate the spatial variation in the thermal conductivity as in the measurement. The simulation of purely Brownian motion based aggregation and thermal diffusion account for the variations in thermal conductivity both spatially and temporally.

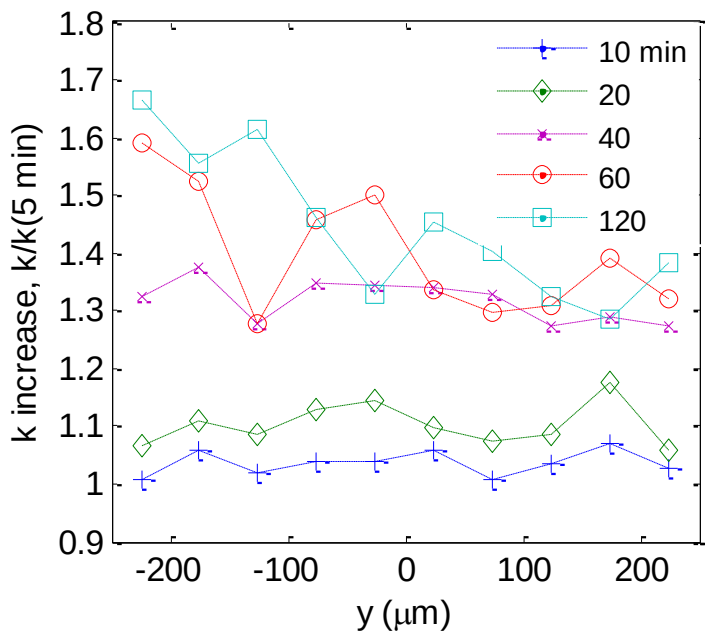

Figure 4.20: Plot of the simulated thermal conductivity of the $5\%_{vol}$ concentration of 40 nm alumina particles suspended in water subjected to a 40 ^{o}C isothermal condition for the first 10 minutes then to a 4 W/cm^2 heat flux.

4.3.4.3 Effective Viscosity

The predicted viscosity distribution from the Monte Carlo simulation for the $3\%_{vol}$ concentration is shown in Figure 4.21. For this set up, the expected increase in the viscosity from the hot region to the cold region is a factor of 1.7. Diffusion of particles towards the cold region and more aggregation in the cold region causes the

viscosity variation across the cavity to double from the variation due to the temperature gradient. In flow it is expected that the aggregates may compress from the shear forces reducing the viscosity. The shear effects of the flow will also cause a greater concentration distribution and thus viscosity distributions as particles are forced towards the center of the cavity cross-section away from the cavity walls.

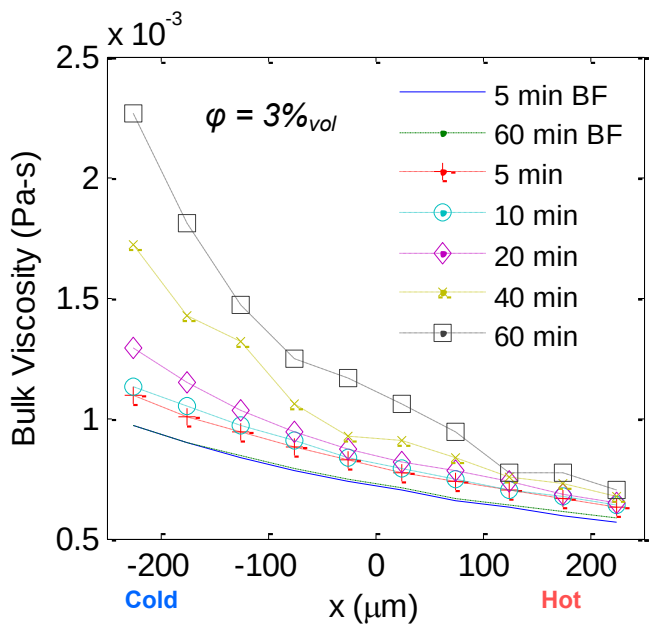

Figure 4.21: Calculated viscosity distribution of the base fluid and nanofluid across the cavity at various times from the Monte Carlo simulation for $3\%_{vol}$ concentrations of 40 nm nominal diameter alumina nanoparticles in water subjected to a heat flux.

The ratio of the calculated viscosity enhancement factor, given by the equation $\alpha_{visc} \equiv \left(\mu_{eff}/\mu_f - 1\right)/\varphi$, and thermal conductivity enhancement factor, given by the equation $\alpha_{cond} \equiv \left(k_{eff}/k_f - 1\right)/\varphi$, for the three volume concentrations is plotted in Figure 4.22. The average viscosity and thermal conductivity at each time is used as the effective value. The results are similar to those from the isothermal aggregation. For the first hour the ratio stays below the favorability limit of 4 for the 1% and $3\%_{vol}$ concentrations.

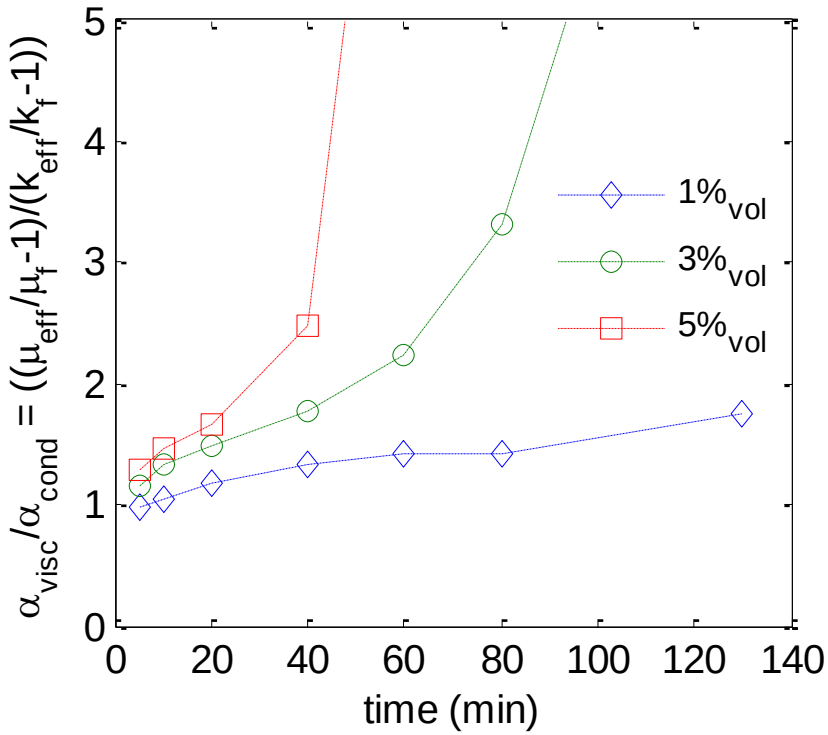

Figure 4.22: Plot of the calculated ratio of viscosity increase to thermal conductivity increase over time from the full Monte Carlo simulation for the three concentrations of 40 nm alumina nanoparticles suspended in water.

The 5% shows the ratio increase dramatically before the end of the first hour. This is much greater than the prediction from the isothermal aggregation case, which showed the ratio remaining below the favorable limit of 4 for all concentrations and temperatures over a one hour period. The main difference between the two simulations is the diffusion of particles creating a region of higher concentration and more aggregation. At larger amounts of aggregation the rate the viscosity increases with aggregation increases. The greater aggregation in the cold region causes a larger increase in average viscosity than the lessened aggregation in the hot region. For the lower volume concentration and with less aggregation the ratio stays below the limit of favorability.

4.3.4.4 Particle Size Effects

Given the good agreement between the simulation and measurements, the Monte Carlo simulation is used to predict the results for cases not measured experimentally. The effect of the particle size is of great interest due to the strong dependence of the rate of aggregation, diffusion, and settling on the particle size with little impact on the effective medium theories as long as the particles remain small. Figure 4.23 is the plot of the average radius of gyration of the aggregates over time predicted by the Monte Carlo simulation for $5\%_{vol}$ concentration and particle diameters of 40 nm, 60 nm, 80 nm, and 130 nm. As the particle size increases the amount of aggregation decreases due to the reduced movement and a fewer number of particles. After two hours, the aggregates for the 40 nm particles are over 10 times the individual particle size. The case of the 60 nm particles gives a large reduction in the aggregate size, which is 3 times the individual particle size. For 80 nm particles the aggregates after 2 hours are less than 2 times the individual particle size. The 130 nm particle case shows no increase in size over the 2 hour period.

Figure 4.24 plots the average thermal conductivity over time predicted by the Monte Carlo simulation for the four particle diameters at $5\%_{vol}$ concentration. Due to the decreased amount of aggregation for the larger particles the thermal conductivity enhancement is much less. After two hours the 60 nm and 80 nm cases still show an increase in the rate of thermal conductivity increase due to the much slower progression of aggregation. The 130 nm case that shows no aggregation stays at the imposed effective medium theory prediction.

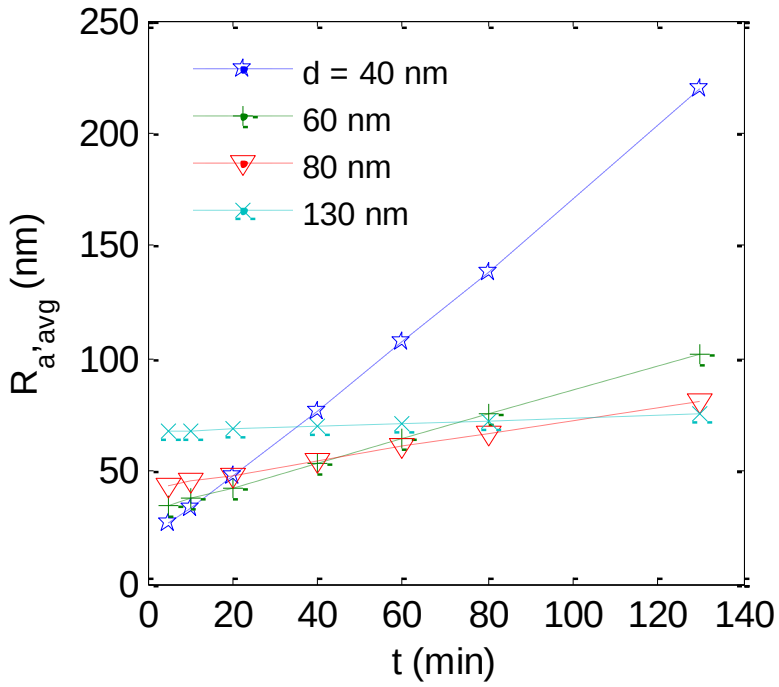

Figure 4.23: Plot of calculated average radius of gyration of the aggregates over time from the Monte Carlo simulation for $5\%_{vol}$ concentration for particle diameters of 40 nm, 60 nm, 80 nm, and 130 nm.

Figure 4.25 plots the ratio of the viscosity and thermal conductivity enhancement factors calculated from the Monte Carlo simulation for $5\%_{vol}$ concentration and the four particle diameters. Due to the reduced aggregation with the larger particles, the ratio stays below the favorability limit of 4 for the 60 nm, 80 nm, and 130 nm particles sizes for the simulated time period at the higher concentration. From the trend, it is likely that at later times the 60 nm case will reach the favorability limit. The 130 nm case is the only case that stays close to the ideal 1:1 ratio.

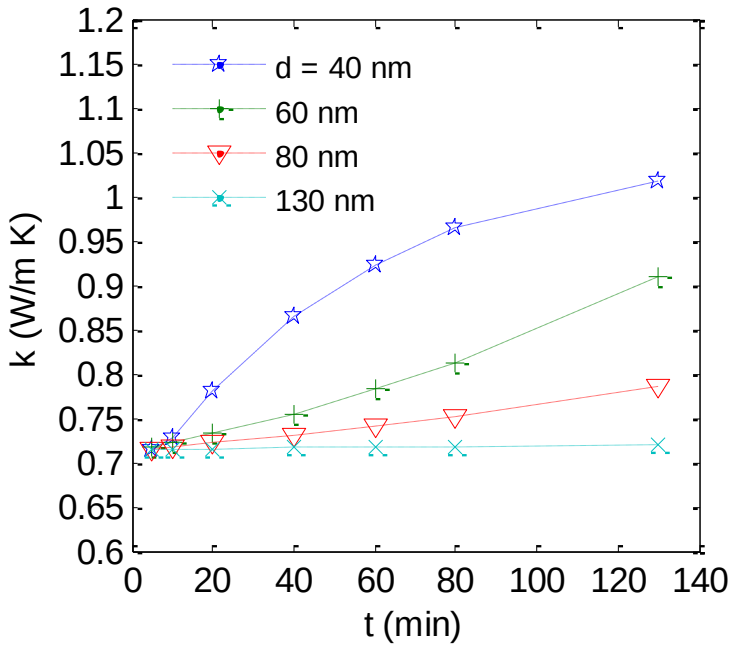

Figure 4.24: Plot of the calculated average effective thermal conductivity over time from the Monte Carlo simulation for 5%$_{vol}$ concentration for particle diameters of 40 nm, 60 nm, 80 nm, and 130 nm.

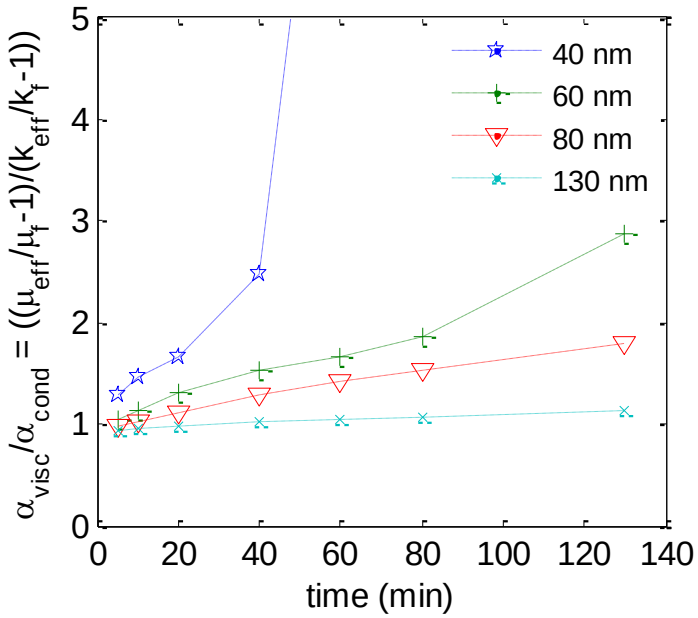

Figure 4.25: Calculated ratio of the average viscosity and thermal conductivity enhancement factor over time from the Monte Carlo simulation for 5%$_{vol}$ concentration and 40 nm, 60 nm, 80 nm, and 130 nm nominal diameters.

4.4 Particle Size Optimization

The variation of aggregation, diffusion and settling with particle size leads to the possibility of an optimum value. To estimate an optimum particle size, the dependence of the aggregation, diffusion and settling time constants on particle size are calculated and compared. The aggregation time constant represents the time for the number of particles to reduce by fifty percent and is given through slow aggregation theory by [102,103]

$$t_p = \frac{\pi \mu_f r_p W}{k_b T \varphi_p} \tag{4.25}$$

where W is the stability ratio given by [104]

$$W = 2r_p \int_0^\infty \frac{B(h)}{\left(h + 2r_p\right)^2} \exp\left(\frac{V_T}{k_b T}\right) dh \tag{4.26}$$

where $B(h)$ is given by [105]

$$B(h) = \frac{6\left(h/r_p\right)^2 + 13\left(h/r_p\right) + 2}{6\left(h/r_p\right)^2 + 4\left(h/r_p\right)} \tag{4.27}$$

h is the distance between the surfaces of the particles and $V_T = V_A + V_R$ is the total potential energy of interaction. V_A is the energy of attraction due to Van der Waals forces and is given by [106]

$$V_A = -\frac{A}{6}\left(\frac{2}{s^2-4}+\frac{2}{s^2}+\ln\frac{s^2-4}{s^2}\right) \tag{4.28}$$

where $s = 2 + h/r_p$. V_R is the electrostatic energy of repulsion due to the electric double layer, which for small values of $\tau = \kappa r_p$ can be approximated by:[106]

$$V_R = \frac{\varepsilon_r \varepsilon_0 \psi^2 r_p}{s}\exp(-\kappa h) \tag{4.29}$$

where $\kappa^2 = 2e^2 N_A I/(k_b T \varepsilon_r \varepsilon_0)$ is the Debye parameter [107], e is the elementary charge, N_A is Avogadro's number, ε_r is the relative dielectric constant of the liquid, ε_0 is the dielectric constant of free space, ψ is the zeta-potential of the particles, I is the concentration of ions in the water which is estimated by the pH as 10^{-pH} for $pH \leq 7$ and $10^{-(14-pH)}$ *for* $pH > 7$. To model the fluid of this study a temperature of 40 ^{o}C and pH of 4 is used.

The time constants for settling and thermal diffusion to reach steady state are calculated by equating the average distance moved by a particle undergoing Brownian motion and distance moved from the respective drift velocity as shown below:

$$\sqrt{2Dt} = u_d t \tag{4.30}$$

$$\tau_d = \frac{2D}{u_d^2} \tag{4.31}$$

The drift velocity for creeping flow over a sphere is determined by a force balance between gravity, buoyancy, and drag given by [102]

$$6\pi\mu_f \frac{d_p}{2} u_d = (\rho_p - \rho_f) V_p g \tag{4.32}$$

$$u_d = \frac{d_p^2 (\rho_p - \rho_f) g}{18\mu} \tag{4.33}$$

where ρ is the density of the particle (p) or fluid (f), V_p is the particle volume, u is the drift velocity, and g is the acceleration of gravity.

The drift velocity for particles to thermally diffuse is estimated as D/l with l taken as 500 μm. The results are plotted in Figure 4.26. Considering slower diffusion, settling and aggregation to be optimal, an optimum particle diameter for our system is determined to be about 130 nm. This is consistent with the simulation results for diffusion and aggregation for the 130 nm particles.

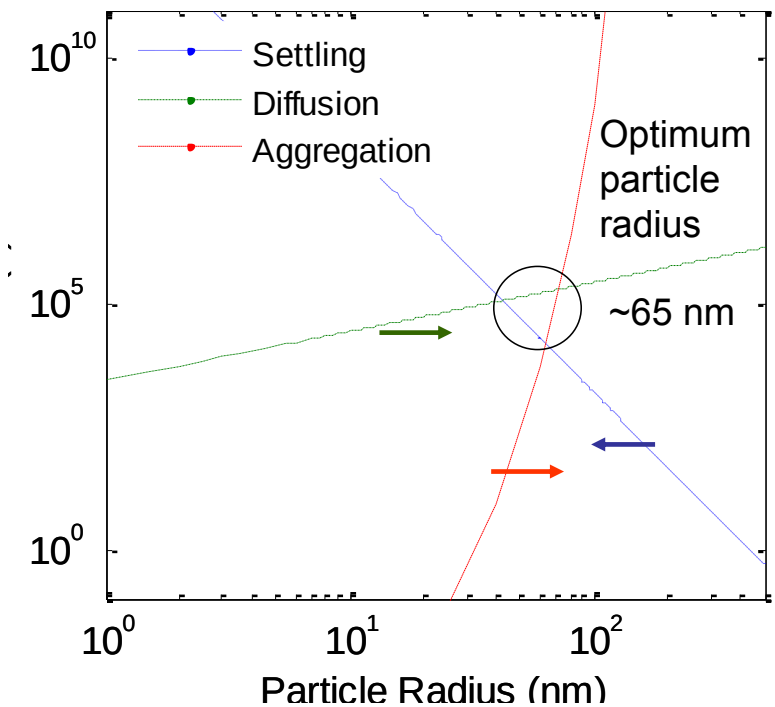

Figure 4.26: Time constant for aggregation (dot), settling (dash), and diffusion (dash-dot) plotted versus particle radius. For each line the arrow points in the direction of increased stability.

4.5 Conclusions

Through experimentation and Monte Carlo simulation of aggregation and thermal diffusion, verified by a numerical model of thermal diffusion, it is shown that the combination of aggregation and thermal diffusion can lead to large variations in thermal conductivity. The aggregation of stabilized nanofluids significantly increases the thermal conductivity of the fluid. Thermodiffusion affects the amount of aggregation across a temperature gradient by creating concentration gradients causing variations in the speed of aggregation and size of aggregates within the nanofluid. The aggregation of the particles increases the concentration gradient due to the larger aggregates forming in the cold region being less mobile. Although the effects of the

stabilizers are not accounted for in the simulation, it predicts the thermal conductivity of the nanofluid well through well known composite theory.

Large viscosity distributions form due to the aggregate size distribution. As aggregation progresses the viscosity increases faster while the thermal conductivity increases slower causing much larger viscosity enhancement factors and unfavorable nanofluids. Increasing the particle size greatly reduces the rate of both the aggregation and thermal diffusion allowing the nanofluid to stay in the favorable regime at the higher concentrations over long periods of time. An optimum particle size can be determined for individual systems and is found to be 130 nm for this system.

PAGE INTENTIONALLY LEFT BLANK

Chapter 5

Conclusions

5.1 Summary

This thesis work focused on understanding the fundamental physics behind the thermal behavior of nanofluids through a study of the aggregation and thermal diffusion of the nanoparticles. The nanofluid temporal behavior is studied experimentally during the progression of aggregation and thermal diffusion. The evolution of the thermal conductivity distribution in a temperature gradient is measured through diffraction limited infrared microscopy. The evolution of the aggregate size and structure at different temperatures is studied with static light scattering. The thermal diffusion and aggregation of the nanofluid are modeled individually and together via a Monte Carlo simulation to study how each one affects the other. The simulation is then used to study the effect of particle size. Finally, an optimization study is completed to determine an optimum particle size for limiting aggregation, diffusion, and settling. The major findings of this thesis work are summarized as follows:

- The thermal conductivity of the nanofluids are found to increase over time, which can be explained by the aggregation of the nanoparticles (Chapter 2)

- Thermal conductivity distributions are found to develop over time in a temperature gradient, which can be attributed to the combination of thermal diffusion and aggregation. (Chapter 2)
- Aggregation in nanofluids is found to be diffusion limited with a fractal dimension of 1.8. (Chapter 3)
- A Monte Carlo simulation of Brownian based aggregation and thermal diffusion are found to model the thermal conductivity measurements well. (Chapter 4)
- Variation in aggregate size across temperature gradient causes large variations in viscosity. (Chapter 4)
- Aggregation in nanofluids leads to unfavorability due to the increased viscosity. (Chapter 4)
- An optimum particle diameter reducing aggregation, diffusion, and settling rates for the system modeled is estimated to be 130 nm. (Chapter 4)

5.2 Discussion

Nanofluids for heat transfer will be subject to a temperature distribution, which will result in thermal diffusion. Brownian motion of the particles allows the particles to interact inducing aggregation. To characterize the effects of the combination of thermal diffusion and aggregation the thermal conductivity distribution over time was calculated from high resolution IR microscopy. The full field temperature distribution allowed for the extraction of information not obtainable using other thermal conductivity measurement techniques. The aggregation is measured through static light scattering yielding the aggregate fractal dimension and length scale. The results are modeled using Monte Carlo simulations of Brownian motion. The simulation

models three situations: aggregation in isothermal conditions, diffusion of non-interacting particles, and the combined aggregation and thermal diffusion.

Our results from the thermal conductivity measurement show large increases in thermal conductivity over time. These results are modeled very well by fractal theory for aggregation. The measurement and simulation of the thermal conductivity distribution over time both show larger increases in thermal conductivity in the cold region of the fluid due to the diffusion of particles towards the cold region causing greater aggregation. Although the increase in thermal conductivity appears favorable for the heat transfer, two other aspects work against the favorability. First, the larger enhancements are occurring in the cold region of the fluid away from the heat source where higher thermal conductivities are needed. Second, the aggregation also increases the viscosity. Given the variations in thermal conductivity across the temperature gradient, the viscosity distribution that already exists due to the temperature gradient will be intensified from aggregation variations. The nanofluid will only be favorable over the base fluid if the increased thermal power removed is greater than the increased pumping power required to drive the fluid. These must always be taken into account when considering the effectiveness of a nanofluid.

Both the aggregation measurement and simulation of isothermal aggregation show faster aggregation for higher temperatures and concentrations. This effect could easily produce an apparent increase in thermal conductivity with temperature after only 15 minutes like those measured by previous researchers. Given the agreement between the thermal conductivity measurement and the simulation taking into account only well know Brownian motion based diffusion and aggregation, it is unlikely another effect could have caused the variations with temperature. This would appear to produce greater aggregation in the hot region of the nanofluid subjected to a temperature gradient. However, the effect of the concentration gradient due to the thermal diffusion overwhelms the temperature effects.

Calculations of the viscosity and thermal conductivity from the fractal theory show that the rate of increase in viscosity increasing with aggregation while the rate of

the increase in thermal conductivity decreases with further aggregation. These trends lead to unfavorable nanofluids. Given the dependence of rate of aggregation, diffusion, and settling on the particle size and apparent lack of dependence of the thermal conductivity and viscosity on particle size as long as the particles remain small, it is interesting to study the effects of particle size. We showed with the simulation the expected decrease in rate of aggregation and diffusion as the particle size is increased at a constant volume fraction due to the reduction in the number of particles and diameter dependence of Stoke's drag. With an increase in particle diameter from 40 nm to 130 nm, the aggregation and diffusion goes from strong to nonexistent. At the larger particle sizes, the effective medium theories for thermal conductivity and viscosity could be applied allowing for greater enhancements in thermal conductivity than viscosity allowing for a favorable nanofluid. However, it is important not to increase the particle size so much that settling becomes important.

This leads to the idea of an optimum particle size for nanofluids. By comparing the time constants for aggregation, diffusion, and settling, for our system an optimum particle size is found to be 130 nm. Although the larger particle size removes the effects that made nanofluids so exciting and well funded, these effects also produced unfavorable consequences, reducing the overall favorability of the nanofluid.

5.3 Recommendations for Future Work

This work focused on understanding the effects of aggregation and thermal diffusion on the thermal conductivity of nanofluids for heat transfer. It is determined that aggregation is the cause of the enhanced thermal conductivity reported by many research groups. Further studies of the thermal conductivity over time in effectively isothermal conditions would increase the certainty of this statement. It is expected that the aggregation will increase the viscosity of the nanofluids greatly creating an unfavorable nanofluid. Viscosity measurements to date have been done over short

periods of time not allowing for aggregation to progress or in a single pass system where the nanofluid is not looped to allow for aggregation effects to be measured. Further studies on the viscosity with aggregation should be done to study this effect. A study should also be done to determine whether the aggregates change their size or structure with flow conditions at the temperatures typical of cooling applications.

It is determined that an optimal particle size for this system is 130 nm to create a more stable fluid reducing aggregation, diffusion and settling. A full study of more stable nanofluids and their effectiveness as actual heat transfer fluids would finally determine the actual applicability of nanofluids in cooling solutions.

LIST OF REFERENCES

[1] A. Krum, "Thermal Management," *Electronics Packaging and Interconnection Handbook*, Ed. By C. A. Harper, 3rd Edition, McGraw-Hill, 2000

[2] *International Technology Roadmap for Semiconductors: Assembly and Packaging*, http://www.itrs.net

[3] R. Prasher, "Thermal Interface Materials: Historical Perspective, Status and Future Directions," *Proceedings of the IEEE* **94**, 1571 (2006)

[4] L. W. da Silva and M. Kaviany, " Micro-thermoelectric Cooler: Interfacial Effects on Thermal and Electrical Transport," *Int. J. Heat Mass Transfer* **47**, 2417 (2004)

[5] L. E. Bell, "Cooling, Heating, Generating Power, and Recovering Waste Heat with Thermoelectric Systems," *Science* **321**, 1457 (2008)

[6] S. B. Riffat and X. Ma, "Improving the Coefficient of Performance of Thermoelectric Cooling Systems: A Review," *Int. J. Energy Research* **28**, 753 (2004)

[7] M. Lee, M. Wong, and Y. Zohar, "Characterization of an Integrated Micro Heat Pipe," *J. Micromechanics and Microengineering* **13**, 58 (2003)

[8] L. Lin, R. Ponnappan, and J. Leland, "High Performance Miniature Heat Pipe," *Int. J. Heat Mass Transfer* **45**, 3131 (2002)

[9] L. Jiang, J. Mikkelsen, J-M. Koo, D. Huber, S. Yao, L. Zhang, P. Zhou, J. G. Maveety, R. Prasher, J. G. Santiago, T. W. Kenny, and K. E. Goodson, "Closed-Loop Electroosmotic Microchannel Cooling System for VLSI Circuits," *IEEE Transactions on Components and Packaging Technologies* **25**, 347 (2002)

[10] S. G. Kandlikar, "High Flux Heat Removal with Microchannels – A Roadmap of Challenges and Opportunities," *Heat Transfer Engineering* **26**, 5 (2005)

[11] D. B. Tuckerman and R. F. W. Pease, "High-Performance Heat Sink for VLSI," *IEEE Electron Device Letters* **2**, 126 (1981)

[12] L. Zhang, J-M. Koo, L. Jiang, M. Asheghi, K. E. Goodson, J. G. Santiago, T. W. Kenny, "Measurements and Modeling of Two-Phase Flow in Microchannels with Nearly Constant Heat Flux Boundary Conditions," *J. Microelectromechanical Sys.* **11**, 12 (2002)

[13] C. H. Hidrovo, T. A. Kramer, E. N. Wang, S. Vigneron, J. E. Steinbrenner, J-M. Koo, F-M Wang, D. W. Fogg, R. D. Flynn, E. S. Lee, C-H. Cheng, T. W. Kenny, J. K. Eaton, and K. E. Goodson, "Two-phase Microfluidics for Semiconductor Cicuits and Fuel Cells," *Heat Transfer Engineering* **27**, 53 (2006)

[14] T. W. Kenny, K. E. Goodson, J. G. Santiago, E. Wang, J-M. Koo, L. Jiang, E. Pop, S. Sinha, L. Zhang, D. Fogg, S. Yao, R. Flynn, C-H. Chang, and C. H. Hidrovo, "Advancec Cooling Technologies for Microprocessors," *Int. J. High Speed Electronics and Systems* **16**, 301 (2006)

[15] T. Cosgrove and B. Vincent, *Colloid Science – Principles, Methods and Applications*, Blackwell Publishing, UK, 2005

[16] M-C. Daniel and D. Astruc, "Gold Nanoparticles: Assembly, Supramolecular Chemistry, Quantum-Size-Related Properties, and Applications toward Biology, Catalysis, and Nanotechnology," *Chem. Rev.* **104**, 293 (2004)

[17] R. Stanway, "Smart fluids: current and future developments," *Mater. Sci. Tech.* **20**, 931 (2004)

[18] D. J. Klingenberg, "Magnetorheology: Applications and Challenges," *AIChE J.* **47**, 246 (2001)

[19] C. Scherer and A. M. Figueiredo Neto, "Ferrofluids: Properties and Applications," *Brazilian J. Phys.* **35**, 718 (2005)

[20] L. Trahms, "Biomedical Applications of Magnetic Nanoparticles," *Lect. Notes Phys.* **763**, 327 (2009)

[21] P. K. Jain, K. S. Lee, I. H. El-Sayed, and M. A. El-Sayed, "Calculated Absorption an Scattering Properties of Gold Nanoparticles of Different Size, Shape, and Composition: Applicaton in Biological Imaging and Biomedicine," *J. Phys. Chem. B* **110**, 7238 (2006)

[22] C. J. Gannon, C. R. Patra, R. Bhattacharya, P. Mukherjee, and S. A. Curley, "Intracellular gold nanoparticles enhance non-invasive radiofrequency thermal destruction of human gastrointestinal cancer cells," *J. Nanobiotech.* **6**, 2 (2008)

[23] D. Pissuwan, S. M. Valenzuela, and M. B. Cortie, "Therapeutic possibilities of plasmonically heated gold nanoparticles," *TRENDS in Biotech.* **24**, 62 (2006)

[24] V. P. Zharov, E. N. Galitovskaya, C. Johnson and T. Kelly, "Synergistic Enhancement of Selective Nanophotothermolysis with Gold Nanoclusters: Potential for Cancer Treatment," *Lasers in Surgery and Medicine* **37**, 219 (2005)

[25] J. M. Martin and N. Ohmae, *Nanolubricants*, John Wiley & Sons, Ltd, England, 2008.

[26] B. Li, X. Wang, W. Liu, and Q. Xue, "Tribochemistry and aniwear mechanism of organic-inorganic nanoparticles as lubricant additives," *Tribol. Lett.* **22**, 79 (2006)

[27] H-L. Yu, Y. Xu, P-J. Shi, B-S. Xu, X-L. Wang, and Q. Liu, "Tribological properties and lubricating mechanisms of Cu nanoparticles in lubricant," *Trans. Nonferrous Metals Soc. China* **18**, 636 (2008)

[28] B. Shen, A. J. Shih, and S. C. Tung, "Application of Nanofluids in Minimum Quantity Lubrication Grinding," *Tribol. Trans.* **51**, 730 (2008)

[29] J. Ma and M. Bai, "Effect of ZrO_2 Nanoparticles Additive on the Tribological Behavior of Multialkylated Cyclopentanes," *Tribol. Lett.* **36**, 191 (2009)

[30] R. Landauer, "Electrical Conductivity in Inhomogeneous Media," *AIP Conf. Proc.* **40,** 1, (1978)

[31] J. C. Maxwell, *A Treatise on Electricity and Magnetism*, II Edition (Clarendon, Oxford, 1881), p. 365.

[32] R. C. Progelhof, J. L. Throne, and R. R. Ruetsch, "Methods for Predicting the Thermal Conductivity of Composite Systems: A Review," *Polymer Engr. Sci.* **16**, 615 (1976)

[33] C-W. Nan, R. Birringer, D. R. Clarke, and H. Gleiter, "Effective Thermal Conductivity of Particulate Composites with Interfacial Thermal Resistance," *J. Appl. Phys.* **81**, 10 (1997)

[34] D. R. Oliver and S. G. Ward, "The Einstein Relation between Relative Viscosity and Volume Concentration of Suspensions of Spheres," *Nature* **173**, 1089 (1954)

[35] A. Einstein, "Berichtigung zu meiner Arbeit: „Eine neue Bestimmung der Moleküldimensionen'," *Ann. Physik* **339**, 591 (1911)

[36] H. Masuda, A. Ebata, K. Teramae and N. Hishinuma, "Alteration of Thermal Conductivity and Viscosity of Liquid by Dispersing Ultra-fine Particles," *Netsu Bussei (Japan)* **7**, 227 (1993)

[37] S. U. S. Choi and J. A. Eastman, "Enhancing Thermal Conductivity of Fluids with Nanoparticles," ASME International Mechanical Engineering Congress & Expo Proceedings (American Society of Mechanical Engineering, San Francisco, 1995)

[38] J. A. Eastman, S. U. S. Choi, S. Li, L. J. Thompson, and S. Lee, "Enhanced Thermal Conductivity Through the Development of Nanofluids," MRS Symposia Proceedings (Materials Research Society, Pittsburgh, 1997), **457**, 3.

[39] S. Lee, S. U. S. Choi, S. Li, and J. A. Eastman, "Measuring Thermal Conductivity of Fluids Containing Oxide Nanoparticles," *J. Heat Transfer* **121**, 280 (1999)

[40] X. Wang, X. Xu, and S. U. S. Choi, "Thermal Conductivity of Nanoparticle – Fluid Mixture," *J. Thermophysics Heat Transfer* **13**, 474 (1999)

[41] S. K. Das, N. Putra, P. Thiesen, and W. Roetzel, "Temperature Dependence of Thermal Conductivity Enhancement for Nanofluids," *J. Heat Transfer* **125,** 567 (2003)

[42] H. E. Patel, S. K. Das, T. Sundararajan, A. S. Nair, B. George, and T. Pradeep, "Thermal Conductivities of Naked and Monolayer Protected Metal Nanoparticle Based Nanofluids: Manifestation of Anomalous Enhancement and Chemical Effects," *Appl. Phys. Lett.* **83**, 2931, 2003

[43] M. L. V. Ramires, J. M. N. A Fareleira, C. A. Nieto de Castro, M. Dix, and W. A. Wakeham, "The Thermal Conductivity of Toluene and Water," *Int. J. Thermophysics* **14**, 1119 (1993)

[44] C. H. Li and G. P. Peterson, "Experimental Investigation of Temperature and Volume Fraction Variations on the Effective Thermal Conductivity of Nanoparticle Suspensions (nanofluids)," *J. Appl. Phys.* **99**, 084314 (2006)

[45] X. Zhang, H. Gu, and M. Fujii, "Experimental Study of the Effective Thermal Conductivity and Thermal Diffusivity of Nanofluids," *Int. J. Thermophysics* **27**, 569 (2006)

[46] B. Yang and Z. H. Han, "Temperature-dependent Thermal Conductivity of Nanorod-based Nanofluids," *Appl. Phys. Lett.* **89**, 083111 (2006)

[47] D. C. Venerus, M. S. Kabadi, S. Lee, and V. Perez-Luna, "Study of Thermal Transport in Nanoparticle Suspensions Using Forced Rayleigh Scattering," *J. Appl. Phys.* **100**, 094310 (2006)

[48] K. Hong, T. Hong, and H. Yang, "Thermal Conductivity of Fe Nanofluids Depending on the Cluster Size of Nanoparticles," *Appl. Phys. Lett.* **88**, 031901 (2006).

[49] N. R. Karthikeyan, J. Philip, and B. Raj, "Effect of Clustering on the Thermal Conductivity of Nanofluids," *Mater. Chem. Phys.* **109**, 50 (2008).

[50] S. D. Fortenberry, E. E. Dominguez-Ontiveros, D. R. Huitink and Y. A. Hassan, "The Temporal Evolution of Nanoparticle Suspensions," *Transactions of the American Nuclear Society* **99**, 785 (2008).

[51] J. Philip, P. D. Shima and R. Baldev, "Evidence for Enhanced Thermal Conduction Through Percolating Structures in Nanofluids," *Nanotechnology* **19**, 305706 (2008).

[52] R. Prasher, P. Phelan, and P. Bhattacharya, "Effect of Aggregation Kinetics on the Thermal Conductivity of Nanoscale Colloidal Solutions (Nanofluid)," *Nano Letters* **6**, 1529 (2006)

[53] A. Putnam, D. G. Cahill, P. V. Braun, Z. Ge, and R. G. Shimmin, "Thermal Conductivity of Nanoparticle Suspensions," *J. Appl. Phys.* **99**, 084308 (2006)

[54] J. Buongiorno et al. "A Benchmark Study on the Thermal Conductivity of Nanofluids," *J. Appl. Phys.* **106**, 094312 (2009)

[55] R. Prasher, D. Song, J. Wang, and P. Phelan, "Measurements of Nanofluid Viscosity and its Implications for Thermal Applications," *Appl. Phys. Lett.* **89**, 133108 (2006)

[56] J-H. Lee, K. S. Hwang, S. P. Jang, B. H. Lee, J. H. Kim, S. U. S. Choi, and C. J. Choi, "Effective Viscosities and Thermal Conductivities of Aqueous Nanofluids Containing Low Volume Concentrations of Al_2O_3 Nanoparticles," *Int. J. Heat Mass Transfer* **51**, 2651-2656 (2008).

[57] J. Garg, B. Poudel, M. Chiesa, J. B. Gordon, J. J. Ma, J. B. Wang, Z. F. Ren, Y. T. Kang, H. Ohtani, J. Nanda, G. H. McKinley, and G. Chen, "Enhanced Thermal Conductivity and Viscosity of Copper Nanoparticles in Ethylene Glycol Nanofluid," *J. Appl. Phys.* **103**, 074301 (2008).

[58] P. Keblinski, S. R. Phillpot, S. U. S Choi, and J. A. Eastman, "Mechanisms of Heat Flow in Suspensions of Nano-sized Particlces (nanofluids)," *Int. J. Heat Mass Transfer* **45**, 855-863 (2002)

[59] Y. Xuan, Q. Li and W. Hu, "Aggregation Structure and Thermal Conductivity of Nanofluids," *Thermodynamics* **49**, 4 (2003)

[60] R. Prasher, P. Bhattacharya and P. E. Phelan, "Thermal Conductivity of Nanoscale Colloidal Solutions (Nanofluids)," *Phys. Rev. Lett.* **94**, 025901 (2005)

[61] W. Evans, J. Fish and P. Keblinski, "Role of Brownian Motion Hydrodynamics on Nanofluid Thermal Conductivity," *Appl. Phys. Lett.* **88**, 093116 (2006)

[62] C-J. Yu, A. G. Richter, J. Kmetko, S. W. Dugan, A. Datta, and P. Dutta, "Structure of Interfacial Liquids: X-ray Scattering Studies," *Phys. Rev. E* **63**, 021205 (2001)

[63] W. Yu and S. U. S. Choi, "The Role of Interfacial Layers in the Enhanced Thermal Conductivity of Nanofluids: A renovated Maxwell Model," *J. Nanoparticle Res.* **5**, 167-171 (2003)

[64] L. Xue, P. Keblinski, S. R. Phillpot, S. U. S. Choi and J. A. Eastman, "Effect of Liquid Layering at the Liquid-Solid Interface on Thermal Transport," *Int. J. Heat Mass Transfer* **47**, 4277-4284 (2004)

[65] P. Ben-Abdallah, "Heat Transfer Through Near-field Interactions in Nanofluids," *App. Phys. Lett.* **89**, 113117 (2006)

[66] R. Jullien and R. Botet, *Aggregation and Fractal Aggregates*, World Scientific, 1987

[67] J. Y. H. Liao, C. Selomulya, G. Bushell, G. Bickert and R. Amal, "On Different Approaches to Estimate the Mass Fractal Dimension of Coal Aggregates," *Part. Part. Syst. Charact.* **22**, 299-309 (2005)

[68] B-X. Wang, L-P. Zhou, and X-F. Peng, "A Fractal Model for Predicting the Effective Thermal Conductivity of Liquid with Suspension of Nanoparticles," *Int. J. Heat Mass Transfer* **46**, 2665-2672 (2003)

[69] R. Prasher, W. Evans, P. Meakin, J. Fish, P. Phelan, and P. Keblinski, "Effect of Aggregation on Thermal Conduction in Colloidal Nanofluids," *App. Phys. Lett.* **89**, 143119 (2006)

[70] W. Evans, R. Prasher, J. Fish, P. Meakin, P. Phelan, and P. Keblinski, "Effect of Aggregation and Interfacial thermal Resistance on Thermal Conductivity of Nanocomposites and Colloidal Nanofluids," *Int. J. Heat Mass Transfer* **51**, 1431 (2008)

[71] R. de Rooij, D. van den Ende, M. H. G. Duits, and J. Mellema, "Elasticity of Weakly Aggregating Polystyrene Latex Dispersions," *Phys. Rev. E* **49**, 3038 (1994)

[72] L. L. Hoekstra, R. Vreeker, and W. G. M. Agterof, "Aggregation of Colloidal Nickel Hydroxycarbonate Studied by Light Scattering," *J. Colloid Interface Sci.* **151**, 17 (1992) ""

[73] A. A. Potanin, "On the Computer Simulation of the Deformation and Breakup of Colloidal Aggregates in Shear Flow," *J. Colloid Interface Sci.* **157**, 399 (1993)

[74] J. Buongiorno, "Convective Transport in Nanofluids," *J. Heat Transfer* **128**, 240 (2006).

[75] D. Wen and Y. Ding, "Effect of Particle Migration on Heat Transfer in Suspensions of Nanoparticles Flowing Through Minichannels," *Microfluid. Nanofluid.* **1,** 183 (2005).

[76] R. Savino and D. Paterna, "Thermodiffusion in Nanofluids Under Different Gravity Conditions," *Phys. Fluids* **20**, 017101 (2008).

[77] B. V. Enüstün and J. Turkevich, "Coagulation of Colloidal Gold," *J. American Chem. Soc.* **85**, 3313 (1963).

[78] H. Fernández-Morán and J. B. Finean, "Electron Microscope and Low-angle X-ray Diffraction Studies of the Nerve Myelin Sheath," *J. Biophys. and Biochem. Cytology* **3**, 725 (1957)

[79] G. Bushell and R. Amal, "Measurement of Fractal Aggregates of Polydisperse Particles Using Small Angle Light Scattering," *J. Colloid Interface Sci.* **221**, 186-194 (2000)

[80] D. W. Schaefer, J. E. Martin, P. Wiltzius, D. S. Cannell, "Fractal Geometry of Colloidal Aggregates," *Phys. Rev. Lett.* **52**, 26 (1984)

[81] A. J. Salem and G. G. Fuller, "Small Angle Light Scattering as a Probe of Flos-induced Particle Orientation," *J. Colloid Interface Sci.* **108**, 1 (1985)

[82] D. A. Weitz, J. S. Huang, M. Y. Lin and J. Sung, "Limits of the Fractal Dimension for Irreversible Kinetic Aggregation of Gold Colloids," *Phys. Rev. Lett.* **54**, 13 (1985)

[83] C. M. Sorensen, "Light Scattering by Fractal Aggregates: A Review," *Aerosol Science and Technology* **35**, 648-687 (2001)

[84] G. C. Bushell, Y. D. Yan, D. Woodfield, J. Raper, and R. Amal, "On Techniques for the Measurement of the Mass Fractal Dimension of Aggregates," *Advances in Colloid and Interface Science* **95**, 1-50 (2002)

[85] L. Onsager, "Reciprocal Relations in Irreversible Processes. I." *Phys. Rev.* **37**, 405, (1931)

[86] S. R. de Groot and P. Mazur, *Non-Equilibrium Thermodynamics*, (New York, Interscience Pub., 1962), p. 273-284.

[87] J. L. Anderson, "Colloid Transport by Interfacial Forces," *Ann. Rev. Fluid Mech.* **21**, 61, (1989)

[88] D. J. Kim, H. Kim, and J. K. Lee, "Dependence of the rheological behavior of electrostatically stabilized alumina slurries on pH and solid loading," *J. Mat. Sci.* **33**, 2931, (1998)

[89] T. A. Witten and L. M. Sander, "Diffusion-Limited Aggregation, a Kinetic Critical Phenomenon," *Phys. Rev. Lett.* **47**, 19, (1981)

[90] P. Meakin and J. M. Deutch, "Spectral Dimension for the Diffusion-Limited Aggregation Model of Colloid Growth," *J. Chem. Phys.* **80**, 5 (1984)

[91] L. A. Spielman and O. Levenspiel, "A Monte Carlo Treatment for Reacting and Coalescing Dispersed Phase Systems," *Chem. Eng. Sci.* **20**, 247-254 (1965)

[92] B. H. Shah, D. Ramkrishna, and J. D. Borwanker, "Simulation of Particulate Systems Using the Concept of the Interval of Quiescence," *AIChE Journal*, **23**, 6 (1977)

[93] K. Liffman, "A Direct Simulation Monte-Carlo Method for Cluster Coagulation," *J. Comp. Phys.* **100**, 116-127 (1992)

[94] F. E. Kruis, A. Maisels and H. Fissan, "Direct Simulation Monte Carlo Method for Particle Coagulation and Aggregation", *AIChE Journal* **46**, 9 (2000)

[95] N. Metropolis and S. Ulam, "The Monte Carlo Method", *J. Amer. Stat. Assoc.* **44**, 247 (1949).

[96] M. Smoluchowski, "Drei Vorträge über Diffusion brownsche Bewegung und Koagulation von Kolloidteilchen," *Physik Z.* **17**, 557-585 (1916)

[97] H. J. Pearson, I. A. Valioulis and E. J. List, "Monte Carlo Simulation of Coagulation in Discrete Particle-size Distributions, Part 1. Brownian motion and fluid shearing," *J. Fluid Mech.* **143**, 367 (1984)

[98] J. C. Maxwell, *A Treatise on Electricity and Magnetism*, II Edition (Clarendon, Oxford, 1881), p. 365.

[99] A. A. Potanin, R. De Rooij, D. Van den Ende, and J. Mellema, "Microrheological Modeling of Weakly Aggregated Dispersions," *J. Chem. Phys.* **102**, 14 (1995).

[100] W. J. Tseng and C. H. Wu, "Aggregation, Rheology and Electrophoretic Packing Structure of Aqueous Al_2O_3 Nanoparticle Suspensions," *Acta Materialia* **50**, 3757 (2002)

[101] S. A. Putnam, D. G. Cahill, and G. C. L. Wong, "Temperature Dependence of Thermodiffusion in Aqueous Suspensions of Charged Nanoparticles," *Langmuir* **23,** 9221-9228 (2007).

[102] R. J. Hunter, *Foundations of Colloid Science*, Oxford University Press: New York, 2001

[103] L. H. Hanus, R. U. Hartzler, and N. J. Wagner, "Electrolyte-Induced Aggregation of Acrylic Latex. 1. Dilute Particle Concentrations," *Langmuir* **17**, 3136-3147 (2001).

[104] W. N. Russel, D. A. Saville, and W. R. Schowalter, *Colloidal Dispersions*, Cambridge University Press: Cambridge, UK, 1989

[105] E. P. Honig, G. J. Roebersen, and P. H. Wiersema, "Effect of Hydrodynamic Interaction on the Coagulation Rate of Hydrophobic Colloids," *J. Colloid Interface Sci.* **36**, 1 (1971)

[106] E. J. W. Verwey and J. Th. G. Overbeek, *Theory of the Stability of Lyophobic Colloids*, Elsevier, Amsterdam, 1948

[107] M. Schudel, S. H. Behrens, H. Holthoff, R. Kretzschmar, and M. Borkovec, "Absolute Aggregation Rate Constants of Hematite Particles in Aqueous Suspensions: A Comparison of Two Different Surface Morphologies," *J. Colloid Interface Sci.* **196**, 241-253 (1997)

DISTRIBUTION

Electronic Distribution

1 Prof. K. E. Goodson
goodson@stanford.edu
Department of Mechanical Engineering
440 Escondido Way, Bldg 530
Stanford University
Stanford, CA 94305-3032

1	MS0116	J. B. Woodard	2134
1	MS0340	M. E. Gonzales	8240
1	MS0359	Y. V. Moreno	1912
1	MS0621	N. S. Rattan	5636
1	MS1078	W. L. Hermina	1710
1	MS9001	C. D. Moen	8005
1	MS9042	E-P. Chen	8246
1	MS9054	R. W. Carling	8300
1	MS9054	A. E. Pontau	8360
1	MS9161	S. K. Griffiths	8300
1	MS9161	R. H. Nilson	8365
1	MS9291	B. C-P. Wu	8125
1	MS9292	M. P. Kanouff	8365
1	MS9403	A. M. Morales	8223
1	MS9403	B. E. Mills	8223
1	MS9404	J. A. Zimmerman	8246
1	MS9404	R. E. Jones	8246
1	MS9404	T. Westover	8246
1	MS9404	X. Zhou	8246
1	MS9405	G. D. Kubiak	8600
1	MS9409	N. R. Fornaciari	8365
1	MS9409	D. E. Dedrick	8365
1	MS9409	W. G. Houf	8365
1	MS9409	S. C. James	8365
1	MS9409	T. A. Johnson	8365
1	MS9409	J. A. Templeton	8365
1	MS9409	G. J. Wagner	8365
1	MS9409	W. S. Winters	8365
1	MS9661	A. D. Shugard	8224
1	MS0899	Technical Library	9536
1	MS0123	D. Chavez, LDRD Office	1011

Sandia National Laboratories